SYNTHESIS OF ZINC OXIDE-BASED NANOMATERIALS FOR CATALYTIC AND ANTIBACTERIAL APPLICATIONS

Aklilu Guale

A Dissertation Submitted to the Department of Applied Chemistry,

School of Applied Natural Science

Presented in Partial Fulfillment of the Requirement for the Degree of Doctor of Philosophy in Applied Chemistry (Materials Chemistry)

Office of Graduate Studies

Adama Science and Technology University

February, 2023

Adama, Ethiopia

SYNTHESIS OF ZINC OXIDE-BASED NANOMATERIALS FOR CATALYTIC AND ANTIBACTERIAL APPLICATIONS

Aklilu Guale

Supervisors

Dr. Fedlu Kedir (Associate Professor)

Dr. Osman Ahmed (Associate Professor)

A Dissertation Submitted to the Department of Applied Chemistry,

School of Applied Natural Science

Presented in Partial Fulfillment of the Requirement for the Degree of Doctor of Philosophy in Applied Chemistry (Materials Chemistry)

Office of Graduate Studies

Adama Science and Technology University

February, 2023

Adama, Ethiopia

Declaration

I hereby declare that this dissertation entitled "**Synthesis of Zinc Oxide-based Nanomaterials for Catalytic and Antibacterial Applications"** is my original work. That is, it has not been submitted for the award of any academic degree, diploma or certificate in any other university. All sources of materials used for this dissertation have been duly acknowledged through appropriate citations.

Aklilu Guale _____ _____

Name of student Signature Date

Approval Page

I/we hereby certify that the recommendations and suggestions made by the board of examiners are appropriately incorporated into the final version of the dissertation entitled "**Synthesis of Zinc Oxide-based Nanomaterials for Catalytic and Antibacterial Applications**" by **Aklilu Guale**.

Major Supervisor	Signature	Date
Co-supervisor	Signature	Date

We, the undersigned, members of the Board of Examiners of the dissertation open defense by **Aklilu Guale** have read and evaluated the dissertation entitled "**Synthesis of Zinc Oxide-based Nanomaterials for Catalytic and Antibacterial Applications**" and examined the candidate during open defense. This is, therefore, to certify that the dissertation is accepted for partial fulfillment of the requirement of the degree of Doctor of Philosophy in **Applied Chemistry (Materials Chemistry).**

Chairperson	Signature	Date
Internal Examiner	Signature	Date
External Examiner 1	Signature	Date
External Examiner 2	Signature	Date

Finally, approval and acceptance of the dissertation is contingent upon submission of its final copy to the Office of Postgraduate Studies (OPGS) through the candidate's Department Graduate Council (DGC) and School Graduate Committee (SGC).

_____	_____	_____
Department Head	Signature	Date
_____	_____	_____
School Dean	Signature	Date
_____	_____	_____
Office of Postgraduate Studies, Dean	Signature	Date

ACKNOWLEDGEMENTS

All the good things come to an end and, this PhD work is the product of years of support, mentorship, and friendship from so many people. At this point, I would like to thank all the people that contributed to the work presented in this dissertation.

First of all, I would like to express my deepest gratitude to my supervisors Dr. Fedlu Kedir, Dr. Osman Ahmed, and Dr. Rajalakshmanan Eswaramoorthy for introducing the present work topic, their unreserved cooperation, constructive criticism and valuable suggestion, supervision, appreciable encouragement, and consultancy throughout the work.

Special thanks to Dr. Lemma Teshome for his support in different ways to complete this work from sample characterization to the valuable feedback and comments received to publishing parts of this work.

My sincere thanks to Mr. Guta Amanu and Mr. Eticha Abdisa, Mr. Demeke Tesfaye, Mr. Leta, Mr. Lemmi, Ms. Emebet, and Ms. Bontu for their technical support, contributions, and efforts in helping me at the laboratory and sample characterization.

I would also like to thank my dissertation examiners, Dr. Bedasa Abdisa and Dr. Aschalew Tadesse for their constructive comments, thoughts, and the very fruitful experience during my final progress report presentation.

I thank Prof Neeraj Gupta for the valuable comments, suggestions, and advice informally received on my PhD work.

Also, I want to thank Ms. Kidan, Ms. Mekdes, Ms. Mastewal, Ms. Adina for their cooperation to keep the laboratory stay opened during my lab work.

Moreover, I acknowledge Wachemo University for sponsoring my PhD. study, Adama Science and Technology University for my PhD study and financial support; Department of Applied Chemistry, Department of Applied Biology, and Department of Materials Engineering for providing laboratory space and allowing me to use the facilities in the laboratory to accomplish this work. I also acknowledge Prof. Jaebeom Lee's lab (National Research Foundation of Korea, NRF-2021H1D3A2A01099457) for supporting different tests and sample characterizations.

My special thanks to goes to all my friends that I made during my PhD for all they have done for making my life more beautiful, inside and outside the university: invaluable advice, encouragement, generous support, and friendship throughout my study.

Finally, I want to thank my parents for their unconditional love, support and encouragement during my PhD study.

TABLE OF CONTENTS

CONTENTS **PAGE**

LIST OF FIGURES

LIST OF SCHEMES

LIST OF TABLES

LIST OF ABBREVIATIONS AND ACRONYMS

4-NP	4-Nitrophenol
4-AP	4-Aminophenol
BET	Brunauer-Emmett-Teller
BJH	Barrett-Joyner-Halenda
CB	Conduction band
DMSO	Dimethyl sulfoxide
EDS	Energy dispersive spectroscopy
EIS	Electrochemical impedance spectroscopy
Eqn.	Equation
E. coli	*Escherichia coli*
FTIR	Furrier transform infrared
VSB	*Verbascum sinaiticum* Benth.
GO	Graphene oxide
HAADF-STEM	High-angle annular dark-field scanning transmission electron microscopy
HRTEM	High-resolution transmission electron microscope
MB	Methylene blue
MW	Microwave
MS	Mott-Schottky

NCs	Nanocomposites
NMs	Nanomaterials
NPs	Nanoparticles
P. aeruginosa	*Pseudomonas aeruginosa*
PEG	polyethylene glycol
PL	Photoluminescence
rGO	Reduced graphene oxide
RhB	Rhodamine B
RHE	Reversible hydrogen electrode
ROS	Reactive oxygen species
S. aureus	*Staphylococcus aureus*
S. pyogenes	*Streptococcus pyogenes*
SEM	Scanning electron microscope
TEM	Transmission electron microscope
UV-Vis	Ultraviolet -visible
VB	Valance band
CAL	*Cordia africana* Lam.
XPS	X-ray photoelectron spectroscopy
XRD	X-ray diffraction
DNA	Deoxyribonucleic acid

Abstract

Nanomaterial-based catalytic conversion of hazardous organic pollutants into benign substances is an attractive method for wastewater treatment. In this study, metal oxide-based nanomaterials (CuO, ZnO, CuO-ZnO, and rGO-ZnO/CuO) were prepared by a microwave-assisted method using plant extracts and low toxicity level reagent for wastewater remediation and antibacterial activities. In this regard, CuO nanoparticles were synthesized by a microwave-assisted method using Cordia africana Lam. leaf extracts. Also, CuO-ZnO nanocomposites (NCs) were synthesized by using an extract of Verbascum sinaiticum Benth plant. Similarly, rGO-ZnO/CuO nanocomposites (NCs) were synthesized via a simple, microwave (MW)-assisted method. X-ray diffraction analysis (XRD), spectroscopic (UV-visible, Fourier Transform-infrared spectroscopy, and photoluminescence), microscope (scanning electron microscope, transmission electron microscope*), and electrochemical methods were used to explore the crystallinity, optical characteristics, morphology, composition, and electrochemical properties of the synthesized nanomaterials, respectively. The X-ray diffraction analysis and scanning electron microscope/energy dispersive spectroscopy analyses indicated the formation of nanocrystals of monoclinic CuO phase having a cluster of spherical-shaped morphology using Cordia africana Lam. extract, plate-like CuO-ZnO NCs using the extract of Verbascum sinaiticum Benth, rod-shaped rGO-ZnO/CuO and flower-like rGO-ZnO/CuO using PEG-200. Compared to pristine ZnO, all nanocomposites (i.e., plate-like CuO-ZnO, rod-shaped rGO-ZnO/CuO, and flower-like rGO-ZnO/CuO) have showed enhanced visible light harvesting capability and suppressed rate of electron-hole recombination. The performance of the as-synthesized nanomaterials was tested against catalytic reduction of 4-nitrophenol, photocatalytic degradation of methylene blue, and disinfection of E. coli, S. aureus, P. aeruginosa, and S. pyogenes bacterial strains. According to the result, the reduction of 4-nitrophenol to 4-aminophenol was achieved with ratio constants of 75.8 $min^{-1}g^{-1}$ (CuO), 5.9 $min^{-1}g^{-1}$ (plate-like CuO-ZnO), and 11.7 $min^{-1}g^{-1}$ (rod-shaped rGO-ZnO/CuO). Similarly, 82%, 90%, and 86% photocatalytic degradation of methylene blue initial concentration were achieved within 105 min using plate-like CuO-ZnO, rod-shaped rGO-ZnO/CuO, and flower-like rGO-ZnO/CuO nanocomposites, respectively. Among the prepared nanomaterials, CuO (using Cordia africana Lam) and CuO-ZnO (using PEG-200) showed antibacterial activities against all four bacterial strains (E. coli, S. aureus, P. aeruginosa, S. pyogenes) with an approximate inhibition zone (mm) of (20.5, 10.0, 22.0, 24.8, respectively) for CuO and (13.8, 11.0, 18.5, 24.0, respectively) for CuO-ZnO at 37.5 μg/mL concentration. Modification of ZnO with CuO and rGO showed enhanced photocatalytic activities due to the improved visible light absorption and suppressed electron-hole (e^-/h^+) recombination. Therefore, nanomaterials prepared using low toxicity level reagents including CuO nanoparticles (Cordia africana Lam.), CuO-ZnO NCs (Verbascum sinaiticum Benth), and rGO-ZnO/CuO NCs (PEG-200) could be a desirable catalyst for the elimination of organic pollutants for the remediation of wastewater.*

Keywords: *Cordia africana* Lam., *Verbascum sinaiticum* Benth., antibacterial, p-n heterojunctions, photocatalysis, catalytic reduction.

CHAPTER ONE

1. INTRODUCTION

1.1. Background of Study

Environment pollution is an undesirable change in the physical, chemical, or biological characteristics of the environment including air, water, and solids that causes harmful effects on various forms of life and property (Singer, 1970). The rate and quantity of the pollutants discharged into the environment (like industrial effluents, domestic pollutants, etc.) have become beyond the ecosystem's capability to degrade or convert them into nontoxic or environmentally benign substances (Wick & Chatzinotas, 2019). Particularly, surface and ground sources of freshwater are vulnerable to pollution due to the continuous increase in organic, inorganic, and biological pollutants from industrial effluents and domestic sewage discharged into the environment. Pesticides, synthetic organic dyes, and aromatic derivatives like methylene blue, methyl orange, rhodamine B, and toxic heavy metal ions of (Cr, As, Cd, Pb, Hg, etc.) are a few examples of pollutants. They cause health-related problems such as cancer, dermatitis, respiratory diseases, allergic reactions in eye, skin irritation, mucus membrane irritation, blood disorder, liver and kidney damage, poisoning the central nervous system, and others (Boruah et al., 2018; Ramanathan et al., 2019)

Furthermore, the emergence of multidrug-resistant human pathogenic microbes to one or several antibiotics is also a matter of great concern (Rai et al., 2012). Common human pathogens include *Bacillus subtilis (B. subtilis), Bacillus megaterium (B. megaterium), Staphylococcus aureus (S. aureus), Sarcina lutea, Escherichia coli (E. coli), Pseudomonas aeruginosa (P. aeruginosa),* and *Klebsiella pneumonia (K. pneumonia).* In light of this, there is an urgent need to develop or search for new antimicrobial agents by easy, rapid, and eco-friendly route having broad-spectrum antimicrobial activity (Ingle et al., 2014; Rai et al., 2012).

In the context of Ethiopia, rivers and streams are the main sources of water for industries, drinking, and irrigation. Preliminary studies showed that untreated effluents from industries, sewage from domestic households, and different agricultural activities are among the major sources of surface and groundwater contamination (Ademe, 2014; D. Dadi et al., 2017).

Potential pollution sources of water pollutants from different industries in Ethiopia include clay & glass, food, paper & pulp, textile, tannery, and leather industries, etc. (Ademe, 2014; Gebrekidan et al., 2009; Gitet et al., 2013).

Over the years, varieties of conventional techniques have been employed to remove organic pollutants from water (Ajmal et al., 2014; Younas et al., 2021). These include (i) physical: sedimentation, filtration, (ii) chemical: flocculation and coagulation, ozonation, chemical precipitation, adsorption, and (iii) biological: bioremediation, aerobic treatment, and anaerobic treatment methods (A. Saravanan et al., 2021). Most of these techniques are often very costly or involve the accumulation of concentrated sludge and create a disposal problem, or generate toxic products as a byproduct (Y. Huang et al., 2019). Persistent organic pollutants are among the challenging ones to remove using conventional techniques (Ajmal et al., 2014). In line with this, the emergence of multidrug-resistant bacteria has also become a big concern worldwide. Thus, it is important to look for a method that could effectively remediate polluted water following environmentally benign and economical methods. In recent years, researchers are developing nanomaterial-based adsorbents, catalysts, and antibacterial agents to treat the rapidly increasing pollutant loads introduced to water and multidrug-resistant pathogens (Santhosh et al., 2016; Yaqoob, Parveen, et al., 2020).

Nanomaterials are the cornerstones of material science and are the core of the emerging nanotechnology field. Their distinctive and tailorable size-dependent properties (over the scale of 1-100 nm), make them attractive for various emerging applications (Nasrollahzadeh, Sajadi, et al., 2019). The physical (structural, electronic, optical, and magnetic) and chemical (e.g., catalytic) properties of materials improve significantly when their size is reduced to the nanoscale regime (i.e., 1-100 nm). Thus, owing to their distinctive tunable size-dependent properties, nanomaterials have promising potential in the development of sustainable solutions for critical challenges in energy and environmental issues (Deganello, 2017). During the past decade, nanotechnology has made rapid advances in catalytic fuel production, energy conversion, and remediation of polluted waters. Among these, the application of nanomaterials for wastewater treatment is an active area of research.

Compared to bulk materials, nanomaterials display higher rate/efficiency of adsorption, catalytic reduction, photocatalytic degradation, and bacterial disinfection. Nanomaterials-based

catalysts possess numerous advantages in the applications of photocatalysis and catalytic reduction, and bacterial disinfection (Nosaka & Nosaka, 2017; Ong et al., 2018). For this reason, nanomaterials are viable candidates to convert hazardous water pollutants into environmentally benign ones. Particularly, photocatalysis has a promising significance owing to its capacity for solar light utilization, green virtues, and effectiveness in the degradation of organic pollutants in the water (Ajmal et al., 2014; Anwer et al., 2019; Gadipelly & Mannepalli, 2019). Similarly, the catalytic transformation of pollutants into biodegradable or economically valuable low-toxicity level chemicals using nanomaterials is also a highly desirable approach. In such reactions, nanomaterials-based catalysts provide a sustainable way of transforming organic compounds in an environmentally benign manner in aqueous media (Gadipelly & Mannepalli, 2019). Furthermore, there has been a growing interest in the application of nanomaterials as antibacterial agents for the remediation of polluted water against multidrug-resistant human pathogenic microbes (Rai et al., 2012). The application of nanomaterials in wastewater remediation has therefore become increasingly important.

A variety of nanomaterials have been employed as catalysts and antimicrobial agents over the past few decades. These include metals, metal oxides, metal oxide-based nanocomposites (NCs), and others. Metal oxide-based nanomaterials are the potential catalyst due to their remarkable properties and advantages such as high natural abundance, high chemical stability, tunable bandgap/band edge positions, and excellent thermal/electrical conductivity (Bano et al., 2020; M. M. Khan et al., 2015; Ray & Pal, 2017; Sherly et al., 2016). Some of the oxides that have played a key role in enhancing catalytic activities include ZnO, TiO_2, WO_3, CuO, Cu_2O, Fe_2O_3, and others (Danish et al., 2021; Velempini et al., 2021). Among these oxides, ZnO has been extensively studied for catalytic and antibacterial activities. Affordability, high binding energy, abundant availability, non-toxicity, high electron-hole mobility, as well as ease of preparation are some of the features that make ZnO a highly relevant material for photocatalysis (Pirhashemi et al., 2018; Ullah et al., 2021). However, the practical applications of pristine ZnO for photocatalysis were limited due to the high rate of e^-/h^+ recombination, the wide bandgap for visible light activation, and the photocorrosion in aqueous media (Ong et al., 2018; Pirhashemi et al., 2018). Therefore, modifying ZnO to enhance its photocatalytic activities is important.

Reports show that several ZnO performance-enhancing strategies have been developed, such as doping (Kumari et al., 2019), coupling two semiconductors/composite formation (Paydar et al., 2021; Pirhashemi et al., 2018; Taufique et al., 2018), designing new morphology (Thakur & Mandal, 2020), and others (Fei et al., 2019). Studies have shown that coupling two or more semiconductors with appropriate band edges exhibits a synergistic effect that reduces e-/h+ recombination enhancing photocatalysis (Sherly et al., 2016). In this regard, coupling ZnO with narrow bandgap oxides such as CuO, Cu_2O, Fe_2O_3, and others results in ZnO-based nanocomposites. As a p-type semiconductor, CuO is an attractive candidate for producing ZnO-based p-n heterojunctions. CuO is a narrow bandgap (1.2-2.4 eV) p-type semiconductor with good optical, thermal, electrical, and catalytic properties (Oruç & Altındal, 2017; Sagadevan & Murugasen, 2015; Sahooli & Sabbaghi, 2013; Son et al., 2009). It is a relatively low-cost, nontoxic, and environmentally benign oxide. In addition, it has anti-inflammatory and biocide (antifungal, anti-viral, and anti-bacterial) activities (R. Dadi et al., 2019; Varier et al., 2020). The resulting nanocomposites increase the range of solar spectrum absorbed to the visible region and also improve charge separation. In addition, using carbonaceous nanomaterials (graphene, carbon nanotube, g-C_3N_4, etc.) as catalyst support increases the adsorptivity, reduces photocorrosion, and improves the dispersibility of the resulting NCs in aqueous media (Kumaresan et al., 2020; X. Li et al., 2018).

The photocatalytic activity of nanomaterials is highly morphology dependent. Owing to their morphology, 1D nanostructures exhibit attractive features that make them potential candidates for photocatalytic applications (G. Zhang & Sun, 2017). In particular, ZnO nanorods are known for having high surface area and aspect ratio, fast charge transfer, high photosensitivity, better charge separation, and efficient confinements on electrons and photons (Aspoukeh et al., 2022; Ramos et al., 2022; Zhou et al., 2013). Recently, nanostructures comprised of ZnO, rGO, and CuO components with varieties of morphologies were reported for catalytic applications. These include, flower-like for photocatalytic degradation of RhB and 4-chlorophenol (Kumaresan et al., 2020), needle-like for photocatalytic oxidation of flue gas (Man et al., 2020), flower-rod-like heterostructures for 4-nitroaniline catalytic reduction (Tantubay et al., 2020), and others (Firoozi & Hosseini-Sarvari, 2021). Generally, the synthesis methods reported in most cases involve the co-deposition of both ZnO and CuO on rGO or GO sheets. Among the synthesis methods reported are solid-state (Kumaresan et al., 2020), hydrothermal (Firoozi & Hosseini-

Sarvari, 2021; Maity et al., 2018; Man et al., 2020; Tantubay et al., 2020; C. Wang et al., 2014), wet chemical/ refluxing (Jyoti & Varma, 2019), and other methods (Asgar et al., 2020; Jyoti et al., 2018). Inherent to the attractive features of nanorods, reports on the synthesis of rod-shaped rGO-ZnO/CuO for catalytic application are rare. Hence, designing an effective technique to synthesize a rod-like rGO-ZnO/CuO nanostructure is highly desirable to exploit the maximum benefit from its catalytic applications.

To benefit from the full potential of nanomaterials, their fabrication strategies need to be simple, fast, economical, and eco-friendly. However, most of the conventional techniques suffer from at least one of the limitations due to the high energy demand, sophisticated instruments involved, and use of toxic and hazardous chemicals that have adverse effects on the environment, human life, and on biological applications of the materials (Annathurai et al., 2019; M. Khan et al., 2015; Yulizar et al., 2018). Among the various methods of preparing ZnO-based NCs, a microwave-assisted method offers many advantages over conventional heating methods, such as fast reactions, uniform particle size distribution, high yield, and highly pure nanomaterials (Sharifi et al., 2021). Reports have shown that different precursors and other reagents can be utilized for the synthesis of ZnO-based nanostructured materials (NMs). Particularly, the choice of proper reagents determines the morphology and properties of the resulting nanomaterials (Mukherji et al., 2019). A green chemistry approach, however, encourages the use of cheap, eco-friendly reagents, and waste-free methods that reduce or eliminate chemical waste (Paristiowati et al., 2019). In this regard, using low toxicity and cheap chemicals like sucrose, PEG, ascorbic acid, and biomolecules from plant extracts complies with the principles of green chemistry (Erythropel et al., 2018).

These days, the use of phytochemicals found in plant extracts as alternatives to toxic synthetic chemicals for nanomaterials synthesis has received growing interest (Hussain et al., 2016; Nasrollahzadeh, Atarod, et al., 2019; Pal et al., 2019). Plant extracts provide biomolecules that are safe, green, low-cost, and naturally available.(Adil et al., 2015; S. G. Ali et al., 2021).In the synthesis of nanostructured materials, the biomolecules found in the plant extracts play a crucial role as reducing agents, stabilizing agents, or both; which in turn affect the properties and morphologies of the resulting nanomaterials (M. Khan et al., 2018; Marslin et al., 2018). In this regard, plant extract-based nanomaterials preparation is one of the promising green routes to

overcome the limitations of the physicochemical methods. Plant extract contains both primary and secondary metabolites such as polyphenolic compounds contain a large number of hydroxyl groups that help in the reduction of metal ions and stabilization of the NPs as they form (Basnet et al., 2018; Kar et al., 2018) According to the literature data, the aqueous extract of *Cordia africana Lam.* (CAL) and *Verbascum sinaiticum* Benth. (VSB) leaves contain phytochemicals that have significant reducing properties, such as polyphenols, tannins, and saponins making them a promising candidate for nanoparticle synthesis (Geyid et al., 2005; Mergia et al., 2016). The leaves of *Cordia africana* Lam. (local name waddessa/wanza) belongs to the family of *Boraginaceae*, and the leaves of *Verbascum Sinaiticum* Benth. (local name gurra-harree/yahiya joro) belongs to the family of *Scrophulariaceae.* Both CAL and VSB are medicinal plants and are abundantly available for use in nanoparticle synthesis.

Considering all the above-indicated ideas the current work aims to synthesize ZnO-based nanocomposite by a green approach using CuO and rGO as ZnO modifiers, utilizing plant extracts and PEG as low-toxicity level reagents, and with the help of efficient, low-cost, simple, and rapid MW-assisted method. Spectroscopy (UV-Vis, FTIR, PL), XRD, microscopy (SEM, TEM), XPS, electrochemical, and other methods were employed to study the optical, crystallinity, morphological, textural, compositional, and electrochemical properties. Further, the performance of the samples was evaluated by employing photocatalytic degradation of MB, catalytic reduction of 4-NP, and antibacterial activities against *E. coli*, *S. aureus*, *P. aeruginosa*, and *S. pyogenes* bacterial strains. Hence, the finding of this study will add important values to the existing knowledge and literatures. Specifically, on the (i) design of simple and green protocol to synthesis rod-shaped and flower-like NCs composed of rGO, ZnO, and CuO in the presence of PEG; (ii) use of CAL and VSB extracts to synthesis CuO NPs, ZnO NPs, and CuO-ZnO NCs; and (iii) performance evaluations of these materials against 4-NP reduction, MB degradation and antibacterial activities.

.

1.2. Statement of the Problem

Water is one of the most important resources responsible for the survival of life on our planet (Westall & Brack, 2018). Among the available water on earth, only 3 % is freshwater, of which about 68.7 % exist as glaciers and icecaps, 30 % as groundwater, and only about 0.3 % is surface freshwater which includes lakes, swamps, and rivers (Thatai et al., 2018). In recent years, the rapid growth of pollutant loads introduced to water due to human activities has become a global concern. In particular, the continuous increase in pollutants discharged into the environment from industrial effluents and domestic sewages is threatening the quality of freshwater (Boruah et al., 2018; Ramanathan et al., 2019; Younas et al., 2021). Specifically, soluble organic dyes and their breakdown products released from industries like textiles (Carmen & Daniel, 2012; Sivaram et al., 2018), paper and pulp (Ilyas et al., 2019; Mandeep et al., 2019), pharmaceuticals, and tanneries (Kanu, Ijeoma and Achie, 2011) are toxic, carcinogenic, or mutagenic to life forms (Mandeep et al., 2019; Sivaram et al., 2018). Therefore, the removal of these pollutants before discharging the effluents into the environment is highly important. Furthermore, persistent organic pollutants such as dyes are among the challenging ones to remove using conventional techniques (Ajmal et al., 2014).

Some of the existing conventional techniques employed for wastewater remediation include, (i) physical treatment methods such as activated carbon, adsorption, reverse osmosis, ultrafiltration, coagulation and flocculation, and membrane process are used to remove the dyes from water, but they transfer the contaminants from one medium to another, resulting in secondary pollution and also further treatment is required to regenerate the adsorbent and replacement of the membranes, which can be costly (Ajmal et al., 2014; Devendran & Swaminathan, 2019; Verma, 2021); (ii) chemical treatment methods, such as chlorination, ozonation, precipitation, neutralization, ultraviolet (UV) light treatment, and chemical oxidation processes for removing a wide range of contaminants, but they may also generate secondary waste products that need to be disposed of properly and also may form harmful by-products (Devendran & Swaminathan, 2019; Reddy et al., 2003; Verma, 2021); (iii) biological treatment methods, such as microbiological decomposition, enzymatic decomposition, biodegradation, anaerobic digestion, aerobic treatment, and flocculation, but inefficient for synthetic dyes and require a stable source of microorganisms, medium temp and pH, and require further bacterial

disinfection steps (Devendran & Swaminathan, 2019; Verma, 2021). Current wastewater treatment methods make use of the combination of physical, chemical and biological processes, and operations to remove insoluble particles and soluble contaminants from polluted water (Crini & Lichtfouse, 2019). Nevertheless, researchers are still struggling to find methods that are eco-friendly, low-cost, effective, and free of generating secondary contaminants. However, low efficiency, high cost, slow process, disposal problems, or generation of secondary contaminants are among limitations of the existing techniques.

Human pathogenic microorganisms are another main factor posing a severe threat to the well-being of humans. Human pathogenic bacteria like *E. coli*, *S. aureus*, *P. aeruginosa*, and *S. pyogenes* are among the most prevalent causes of water-borne diseases. Recently, the emergence of multidrug-resistant human pathogenic microbes to one or several antibiotics is a matter of great concern (Rai et al., 2012). In light of this, there is an urgent need to develop or search for new antimicrobial agents by easy, rapid, and eco-friendly routes having broad-spectrum antimicrobial activity.

In this regard, the development of nanomaterials-based catalysts and antibacterial agents for complete mineralization or transform into low toxicity level /biodegradable and effective bacterial disinfection is an alternative to conventional methods. Nanocatalysts are particularly useful for treating organic water pollutants via complete degradation, transforming them into ecofriendly or industrially useful chemicals. Similarly, NPs have shown antimicrobial activity against the most frequently encountered clinically important multidrug-resistant human pathogens such as *P. aeruginosa, E.coli, and S.aureus* (S. G. Ali et al., 2021; R. Dadi et al., 2019; Thatikayala & Min, 2021). To this end, ZnO-based NMs constitute a potential candidate for their unique features and versatilities.

So far, several modifications were made to improve the performance of the ZnO. To the best of our knowledge, the synthesis of CuO-ZnO NCs using VSB and CAL extracts and the synthesis of rod-shaped rGO-ZnO/CuO NCs using PEG for catalytic and antibacterial applications were not reported. Therefore, in this study, CuO-ZnO NCs were synthesized using VSB and CAL extracts. Also, rod-shaped rGO-ZnO/CuO NCs were synthesized using PEG. CuO and rGO were used to modify the properties of ZnO, such that CuO was used to modify visible light activation and charge separation for CuO is a p-type and narrow bandgap semiconductor; and

graphene (rGO) was used as catalyst support to modify the adsorption capacity, stability, recoverability, and other properties of the ZnO-based nanocomposites for rGO has high adsorbing capacity, high capacity of avoiding agglomeration, and 2D sheet like morphology. The resulting NMs were used in the photocatalytic degradation of MB, catalytic reduction of 4-NP, and antibacterial agents. MB and 4-NP were used as test pollutants.

1.3. Objectives

1.3.1. General Objective

The general objective of this study was to synthesize and characterize ZnO-based nanomaterials by a green approach for the application of catalytic and antibacterial activities.

1.3.2. Specific Objectives

The specific objectives of this study were:

- To synthesize metal oxide nanomaterials: ZnO, CuO, and CuO-ZnO using *Cordia africana* and *Verbascum sinaiticum* Benth extracts.
- To synthesize rGO-ZnO/CuO NCs using PEG-200.
- To characterize synthesized nanomaterial using XRD, UV-Vis, FTIR, PL, SEM/EDS, TEM, XPS, BET, and electrochemical (EIS and Mott-Schottky) methods.
- To carry out the preliminary performance test for best performing material selection.
- To evaluate the performance of the selected composite nanomaterials against photocatalytic degradation of methylene blue dye.
- To evaluate the performance of the selected nanomaterials against catalytic reduction of 4-nitrophenols.
- To evaluate the antimicrobial activity of the selected nanomaterials against *E. coli*, *S. aureus*, *P. aeruginosa*, and *S. pyogenes* bacterial strains.
- To evaluate the recoverability of the selected nanomaterials for photocatalytic degradation of MB and catalytic reduction of 4-nitrophenols

1.4. Significance of the Study

Among the metal oxide-based nanomaterials, ZnO-based nanomaterials are widely used for catalytic and antibacterial activities. Since synthesis of CuO-ZnO NCs using VSB and CAL extracts as well as synthesis of rod-shaped rGO-ZnO/CuO NCs using PEG for catalytic and antibacterial applications were not reported before, the finding of this study may play a significant role in promoting green methods of nanomaterials synthesis for varieties of application. Particularly, it may provide deeper insight on how ZnO-based nanomaterials could be fabricated employing the green chemistry protocols for catalytic and antibacterial applications. Thus, the finding may benefit researchers in the field, science community, people in the academia, and it may contribute to the research gap in the literature. Since the study employed simple, fast, ecofriendly, low-cost materials and scalable methods for material synthesis, it may provide valuable information for those who work on: (i) green method of materials synthesis, (ii) the catalytic transformation of organic pollutants, and (iii) bacterial disinfections. Also, the finding may serve as an input for organizations/sectors working on infectious disease control and polluted water remediation

CHAPTER TWO

2. LITERATURE REVIEW

2.1. Metal Oxide-Based Nanocomposites

In recent years, metal oxide nanostructures have received increasing importance in the field of materials science due to their unique features such as high natural abundance, high chemical stability, tunable bandgap/band edge positions, and excellent thermal/electrical conductivity (Bano et al., 2020; M. M. Khan et al., 2015; Ray & Pal, 2017; Sherly et al., 2016). Nanostructured metal oxides display superiority to their bulk counterparts in size/shape-dependent physicochemical and functional properties, chemical and thermal stability, and a wide range of practical applications (Das & Srivastava, 2018; Vivekanandhan, 2019). As a result of these remarkable properties and advantages, metal oxide-based nanomaterials have been studied in depth for applications in sensors, catalysis, superconductors, electronics, energy production and storage, medicine, and other medical fields (W. Chen et al., 2018; Kwon et al., 2018; Nunes et al., 2019; Raizada et al., 2021; K. R. Singh et al., 2021). Some of the metal oxides with versatile applications include TiO_2, ZnO, SnO_2, CuO, Cu_2O, NiO, Al_2O_3, WO_3, Nb_2O_5, and so on.

Since the materials used for the practical application in a specific field are required to possess certain qualities such as a high surface area, high stability, good recoverability, and appropriate bandgap/band edge potentials; obtaining a single component metal oxide nanostructured material fulfilling all the requirements is challenging. To meet the requirements of a specific application, varieties of modification strategies have been devised through the modification of characteristics such as composition, morphology, electrical and optical properties, surface properties, and others employing techniques such as doping, defect engineering, morphology optimization, composite formation, or coupling with materials like noble metals, carbon nanostructures, and other semiconductors (Djurišić et al., 2014; Mathalai Sundaram et al., 2019; Paydar et al., 2021; Pirhashemi et al., 2018; Taufique et al., 2018; Thakur & Mandal, 2020).

One of these modifications is nanocomposite materials, which are characterized by remarkable properties. Nanocomposite materials are composed of at least one component or phase of

nanoscale dimensions. They possess properties that are not typically observed in single individual components such as optical, electrical, magnetic, adsorptivity, catalytic, chemical, and so on, which can be tuned by controlling composition, stoichiometry, and experimental conditions during composite synthesis (Camargo et al., 2009). So far, a variety of nanocomposites have been developed utilizing compositing components such as metals, metal oxides, and others. In a given NCs, however, effective coupling requires a compatible energy band configuration, less lattice inconformity, and well-matched conductivity between the components of the NCs (Pirhashemi et al., 2018). In particular, nanocomposites containing two or more metal oxides have drawn significant attention because of their synergistic properties.

ZnO is one of these oxides that has been extensively studied because of its impressive properties. Wide bandgap (3.37 eV), abundant availability, high binding energy, non-toxicity, a wide range of morphologies, good isoelectric point (pH 9–9.5), several facile preparation routes, as well as other desirable electro-optical characteristics are some of the features that make ZnO a highly relevant material for photocatalysis and antibacterial applications (Akir et al., 2016; Ong et al., 2018; Pirhashemi et al., 2018; Tănase et al., 2021; Thakur & Mandal, 2020; Ullah et al., 2021). ZnO nanomaterials have versatile applications in photodiodes (Chávez-Urbiola et al., 2019), solar cells (Rahman et al., 2019), photocatalysis (Pirhashemi et al., 2018), sensors and UV-filtering (Subbiah et al., 2018), biomedical fields (Rajeshkumar et al., 2019), antibacterial (S. G. Ali et al., 2021), and others. However, pristine ZnO nanostructures have limitations for photocatalytic applications due to the high rate of e^-/h^+ recombination, the wide bandgap for the activation by visible light, and the photocorrosion in aqueous media (Ong et al., 2018; Pirhashemi et al., 2018). Therefore, modifying ZnO NPs is important for catalytic applications.

Various types of materials have been coupled with ZnO nanostructures to improve their performance in catalytic, antimicrobial, and other applications. Studies have demonstrated that heterojunctions of ZnO (a wide band gap semiconductor) with narrow band gap semiconductors such as CuO, Cu_2O, Fe_2O_3, Bi_2O_3, BiOI, g-C_3N_4, Ag_2O, and AgI exhibited enhanced photocatalytic activity when compared to pristine ZnO (Pirhashemi et al., 2018). Coupling with suitable materials improves the rate of the electrical charge transfer leading to enhanced photocatalytic performance. According to Romeiro et al., rGO-ZnO NCs films exhibit improved electrocatalytic performance for oxygen evolution than ZnO films in water splitting (Romeiro

et al., 2017). As a result, the electrochemical impedance spectroscopy (EIS) experiment showed a decrease in impedance charge transfer resistances in comparison with ZnO. Furthermore, by adding suitable support materials to ZnO, the adsorption properties can be significantly enhanced. Lei *et al.* synthesized hierarchical porous microspheres of ZnO-Al_2O_3 that removed Congo red dye with an efficiency of about two times higher than that of pristine ZnO due to the improved adsorption capacity of the ZnO-Al_2O_3 (C. Lei, Pi, Xu, et al., 2017). Similarly, other ZnO characteristics such as bandgap, stability, charge separation, and others could be improved by forming nanocomposites (Sherly et al., 2016).

As compared to coupling n-type to n-type semiconductors, coupling n-type with p-type semiconductors leads to p-n heterojunction having better charge separation. In p-n heterojunction, the built-in electric potential in the interface offers the advantages of reduced rate of recombination and fast transfer of photogenerated charge carrier (Pirhashemi et al., 2018; L. Zhu et al., 2018). As a consequence, a wide range of ZnO-based p-n heterojunction photocatalytic materials has shown enhanced performance owing to improved visible light response and minimal recombination rates (Ding et al., 2018; Taufique et al., 2018; M. Zhang et al., 2018; Y. H. Zhang et al., 2018). Some of the p-type semiconductors reported for catalytic applications are NiO, CuO, Cu_2O, MnO, Ag_2O, Co_3O_4, MoS_2, (BiOX, X=Cl, Br, and I), etc. For the attractive features of CuO stated in the introduction section, coupling ZnO with CuO could improve the charge separation, lower the band gap, suppresses recombination rate, and other. Since, both the CB and VB band edge positions of CuO lie above the corresponding CB and VB band edge positions of ZnO, CuO is compatible with ZnO for CuO/ZnO heterojunction formation that allows the transfer of charge carriers (Annathurai et al., 2019; Mageshwari et al., 2015). Studies have shown that coupling ZnO with low bandgap p-type semiconductor CuO greatly improved visible light absorption capacity, suppressed e^-/h^+ recombination rates, and improved the degree of photostability in aqueous media (C. Liu et al., 2019; Sahu, Bisht, et al., 2020; Yendrapati Taraka et al., 2019).

2.2. Photocatalysis

Among the various advanced oxidation processes for treating wastewater, photocatalysis using semiconductor nanoparticles has received considerable attention in recent years. A photocatalyst

is a material that is capable of absorbing light, producing electron–hole pairs that enable chemical transformations of the reaction participants and regenerate its chemical composition after each cycle of such interactions (M. M. Khan et al., 2015). Heterogeneous photocatalysis has applications in various areas like environmental remediation, fuel production, disinfection, and antifogging (Danish et al., 2021; Nakata & Fujishima, 2012; C. Zhang et al., 2019).

The performance of heterogeneous photocatalysts depends on both features of the photocatalyst and operational parameters. Some of the important features of a photocatalyst that determine performance are surface area, morphology, exposed facet, crystal defects, stability, and appropriate bandgap/band-edge positions (Asadzadeh-Khaneghah & Habibi-Yangjeh, 2020; Galani & Panda, 2019). Particularly, materials with a high specific surface area like microporous (pore<2 nm) and mesoporous (pore 2-50 nm) structures or sieves and honeycomb-like structures are promising candidates in the field of catalysis.

Furthermore, the main operational parameters that govern the reaction kinetics are the mass of the catalyst, the light wavelength, the radiant flux, the initial concentration of reactants (pollutants), the pH of the medium, and temperature as shown in Figure 1 (Akpan & Hameed, 2009; Herrmann, 2010; A. Kumar, 2017; Lin et al., 2014). As can be seen from the Figure, increasing the light intensity, temperature, mass of catalyst, and initial dye concentration increase the rate of photocatalytic reaction until the optimum is reached (Herrmann, 2010; Lin et al., 2014). The photon energy also affects photocatalysis, i.e., only light with photon energy greater than the bandgap of the catalyst can generate charge carriers. The influence of pH on photodegradation depends on the nature of the surface of the catalyst affecting the adsorption of dye molecules onto the catalyst (Akpan & Hameed, 2009). Holes are considered as the major oxidation species at low pH, while hydroxide radicals are the predominant oxidation species at neutral and high pH levels. Hence, optimization of both affecting features and operational parameters with the appropriate choice of material is needed to achieve enhanced photocatalytic performance.

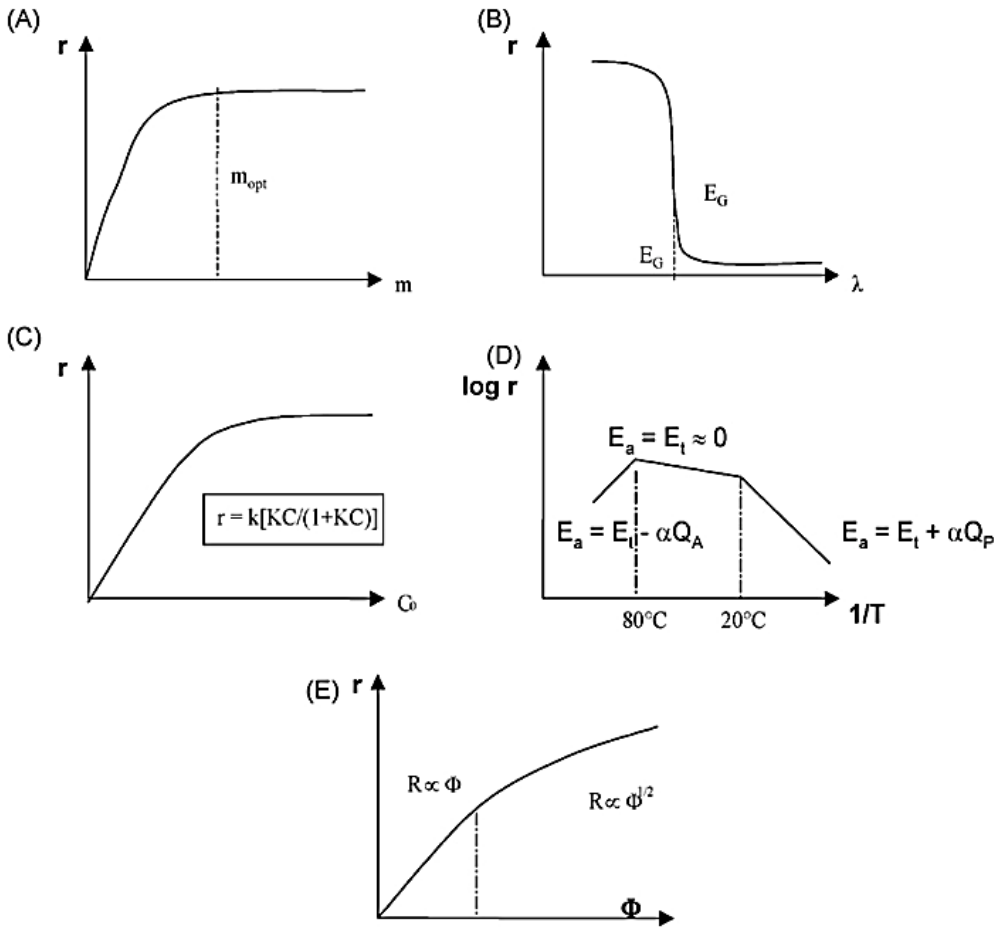

Figure 1. Influence of the different physical parameters which govern the kinetics of photocatalysis: reaction rate r; (A) mass of catalyst m; (B) wavelength λ; (C) initial concentration c of reactant; (D) temperature T; (E) radiant flux Φ (Herrmann, 2010).

2.2.1. Photocatalysis Mechanism

When the light of appropriate energy is absorbed by the photocatalyst, the exciton or electron/hole (e^-/h^+) pairs form, with electrons in the conduction band and holes in the valence band as shown in Figure 2. Depending on the environment and band edge positions relative to the redox potential of the adsorbed species, each of the charge carriers may follow various routes. Electrons induce a reduction in the conduction band while holes induce oxidation in the valance band, or both holes and electrons may recombine. Thus, the charge carriers give rise to the generation of reactive oxygen species (ROS) such as superoxide anion radicals ($O_2^{\bullet -}$), hydroxyl radicals ($^{\bullet}OH$), singlet oxygen species ($^{\bullet}O_2$), and peroxide molecules (H_2O_2) (Nosaka

& Nosaka, 2017; Ong et al., 2018). ROS have a high tendency of oxidizing organic pollutants into less toxic substances or mineralize them into CO_2, H_2O and others as shown in Figure 2.

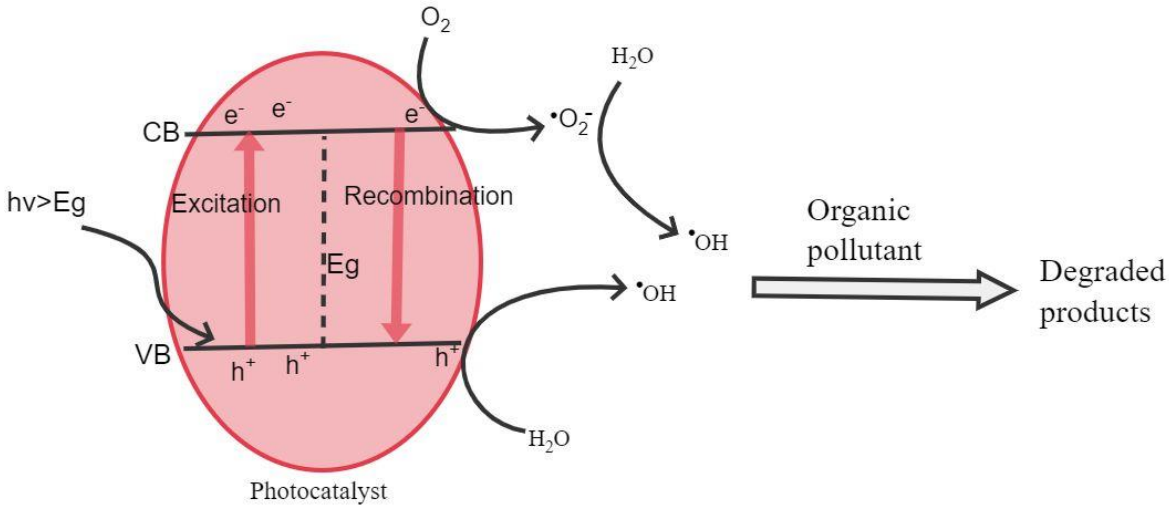

Figure 2. Mechanism of photocatalytic dye degradation (H. wa Yu et al., 2019)

Once the e^-/h^+ pairs are generated, some of the possible mechanisms of the formation of ROS and degradation of organic pollutants are given as follows based on the previous works (Shinde et al., 2017).

(i). Electrons in the conduction band transfer to the adsorbed species (e.g., oxygen, dichromate ion) and induce reduction reaction Eqn. (1-3).

$$e^- + O_2 \rightarrow O_2^{\bullet -} \quad (1)$$

$$e^- + H_2O_2 \rightarrow {}^{\bullet}OH + OH^- \quad (2)$$

$$6e^- + Cr_2O_7^{2-} + 14H^+ \rightarrow 2Cr^{3+} + 7H_2O \quad (3)$$

(ii). Holes in the valence band oxidize adsorbed species (H_2O, OH^-, pollutants (RH), etc.) Eqn. (4-6).

$$h^+ + OH^- \rightarrow {}^{\bullet}OH \quad (4)$$

$$h^+ + H_2O \rightarrow {}^{\bullet}OH + H^+ \quad (5)$$

$$h^+ + RH \rightarrow R^\bullet + H^+ \qquad (6)$$

(iii). Recombination reaction occurs if charge carriers recombine resulting in heat or light Eqn. (7).

$$h^+ + e^- \rightarrow \text{heat or light} \qquad (7)$$

Once these highly reactive species are formed ($^\bullet OH$, $O_2^{\bullet-}$, $R^\bullet$), they initiate further reactions and consequently degrade pollutants into CO_2 and H_2O or less toxic compounds Eqn. (8-17).

$$O_2^{\bullet-} + \bullet OH \rightarrow HOO^\bullet \qquad (8)$$

$$O_2^{\bullet-} + H_2O \rightarrow HOO^\bullet + OH^- \qquad (9)$$

$$O_2^{\bullet-} + H^+ \rightarrow HOO^\bullet \qquad (10)$$

$$O_2^{\bullet-} + H_2O_2 \rightarrow \bullet OH + OH^- + O_2 \qquad (11)$$

$$HOO^\bullet + e^- \rightarrow HO_2^- \qquad (12)$$

$$HOO^\bullet + H^+ + e^- \rightarrow H_2O_2 \qquad (13)$$

$$HOO^\bullet + H_2O \rightarrow H_2O_2 + {}^\bullet OH \qquad (14)$$

$$HOO^\bullet + HOO^\bullet \rightarrow H_2O_2 + O_2 \qquad (15)$$

$$^\bullet OH + RH \rightarrow R^\bullet + H_2O \qquad (16)$$

$$R^\bullet \rightarrow \text{Intermed/final Degrad. Prod.} \qquad (17)$$

$$\therefore \text{RH} \xrightarrow{\text{catalyst + hv}} \text{Intermediate(s)} \rightarrow CO_2 + H_2O + \text{inorganic products (from heteroatoms)}$$

($^\bullet OH, O_2^{\bullet-}$, $HOO^\bullet$, and H_2O_2) are reactive oxygen species.

To propose the possible photocatalytic mechanism, a trapping experiment should be done using different scavengers to explore the involvement of active species in the experiment. These active

species include electrons (e^-), holes (h^+), superoxide radical anions ($O_2^{\bullet -}$) and hydroxyl radicals ($^{\bullet}OH$) (Kumaresan et al., 2020). Thus, the most frequently used compounds (scavengers) are: (i) benzoquinone, triphenylphosphine, acrylamide or azide ion, etc. for $O_2^{\bullet -}$, (ii) isopropanol, benzoic acid, methanol, tert-butyl alcohol, etc. for $^{\bullet}OH$, and (iii) formic acid, ammonium oxalate, potassium iodide, etc. for h^+.

2.2.2. Photocatalytic Applications of ZnO NPs

Owing to its unique features, ZnO is one of the appropriate candidates for photocatalytic applications for polluted water remediation (Pirhashemi et al., 2018; Sahu & Kar, 2019; Vahdat Vasei et al., 2019). Varieties of ZnO nanostructures have been studied for photocatalytic applications over the past decades (C. Lei, Pi, Jiang, et al., 2017; Ong et al., 2018; S. Wang et al., 2018). These include nanosphere (S. M. Saleh, 2019), nanorods (T. J. Liu et al., 2013; X. Zhang et al., 2014), hexagonal plate-like (Mclaren et al., 2009), flower-like (Mao et al., 2019), and others are some of the ZnO nanostructures employed for organic dye degradation by photocatalysis method. As discussed in the previous sections, photocatalytic performance of ZnO nanoparticles is greatly affected by the features of the nanoparticles. These include size, crystal quality, morphology, defect level, and optoelectronic properties (Asadzadeh-Khaneghah & Habibi-Yangjeh, 2020; Galani & Panda, 2019; Hezam et al., 2017; Mao et al., 2019; Wong et al., 2019). Variations in these attributes can be used to tune ZnO nanostructures' photocatalytic performance.

To consider nanomaterials for photocatalytic applications, it is crucial to understand that the particle size and shape of nanomaterials can significantly affect the material's properties and performances. Mclaren *et.al*. demonstrated the effects of particle size and shape of ZnO nanocrystals on photocatalytic activity (Mclaren et al., 2009). The result indicated that for a ZnO nanocrystal, the hexagonal plate-like nanocrystals showed five times higher catalytic activities than the rodshaped crystals due to the presence of the more surface active (001) and (00-1) polar faces on the plate-like crystals compared to the nonpolar surfaces of the rod-shaped crystals. Similarly, among NPs, nanowires, and nano-thin film structures of ZnO, the NPs have shown the highest photocatalytic performances which can be attributed to the largest specific surface area of the NPs whereas the nano-thin film structures have the least of the three (Ong et al.,

2018). On top of this, ZnO nanostructures of the same shape but different aspect ratios may show different photocatalytic performances. Zhang et al, reported that the photocatalytic performance of ZnO nanorods increases with increasing aspect ratio, where the higher aspect ratio nanorods exhibit a high level of surface defects (X. Zhang et al., 2014).

Since the photocatalytic activity of the nanomaterials is highly morphology dependent, it is important to develop ZnO NPs having morphologies and surface characteristics that offer efficient performance to exploit the distinctive features of ZnO (Bathla et al., 2019; Mardikar et al., 2020; Yaqoob, Noor, et al., 2020)**.** Among the ZnO morphologies, one-dimensional nanostructure exhibits attractive features that make ZnO-based materials the potential candidate for photocatalytic applications. Liu et al. studied the photocatalytic activities of nanorods, truncated hexagonal cones, and multilayered disks of ZnO nanocrystals against methyl orange under UV irradiation (T. J. Liu et al., 2013). According to the result, the degradation rate using rod-shaped ZnO nanocrystals was found to be 99.8%, while degradation rates using truncated hexagonal cones and multilayer disks were found to be 75% and 23 %, respectively.

In photocatalytic applications, assembling 1D or 2D nanostructures into 3D hierarchical structures offers additional benefits over simple nanostructures (e.g., NPs, nanorods, nanosheets, etc.) (Arsha Kusumam et al., 2016; Mao et al., 2019). Hierarchical structures prevent agglomeration; improve reactant diffusion and kinetics, enhance charge separation and capacity of light-harvesting, high adsorption capacity, high recyclability, and so on (C. Lei, Pi, Jiang, et al., 2017; S. Wang et al., 2018). Wang *et.al*. reported that ZnO microspheres with hierarchically porous structures exhibit superior photocatalytic properties against Rhodamine B (RhB) degradation owing to their larger surface area, larger charge separation, and higher transfer efficiencies compared to nanostructures of lower dimensions (S. Wang et al., 2018). In addition, Lei *et.al*. demonstrated that hierarchical structures provide a greater degree of organic pollutant removal efficiency through adsorption (C. Lei, Pi, Jiang, et al., 2017). In a similar study, the work of Y. Mao *et.al*. revealed that the flower-like hierarchical structure of ZnO micro/nanostructures exhibited a 97.34% RhB degradation efficiency under UV irradiation with a reaction rate constant of 0.06081 min^{-1}, while other morphologies of ZnO showed lower reaction rates: nanospheres (0.02491 min^{-1}), hexagonal disks (0.03051 min^{-1}), and hexagonal bilayer disk-like structures (0.02879 min^{-1}) (Mao et al., 2019). Several other studies have also

confirmed that hierarchical ZnO micro/nanostructures are more efficient for photocatalysis (Arsha Kusumam et al., 2016; N. Zhang & Chu, 2019).

The presence of defects also greatly affects the wavelength range of absorbed light and the efficiency of the ZnO photocatalyst (Hezam et al., 2017). Particularly, oxygen vacancy defects act as self-dopants, improving the efficiency of the catalyst. Wang *et.al.* showed that increasing the concentration of oxygen vacancies in ZnO crystal results in lowering the bandgap, which in turn increases the visible light absorption leading to efficient photocatalytic degradation of 2,4-dichlorophenol using visible light (J. Wang et al., 2012). According to Hezam and co-workers' report, the oxygen vacancies enhance the performance of ZnO photocatalyst in such a way that (i) the higher concentration of vacancies lower the bandgap leading to more photon absorption, (ii) the oxygen vacancies temporarily trap the electrons lowering the rate of electron-hole recombination, and (iii) facilitate the transfer of trapped electrons to the adsorbed oxygen, resulting in superoxide ions formation (Hezam et al., 2017). The literature report on the use of ZnO nanostructures as photocatalysts for water remediation is summarized in Table 1.

Table 1.The summary of the photocatalytic activities of ZnO nanostructures

Method	Morphology	Dye	Light	Performance	Ref.
Hydrothermal and ultrasonic	flower-like microstructure	MO	simulated sunlight	100% in 60 min	(Qu et al., 2020)
Hydrothermal	flower-like microspheres	MB	UV	97% in 20 min	(Y. Wang et al., 2016)
Hydrothermally	nanoflowers	MB	solar	97% in 10 min	(Hezam et al., 2017)
Hydrothermal	flower-like microsphere	RhB	simulated sunlight	100% in 40 min	(S. Wang et al., 2018)
Solvothermal	flower-like	RhB	UV	97.34% in 60 min	(Mao et al., 2019)
Green	spherical	MO, MB, MR	UV	-	(Davar et al., 2015)
Reflux	flower-like	palm oil mill effluent	UV	96.0 in 120 min	(Wong et al., 2019)
MW-assisted	spherical	MB	UV	78% in 4 h	(Kajbafvala et al., 2012)

2.2.3. Photocatalytic Applications of ZnO-CuO NCs

Studies have demonstrated that CuO/ZnO NCs display a remarkable improvement in photocatalytic performance due to an increase in absorption in the visible light range, majority charge carrier mobility, stability, reusability, and charge separation efficiency compared to ZnO alone or CuO alone (Annathurai et al., 2019; C. Liu et al., 2019; Sahu, Bisht, et al., 2020; Sathishkumar et al., 2011; Senthil Kumar et al., 2017; Yendrapati Taraka et al., 2019). In general, the heterojunction formed between CuO and ZnO enhances charge carriers' separation and transfer which can prolong the lifetime of the photogenerated charge carriers (Yang et al., 2010; J. Zhang et al., 2008). As mentioned in the previous sections for ZnO, the performance of

CuO/ZnO nanocomposites varies with the variation in the morphology, particle size, content (molar ratio) of CuO, surface properties, and others.

The change in the optical properties of the nanomaterials may change the wavelength of the light absorbed which greatly affects the photocatalytic performance. Zhu *et al.* synthesized ZnO/CuO NCs with an improved visible light harvesting capacity compared to the pristine ZnO leading to more charge carriers generation under visible light irradiation (L. Zhu et al., 2018). The report also indicated that ZnO/CuO is twice as effective as pristine ZnO at removing phenol. Similarly, Prabhu et al. reported that CuO/ZnO nanocomposite has an enhanced photocatalytic reduction of CO_2 to CH_3OH compared to pristine ZnO under visible light irradiation (Prabhu et al., 2019). The enhancement was attributed to the increased charge separation due to the p-n heterojunction, which reduced the rate of e^-/h^+ pair recombination.

Similarly, the performance of CuO/ZnO NCs varies with the variation in the morphology, particle size, content (molar ratio) of CuO, surface properties, and others as shown in Table 2. The content (or molar ratio) of CuO affects the performance of the CuO/ZnO NCs. The optimum ratio of the highest-performing composite depends on the morphology and synthesis methods used. Sherly et al. reported that CuO/ZnO with ZnO:CuO molar ratios of 2:1 showed a maximum degradation (82%) of 2,4-dichlorophenol compared to 1:1 and 1:2 under visible-light irradiation (Sherly et al., 2015). However, the optical bandgap reported shows decreasing with an increase in the CuO molar ratio in the sample (i.e., 2.98, 2.91, and 2.89 eV for 1:1, 2:1, and 1:2, respectively). This implies that tuning bandgap alone would not guarantee a high-efficiency CuO/ZnO photocatalyst. On the other hand, hierarchical CuO/ZnO p-n heterojunction synthesized by hydrothermal method with varying CuO content showed photocatalytic activity for methanol formation in the order of ZnO:CuO molar ratios of 100:400 > 100:50>100:20 > 100:10> ZnO (Yendrapati Taraka et al., 2019). The enhanced activity of the composite over the pristine ZnO has been attributed to the decreased rate of charge carriers' recombination inferring the PL results. According to the previous studies, the decreased performance of CuO-ZnO with increased CuO content beyond the optimum value could be explained by the increased agglomeration of CuO that masks surface photoactive sites or enhance the rate of e^-/h^+ recombination (S. G. Babu et al., 2019).

Table 2. The summary of the photocatalytic activities of CuO-ZnO heterostructures

Method	**Morphology**	**CuO %**	**Dye**	**Light**	**Performance**	**Ref.**
Solution-combustion	spherical, hexagonal	50	MB	UV	97.93% in 105 min	(Rajith Kumar et al., 2020)
Green	rod/spindle/ particles	50	MB	Vis	95.6% in 120 min	(Ullah et al., 2021)
Green	spherical	0.2	MB	UV	99% in 60 min	(Thatikayala & Min, 2021)
Hydrothermal	flower-like	33	MB	solar	100% in 30 min	(Mardikar et al., 2020)
Hydrothermal	flower-like	24	MB	UV-Vis	89% in 5h	(Taufique et al., 2018)
Precipitation	sheet-like	5	MB	Vis	96.57% in 25 min	(Bharathi et al., 2019)
Hydrothermal	urchin-like	-	MB	UV	100% in 40 min	(Fang et al., 2018)
Refluxed	nanorods	-	CR, RhB	Vis	99% in 50 min, 100% in 25 min	(Senthil Kumar et al., 2017)
Hydrothermal	flower-like	-	phenol	Vis	78% in 180 min	(L. Zhu et al., 2018)
MW-assisted hydrothermal	flower-like	-	MB	solar	100 in 80 min	(Oliveira et al., 2020)

The particle size and morphology of the CuO/ZnO and individual oxides in the composite can also affect the performance of the NCs photocatalyst. It is well known that the performance of NMs is highly morphology-dependent (Bathla et al., 2019; Senthil Kumar et al., 2017). Ullah et.al reported that CuO-ZnO nanorods have shown the highest photocatalytic efficiency compared to the spindles-like and sphere-like nanoparticles against MB under visible light

irradiation (Ullah et al., 2021). 0D/3D CuO/ZnO heterostructure obtained by deposition of CuO NPs on flower-like ZnO surface showed higher photocatalytic degradation of phenol than those of the pristine ZnO and CuO under visible-light irradiation due to improved visible-light harvesting and effective charge separation (L. Zhu et al., 2018). Moreover, decreasing the size increases the surface area and thus photocatalytic performance. However, agglomeration of NPs and recovery problems limit the overall performance of very small NPs photocatalysts (Raj Pant et al., 2013). In such cases, fastening the NPs on suitable support materials improves the stability and recovery of the photocatalyst for reuse purposes. The summary of the photocatalytic activities of CuO-ZnO NCs was given in Table 2.

The schematic of the electron-hole separation under the influence of the internal electric field of a p–n heterojunction photocatalyst under light irradiation is illustrated in Figure 3.

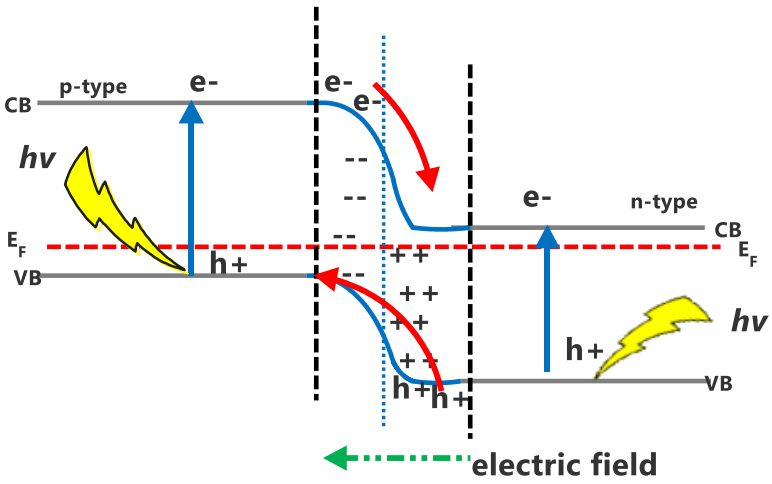

Figure 3. Schematic illustration of the electron-hole separation under the influence of the internal electric field of a p–n heterojunction photocatalyst under light irradiation (Low et al., 2017).

2.2.4. Photocatalytic Applications of ZnO-CuO-rGO

To further improve the stability, pollutant adsorptivity, and recoverability of the catalyst, employing solid catalyst supports has shown a significant improvement in the overall photocatalytic performance of NCs (Srikanth et al., 2017). The catalyst support materials need to possess certain qualities like (i) strong attachment to the photocatalysts with enhanced or

without change in performance and surface area, (ii) large surface area with a strong affinity for reactants or pollutants adsorption, and (iii) high stability against degradation in the process (Srikanth et al., 2017). Various solid support materials such as carbon nanotube, graphene, zeolite, and silica possess the required characteristics to be used for the nanostructured photocatalysts (Chandrasekaran et al., 2018; X. Liu et al., 2013; Qi et al., 2019; Y. Wang et al., 2020). These support materials increase the stability of the attached nanomaterials by avoiding agglomeration and improve the photocatalytic performance by enhancing the active surface area of the nanostructured photocatalysts. Furthermore, the photocatalysts can be recovered using filtration techniques for further application.

Among the support materials, graphene possesses unique electronic, thermal, chemical, mechanical, and surface properties (X. Li et al., 2018; Zhen & Zhu, 2017). An rGO has properties closer to that of pristine graphene. Some of the attractive properties of graphene are its large specific surface area, good electrical conductivity, excellent charge carrier mobility, and so on. Modification of metal oxides with rGO helps the catalyst stay dispersed in the aqueous solution preventing agglomeration and improving recoverability (Herring et al., 2012; Raj Pant et al., 2013). Besides, its heterogeneous nanosheet surface is a favorable site for the nucleation and growth of NPs (Herring et al., 2012; Meti et al., 2018; Ojha et al., 2017).

Metal oxide decorated rGO has applications in various areas including photocatalysis, electronics, energy storage, bio and chemical sensing, light harvesting, H_2 storage, etc. (Ansari et al., 2015). Compared to ZnO nanostructures alone, rGO-based nanocomposites have shown enhanced performance for organic pollutant degradation and antimicrobial activity (Kalantari Bolaghi et al., 2019; Raj Pant et al., 2013; Ramanathan et al., 2019), toxic metal ions reduction (X. Liu et al., 2012), disinfection, and CO_2 reduction (X. Li et al., 2013). Performance improvements have been attributed to the enhanced electron-acceptor/transport properties of rGO and the enhanced adsorption capacity of ZnO/rGO (X. Li et al., 2018). The adsorption capability increases with the rGO loading ratio. However, rGO loading beyond the optimum dosage could decrease the photocatalytic performance due to high photoabsorbing and scattering phenomena (Dou et al., 2015).

Kumaresan and coworkers prepared a flower-like shaped CuO/ZnO NCs deposited on an rGO sheet prepared by the solid-state method that has shown enhanced photocatalytic activities

against the decomposition of RhB and 4- chlorophenol under visible light irradiation (Kumaresan et al., 2020). It has been shown that modification of ZnO (E_g=3.1 eV) with a visible light sensitive CuO and good electron acceptor rGO enhanced photocatalytic performance of CuO/ZnO/rGO (E_g=2.8 eV) under visible light irradiation. According to the report, the improvements are mainly attributed to the presence of graphene, which serves as an electron collector and transporter to prolong the lifetime of the photo-generated charge carriers and due to the CuO-ZnO p-n heterojunction. Similarly, Raj Pant et al reported that Ag/ZnO/rGO NCs showed an enhanced photocatalytic activity with efficient recoverability for cyclic use (Raj Pant et al., 2013). The performance of Ag/ZnO/rGO increases with the content of rGO until the optimum is reached (Dou et al., 2015).

2.3. Catalytic Reduction

In addition to photocatalytic degradation of organic water pollutants, the nanomaterials-based catalytic transformation of pollutants into biodegradable or economically valuable low-toxicity level chemicals is also a highly desirable approach. These days, the transformation of organic compounds into the desired product efficiently in an environmentally benign manner is a major challenge. Most of the large-scale productions of organic compounds involve volatile organic solvents. In an aqueous media, this reaction occurs slowly and is not efficient for large-scale production (Satish Kumar et al., 2019). Therefore, the design and development of a sustainable and efficient way of transformation organic water pollutants are of great interest.

Nitroaromatics is one of the widely exploited compounds in the production of amino-aromatics, which serves as a potential intermediate toward the synthesis of other compounds (K. Zhang et al., 2019). While nitroaromatic compounds like 4-NP are toxic, its reduced form 4-aminophenol has a low toxicity level and has application in a variety of industries for the synthesis of drugs, dyes, and others. Thus, a transformation of 4-NP into 4-aminophenol (4-AP) in the presence of a catalyst and $NaBH_4$ as a reducing agent in an aqueous medium is highly desirable (Mandlimath & Gopal, 2011). The reduction of 4-NP into 4-AP has been practiced for years using conventional methods, which have limitations like the formation of aniline as a side product, longer duration, and extensive methodology involving usage of hydrogen gas at high temperature and pressure, etc. (Mandlimath & Gopal, 2011). Direct hydrogenation of 4-NP

using $NaBH_4$ as a reducing agent in an aqueous medium is a greener method than others, but the reaction is slow due to the sluggish self-hydrolysis of $NaBH_4$ (Mandlimath & Gopal, 2011). Noble metals and metal oxide nanostructures have been used as a catalyst to accelerate the reduction of nitro-aromatics in the presence of reducing agents like $NaBH_4$. In this regard, the use of different metal oxide-based catalysts significantly improved the reduction reaction of 4-NP into 4-AP (Adyani & Soleimani, 2019; Atarod et al., 2015; A. T. Babu & Antony, 2019; Shamsuddin & Raja Nordin, 2019).

Owing to their distinctive properties, nanostructured catalysts of metals (Pd, Pt, Ag, Ru, Rh, and Au) provide a sustainable way for the transformation of organic compounds in an environmentally benign manner in an aqueous medium (Gadipelly & Mannepalli, 2019; Nasrollahzadeh et al., 2020; Salas Orozco et al., 2019). However, the high cost and high chance of agglomeration of the bare metallic nanoparticles during reactions are serious problems that limited their large-scale application as a catalyst. One of the ways to overcome agglomeration limitations is by coupling metallic nanoparticles with suitable support material. Recently, there are increasing interest in using non-noble metal oxide semiconductor catalysts as a low-cost alternative to precious metals-based catalysts for the reduction of 4-NP (Wu et al., 2017).

ZnO is investigated extensively as a catalyst and support for several organic transformations. For instance, ZnO NPs have been used in the transformation of organic compounds like direct oxidative esterification of alcohols (Galani et al., 2018), hydrogenation of aromatic nitro compound to the corresponding amine (Galani et al., 2018), synthesis of coumarins and their derivatives (B. V. Kumar et al., 2011), synthesis of 2,3-disubstituted benzofurans (Safaei-Ghomi & Ghasemzadeh, 2017), synthesis of di-spiroindolizidine bisoxindoles (Satish Kumar et al., 2019), among others. As far as reduction of 4-NP to 4-AP is concerned, no reports have been found that use pristine ZnO NPs. It was usually noble metals or other p-type semiconductor metal oxides coupled with ZnO NPs in the reduction of 4-NP. Meanwhile, CuO NPs and catalysts have demonstrated the ability to catalyze the reduction of 4-NP alone or with other metals or metal oxides (Che et al., 2015; Chowdhury et al., 2020; Sahu et al., 2019; Shamsuddin & Raja Nordin, 2019).

The catalytic reduction mechanism for the conversion of 4-NP into 4-AP involves adsorption and transfer of electrons and protons as shown in Scheme 1. When both reactants are adsorbed

on the surface of the catalyst in aqueous media, electron transfer from BH_4^- to nitro-aromatic leading to the production of amino-aromatic (K. Zhang et al., 2019).

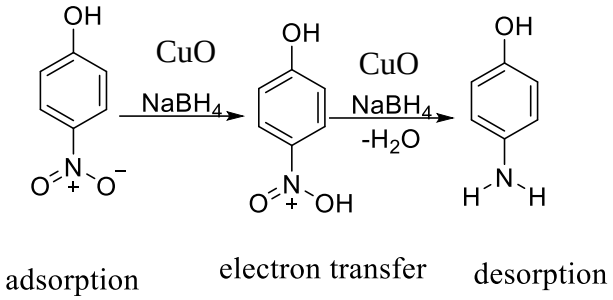

Scheme 1. Schematic mechanism of conversion of 4-NP into 4-AP by borohydride in the presence of CuO nanosheets as catalysts (Sahu et al., 2019).

2.4. Antibacterial Activities

Pollution of water with pathogenic microbes poses a severe threat to public health. Recently, the emergence of multidrug-resistant human pathogenic microbes to one or several antibiotics is a matter of great concern (Rai et al., 2012). In light of this, there is an urgent need to develop or search for new antimicrobial agents by easy, rapid, and eco-friendly routes having broad-spectrum antimicrobial activity. To this end, NMs of transition metals and metal oxides have been identified in a wide range of catalytic transformations (Chng et al., 2013). Metal NPs like noble metals-based catalysts (Pd, Pt, and Au) have become an integral part of the catalytic transformations (Galani et al., 2018). In addition, studies have shown that metal oxide-based nanomaterials also possess remarkable antibacterial activities. Some of the common metal oxide-based nanomaterials are ZnO (Chemingui et al., 2019), CuO(Zarei et al., 2020), CuO-ZnO (Nagendra et al., 2019; Rajith Kumar et al., 2020), CuO-GO (Ahmadi et al., 2021), ZnO-MnO_2-Cu_2O(Hoseinpour & Ghaemi, 2018), CdO–ZnO–MgO (Revathi & Karthik, 2018), and others (Marković et al., 2020; Ramya et al., 2019).

The antimicrobial activity of the nanomaterials depends on factors like size, stability, concentrations added, and degree of contact of the NPs with bacteria (Parham et al., 2019). ZnO NPs have shown good antimicrobial activities. The performance of ZnO NPs as antimicrobial agents can be influenced by several factors, like their morphology, particle size, exposure time,

concentration, pH, control of the reaction parameters during its preparation, and others (Parham et al., 2019; Siddiqi et al., 2018). For instance, ZnO NPs prepared by solution combustion synthesis method using plant extracts display greater antimicrobial activities compared to synthetic chemical fuels (Prashanth et al., 2019). Similarly, the antimicrobial activity of ZnO NPs decreases with the increasing annealing temperature (Azizi et al., 2016). Generally, smaller particle-sized NPs display a greater surface-to-volume ratio. Consequently, the greater surface-to-volume enhances interaction with different components of the microbes leading to better antimicrobial activity (Salas Orozco et al., 2019; Siddiqi et al., 2018). Likewise, different morphologies of ZnO have shown different performances in disinfecting microbes (Raghupathi et al., 2011). For instance, flower-like morphology ZnO nanostructures have shown enhanced antibacterial activity over nanostructures with petal-like morphology against *S. aureus, K. pneumonia,* and *E. coli* (L. K. Babu et al., 2019).

In addition to ZnO nanostructures alone, ZnO–CuO nanocomposites possess excellent antibacterial properties that could be used as an efficient material for bacteria-free water systems (Lozhkomoev et al., 2019; Malwal & Gopinath, 2017; Saravanakkumar et al., 2018; Widiarti et al., 2017). The composite of 25% CuO-ZnO showed enhanced antibacterial activity against *S. aureus* and *E. coli* compared to the ZnO NPs or CuO NPs alone (Widiarti et al., 2017). The enhanced activity was attributed due to the increased surface area and lower bandgap of the CuO-ZnO nanocomposites which improved the light absorption and adsorption properties. Similarly, it has also been reported that CuO-ZnO composite nanofibers exhibited significant antibacterial activity against *S. aureus* and *E.coli* through the release of Cu^{2+} and Zn^{2+} ions and the generation of ROS (Malwal & Gopinath, 2017). These ROS generate due to the interaction of CuO-ZnO nanofibers or their metal ions with cellular membranes leading to the leakage of intracellular materials and thus the killing of bacteria. Further study by Lozhkomoev et.al. showed that CuO–ZnO nanocomposites have shown higher antibacterial activity against *E. coli* and *S. aureus* due to the synergistic effect between CuO and ZnO in the nanocomposite (Lozhkomoev et al., 2019). The possible reason for the higher antibacterial activity of the composite compared to the mono-metal oxides could be due to the release of metal ions and the higher zeta potential of the nanocomposite which interacts electrostatically with bacterial cell wall resulting in membrane permeability change that ultimately destroys the bacteria (Lozhkomoev et al., 2019).

Plausible mechanisms of antimicrobial action

Antibacterial activity is the action whereby the NPs kill or inhibit the growth of the bacteria. Several mechanisms for their mode of action have been suggested for the antibacterial activity of NPs. To achieve antimicrobial action, the nanoparticles need to make contact with the bacterial cells (i.e. interactions between the bacteria surface and NPs) which can be facilitated through electrostatic attraction, van der Waals forces, hydrophobic interactions, and hydrogen bonding (Varier et al., 2020). Then, the NPs or the generated species (metal ions, ROS) cross into the cell membrane by diffusion which leads to the inhibition of bacterial growth or damage to cell membranes and other components of the cell. The most frequently proposed mechanisms of antimicrobial action of the nanoparticles include (i) oxidative stress by ROS (generated by photoactivation or nanomaterial-membrane interactions), (ii) release of metal ions (interact with the negatively charged cell), (iii) adsorption of small size NPs to the bacteria cell wall which would destroy the cell (leads to the leakage of cell contents), (iV) NPs that can enter the cell membrane damage vital bacterial enzyme (Azizi et al., 2016; R. Dadi et al., 2019; Gold et al., 2018; Varier et al., 2020). The pictorial mechanism of antimicrobial activity using NPs is depicted in Figure 4 (Shaikh et al., 2019).

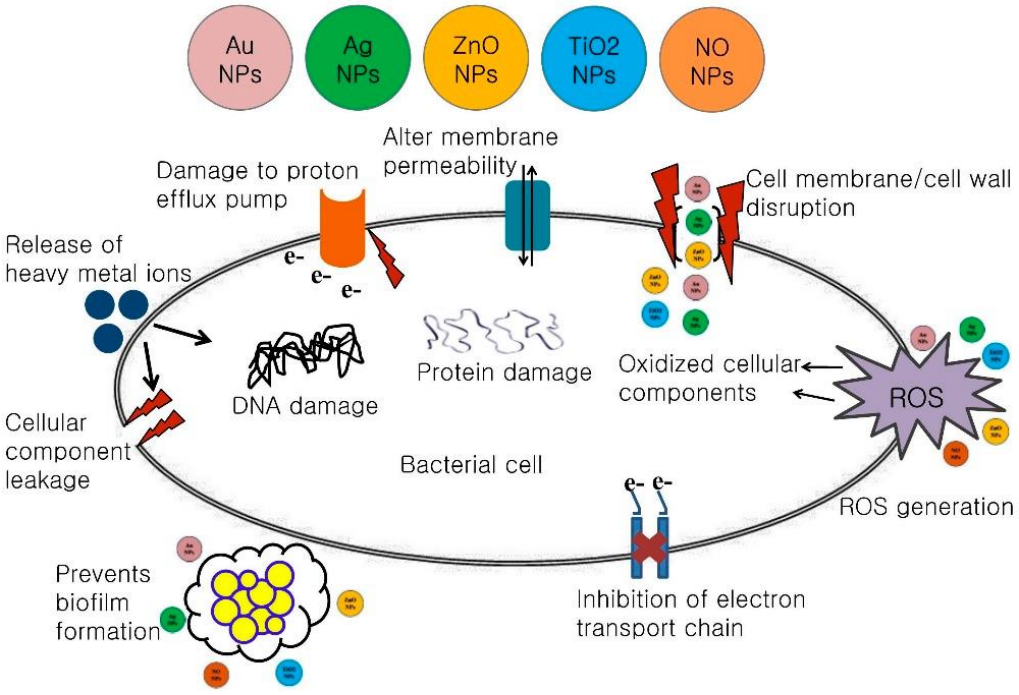

Figure 4. Possible antimicrobial mechanisms of various NPs (Shaikh et al., 2019).

2.5. ZnO and CuO-based Nanomaterials Synthesis Methods

Over the past years, diverse morphologies, sizes, dimensions, and properties of metal oxide nanostructures have been synthesized through physical, chemical, and biological routes (Ahmed et al., 2017; Fakhari et al., 2019; T. Guo et al., 2015). Among metal oxides, varieties of synthesis methods have been reported for the synthesis of CuO, ZnO, and their composites including precipitation (Velayi & Norouzbeigi, 2019), sol-gel (Vo et al., 2020), solvothermal (Podrojková et al., 2021; L. Xu et al., 2017), electrospinning (Fan et al., 2020), solution combustion (Witoon et al., 2013), photodeposition (J. Zhang et al., 2019), microwave-assisted (Pardakhty et al., 2018), electrochemical (Nur et al., 2018), thermal decomposition (R. Saravanan et al., 2013), and spray pyrolysis (Saravanakkumar et al., 2018). Since coupling rGO with metal oxide nanoparticles improves the stabilities and dispersibility of the resultant materials preventing aggregation, different methods have been reported for the synthesis of rGO decorated with CuO and ZnO. In this regard, one-step or two-step methods like hydrothermal (Tantubay et al., 2020), solid-state methods (Kumaresan et al., 2020), co-precipitation–hydrothermal (Man et al., 2020), and wet chemical-refluxing (Jyoti & Varma, 2019) methods have been reported.

The properties of the synthesized nanomaterials are significantly affected by the synthesis route followed and several experimental factors such as pH, reducing agents and stabilizing agents, calcination, annealing temperatures, nature of precursors, and concentration of precursors (Agarwal et al., 2019; Arsha Kusumam et al., 2016; Avcı et al., 2019). Under similar experimental conditions, variation in one of these parameters affects the properties and performance of the resulting nanostructure. For instance, the effect of precursor concentration of Zn^{2+} ions on the morphology of the resulting nanostructure was reported by Avci and co-workers, where flower-like and rod-like ZnO were obtained under MW-assisted hydrothermal synthesis methods using different [Zn^{2+}], 0.02 M for a flower-like structure and 0.04 M for a rod-like structure (Avcı et al., 2019). Similarly, the use of different reagents and experimental conditions could also lead to materials with different morphologies. Arsha *et.al*. prepared rice-like short ZnO nanorods using a solvothermal method with polyvinylpyrrolidone as a capping agent, flower-like ZnO structures using cetyltrimethylammonium bromide-assisted hydrothermal synthesis, and hexagonal pyramid using direct heating of zinc nitrate hexahydrate precursor (Arsha Kusumam et al., 2016). In addition, Ullah *et.al.* synthesized CuO-ZnO NCs

having nanorods, spindles-like, and sphere-like nanoparticles using waste extract of cauliflower, potato peels, and pea peels, respectively (Ullah et al., 2021). As a possible explanation, the different nature of the reagent used might have caused the variation in morphology. Furthermore, varying the synthesis parameters like time and temperature of the reaction greatly affects the morphology of the resulting product (Agarwal et al., 2019).

In addition to the methods used, the choice of the reagents greatly affects the yield and properties of the resulting nanostructures. These days, researchers are working on processes that involve a green approach to nanomaterials synthesis complying with the green chemistry principles. These include the use of low toxicity level reagents with simple, fast, and low power consuming techniques like a microwave (MW) assisted methods (Paristiowati et al., 2019; Sharifi et al., 2021).

2.5.1. Green Synthesis Method

In order to benefit from the full potential of nanomaterials, their fabrication strategies need to be simple, fast, economical, and eco-friendly. However, most of the conventional techniques suffer from at least one of the limitations due to the high energy demand, sophisticated instruments involved, and the use of toxic and hazardous chemicals that have adverse effects on the environment and human health (Annathurai et al., 2019; M. Khan et al., 2015; Yulizar et al., 2018). Consequently, there is a need for green synthesis routes that can alleviate these limitations fully or partially. A green chemistry approach encourages the use of cheap, environmentally benign chemical substances and waste-free methods that eliminate chemical waste (Paristiowati et al., 2019). That means synthetic methods should be designed to use and generate substances with very low or no toxicity to humans and the environment as much as possible (Paristiowati et al., 2019). Among the biological methods, phytochemicals-based synthetic technique received special attention for it employs simple procedures, eco-friendly and easily available raw materials, and scalable methods (Annathurai et al., 2019; M. Khan et al., 2015; Prashanth et al., 2019). In addition, phytochemical-based synthesis of NPs avoids the need for high pressure, high energy, high temperature, and toxic chemicals (Nasrollahzadeh, Sajjadi, et al., 2019).

Phytochemicals-based nanomaterials synthesis makes use of extracts from different parts of a plant (e.g. leaves, stems, fruit peels, seeds, roots, and flowers). Plant extracts are promising alternatives to the harsh chemicals usually used for reduction and stabilization (Nasrollahzadeh, Atarod, et al., 2019). Plant extracts contain varieties of phytochemicals that serve as both reducing and stabilizing agents. These phytochemicals include both primary metabolites such as amino acids, carbohydrates, and secondary metabolites such as alkaloids, phenolic compounds (phenolic acids, lignans, tannins, flavonoids), terpenoid compounds (limanoids, carotenoids), etc. (Basnet et al., 2018; Venu et al., 2019). Among these, polyphenolic compounds contain a large number of readily oxidizable hydroxyl groups. This property of polyphenols and other phytochemicals helps in the reduction of metal ions into metals and GO into rGO, and also forms a complex with metal ions that can easily be hydrolyzed to metal hydroxides (Liao et al., 2011). Furthermore, due to their functional groups and structures, phytochemicals stabilize the nanostructured particles as they form and thus increase the dispersibility of the NPs (Basnet et al., 2018; Kar et al., 2018). In most cases, the phytochemicals promote the formation of smaller particles compared to other methods under the same reaction conditions (Mohammadi-Aloucheh et al., 2018a). Over the years, extracts obtained from various plants have been utilized for the synthesis of NPs of metals (X. Zhang et al., 2014), metal oxides (Siripireddy & Mandal, 2017), metal oxide nanocomposites (Mohammadi-Aloucheh et al., 2018a), and reduction of graphene oxide (GO) into rGO (M. Khan et al., 2015). ZnO (*Nasturtium officinale*) (Bayrami et al., 2019), CuO (*Stachys Lavandulifolia*) (Veisi et al., 2021), Ag/Fe_3O_4/RGO (*Punica Granatum*) (Adyani & Soleimani, 2019), ZnO/CuO (*Mentha longifolia*) (Mohammadi-Aloucheh et al., 2018a), Cr_2O_3/ZnO (*Eichhornia crassipes*) (Zelekew et al., 2021), Pd/RGO/Fe_3O_4 (*Withania coagulans*) (Atarod et al., 2016), $CuFe_2O_4$ (*Morus alba* L.) (Cahyana et al., 2021), Au/CuO/ZnO (*Verbena officinalis*) (Dobrucka et al., 2021) and others are among the nanomaterials synthesized using plant extracts for varieties of applications. The resulting NPs are usually eco-friendly, less expensive, and free of chemical contaminants for medical and biological applications (Hussain et al., 2016).

Recent literature data show that the interest of researchers in the green method of nanomaterials synthesis is growing, one of which is the biological synthesis method. As shown in Figure 5, the number of publications that involve the synthesis of nanostructures using green sources is growing over the past years. Over the past decades, varieties of nanomaterials consisting of

oxides of Cu, Zn, or their composite have been fabricated by a phytochemical-assisted green method due to the easiness of oxide formation, and abundant availability. The resulting oxides and composites have wide applications in photocatalysis, catalytic reduction of organic dyes, antimicrobials, and others. Some of the nanomaterials of ZnO, CuO, and CuO-ZnO-based obtained using plant extracts were given in Table 3.

Figure 5. Progress in the synthesis of nanostructures using green sources (Nasrollahzadeh, Sajjadi, et al., 2019).

In phytochemical-based synthesis, the concentration of the extract, nature of plant extracts, nature of precursors, experimental parameters (temperature, time pH, etc.), and the protocol followed affect the quality, morphology, size, surface microstructure, and other properties of the NMs produced which in turn influence their applications (Basnet et al., 2018; Husen & Iqbal, 2019). In most cases, higher concentrations of the plant extract favor the formation of smaller NPs. Different structures of NPs of various morphologies, sizes, and defects have been reported with extracts from different plants due to the variation in phytochemical constituents and concentration the plants contain (Basnet et al., 2018; Stan et al., 2015). For instance, Logaranjan et al. used the *Aloe vera* gel as a shape-directing agent for the growth of Ag NPs under MW irradiation (Logaranjan et al., 2016). On the other hand, employing extracts from different plants

may have different reaction sites for adsorption, and consequently variable performance. In general, extracts containing phytochemicals with a large number of reducing and stabilizing functional groups play a significant role in the synthesis of different NMs including ZnO (Siripireddy & Mandal, 2017), rGO (X. Zhu et al., 2017), CuO/ZnO (Mohammadi-Aloucheh et al., 2018a), ZnO/rGO (Ramanathan et al., 2019), and others.

Table 3. CuO and ZnO-based nanomaterials synthesized using various plant extracts.

Nanomaterials	**Plants used**	**Application**	**Morphology**	**Ref.**
ZnO/CuO	*Theobroma cacao*		spherical, rice like	(Yulizar et al., 2018)
ZnO/CuO	*Mentha longifolia*	antibacterial	spherical	(Mohammadi-Aloucheh et al., 2018a)
CuO	*Stachys lavandulifolia*	reduction	spherical	(Veisi et al., 2021)
CuO-ZnO	*Vaccinium arctostaphylos* L	antibacterial	spherical	(Mohammadi-Aloucheh et al., 2018b)
CuO-ZnO	*Melissa Officinalis* L.	reduction	spherical	(Bordbar et al., 2018)
CuO-ZnO	*Ginkgo biloba*	photocatalytic, antibacterial	globular	(Thatikayala & Min, 2021)
CuO/GO	sugar cane juice	antioxidant	urchin-like nanospheres	(Bhattacharjee et al., 2020)
ZnO	lemon juice and citric acid	antimicrobial, antioxidant	spherical	(Prashanth et al., 2019)

The mechanism underlying plant-mediated synthesis of NPs depends on the phytochemicals constituents, their concentrations in the plant extract, and the synthesis route followed (Can, 2020; Nasrollahzadeh, Atarod, et al., 2019; P. Singh et al., 2016). Reports on the plausible mechanisms proposed for the phytochemical-based synthesis of metal oxides NPs show variations. For instance, when aqueous solution of zinc salt is mixed with the plant extract,

reactions occur between Zn(II) ions and the most active and abundant phytochemicals in the extract (Basnet et al., 2018). Two of the proposed mechanisms of reactions reported using different plants as the source of the phytochemicals are illustrated in Schemes 2-4 (Ambika & Sundrarajan, 2015; Sutradhar & Saha, 2016; Yuvakkumar et al., 2014).

(i) Zinc ion forms a complex with phytochemicals through donation of π electrons from oxygen-containing functional groups in a ligand which is followed by the formation of $Zn(OH)_2$ under hydrolysis reaction (Ahmed et al., 2017; Ogunyemi et al., 2019). Then after, $Zn(OH)_2$ converts to ZnO NPs upon heat treatment (calcination). Typical examples are shown in Schemes 2 and 3 for the formation of ZnO NPs using phytochemical extracted from *Vitex negundo* (Ambika & Sundrarajan, 2015) and *Nephelium lappaceum L*. (Yuvakkumar et al., 2014).

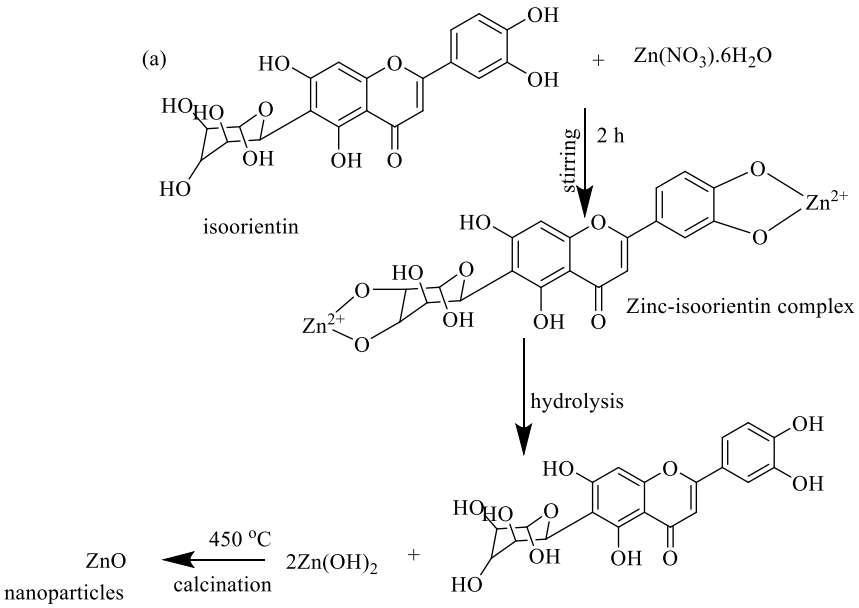

Scheme 2. Possible mechanism of ZnO NPs formation using *Vitex negundo* extract (Ambika & Sundrarajan, 2015).

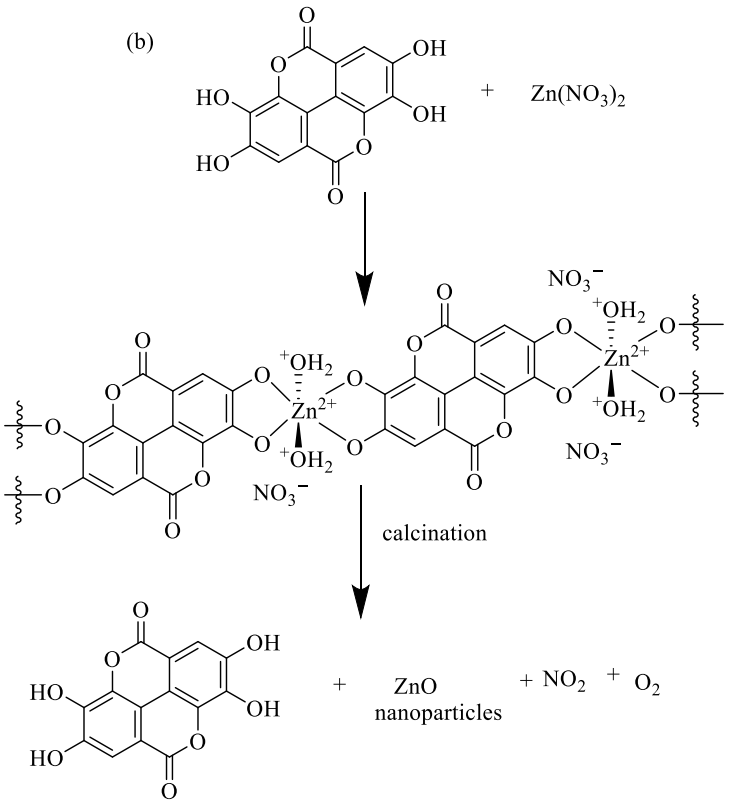

Scheme 3. Possible mechanism of ZnO NPs formation using *Nephelium lappaceum L*. extract (Yuvakkumar et al., 2014).

(ii) Phytochemicals reduce zinc ions to Zn(0) NPs, and then Zn(0) converts to ZnO upon calcination (Sutradhar & Saha, 2016). Representative examples of this reaction mechanism have been proposed for the formation of ZnO NPs using L-ascorbic acid obtained from tomato extract as depicted in Scheme 4, where zinc ions reduce to Zn(0) (Sutradhar & Saha, 2016).

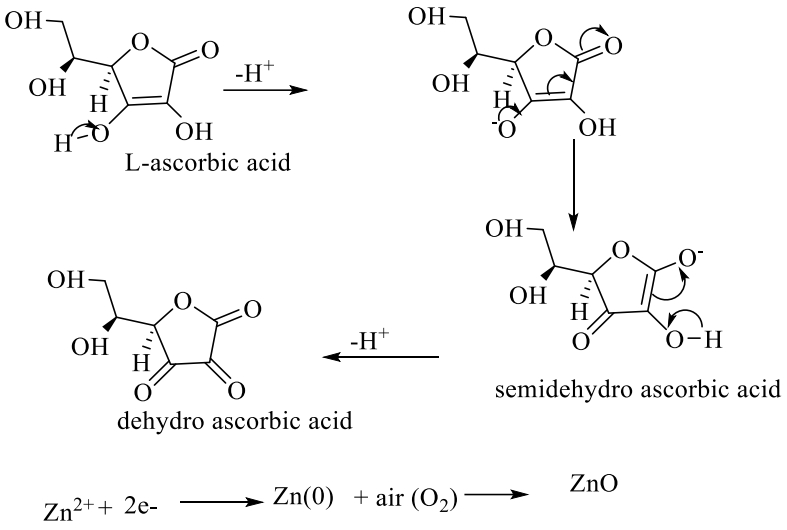

Scheme 4. Mechanism of formation of ZnO NPs using tomato extract (Sutradhar & Saha, 2016).

Combining biological synthesis methods with other techniques such as the MW irradiation synthesis method that proceed at a faster rate at relatively low temperatures could reduce the time required for the NPs synthesis (Joseph & Mathew, 2015).

2.5.2. Microwave-assisted Synthesis

MW-assisted nanomaterial synthesis is a wet-chemical approach that makes use of MW electromagnetic radiation where materials absorb MW radiation and convert it into heat. In MW-assisted nanomaterials synthesis heating is triggered by dipole polarization and/or ionic conduction mechanisms as depicted in Figure 6. When MW irradiation is applied to the sample, the dipoles try to align themselves in the direction of the applied electric field. Dipoles in the oscillating electric field lose energy in the form of heat through molecular friction and dielectric loss (dielectric heating) (T. A. Saleh et al., 2017).

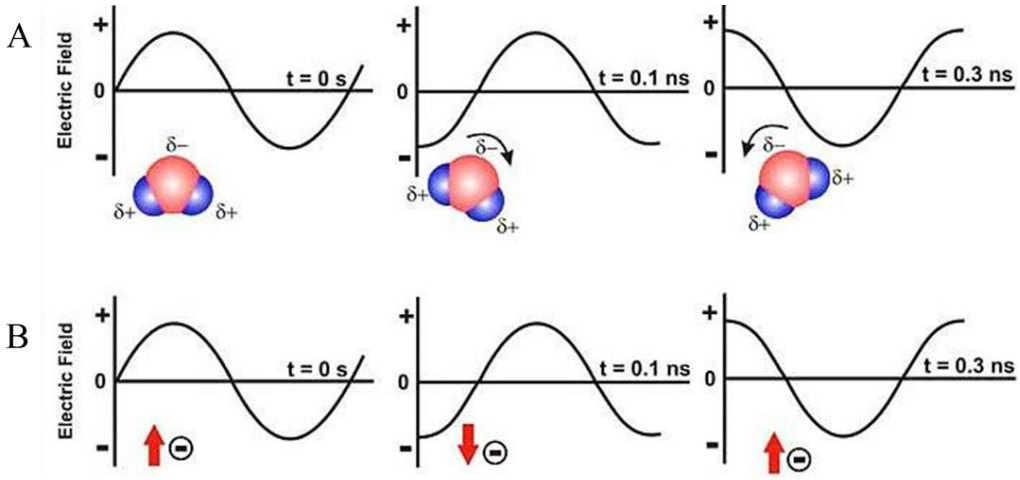

Figure 6. Two main heating mechanisms under MW irradiation: (A) dipolar polarization; (B) ionic conduction mechanism (T. A. Saleh et al., 2017).

Reports suggest that MW-assisted nanomaterials synthesis techniques possess several attractive features compared to conventional methods (Delsouz Khaki et al., 2018; Duan et al., 2015; Isık et al., 2019; Thakur & Karak, 2015). Among these qualities, (i) it provides a rapid uniform heating process throughout the whole sample, (ii) it is energy-efficient, (iii) it promotes small particle size and narrow particle size distribution, and (iv) it provides higher yields within very short reaction times, and (v) better control over the size and shape by tuning reaction parameters.

Varieties of metal NPs, metal oxide NPs, and metal oxide-based nanomaterials have been synthesized by MW-assisted synthesis methods such as TiO_2 (Kato et al., 2019), Ag, Cu, CuO, and SnO (Długosz & Banach, 2020), ZnO (Arellano-Cortaza et al., 2021; Thamima & Karuppuchamy, 2015), ZnO–NiO and ZnO–SnO_2 (Rajeswari et al., 2018), TiO_2-rGO (X. Liu et al., 2011), rGO-$BiVO_4$ (Yan et al., 2013), Ag/ZnO–TiO_2 (L. Li et al., 2014), CuO (Bhattacharjee & Ahmaruzzaman, 2018; Hashimi et al., 2020; Theophil Anand et al., 2019), Ag (K. Ali et al., 2015), CdO–NiO–ZnO (Karthik et al., 2018), ZnO–rGO (Jana & Gregory, 2020), and CuO/rGO (Yin et al., 2019). Different morphologies, crystallinity, and structures have been fabricated utilizing different synthesis protocols. Parameters including MW power, temperature, sample mass, pH, and nature of reagents are factors affecting the MW-assisted synthesis of NPs (T. A. Saleh et al., 2017).

Generally, using reagents that are good absorbers of MW requires less overall energy for NPs synthesis due to selective dielectric heating (Duan et al., 2015). For example reduction of GO to rGO by MW-assisted method enhances the rate of reduction due to the good MW irradiation absorbing nature of GO (Herring et al., 2012). Similarly, the time of irradiation depends on the MW power input and sample mass, which determine the reaction temperature. M. Hasanpoor et al. fabricated ZnO nanostructures having flower-shaped, needle-shaped, and spherical morphologies at different power, time of irradiation, and precursors (Thamima & Karuppuchamy, 2015). Similarly, M. Arellano-Cortaza *et al*. synthesized ZnO nanoparticles of different morphologies (semi-spherical shape, rod-like, and disk-like) through a simple MW-assisted method at different pH values of the reaction mixture for the photocatalytic application (Arellano-Cortaza et al., 2021). In addition, Bhattacharjee *et al*. also reported that CuO nanoleaves were obtained by MW-assisted method using glutamic acid as a complexing/capping agent for use as a catalyst for the reduction and degradation of hazardous organic compounds (Bhattacharjee & Ahmaruzzaman, 2018). Furthermore, ZnO–NiO NCs having nanorod and nanotube-shaped morphologies synthesized by MW-assisted method were also reported for use in photocatalytic degradation of RhB under UV irradiation (Rajeswari et al., 2018). K. Karthik *et al*. also reported the fabrication of CdO–NiO–ZnO nanosheets by MW-assisted method for photocatalytic and antibacterial activities (Karthik et al., 2018).

The use of MW-assisted synthesis in the presence of plant extracts significantly increases the yield of NPs (Yallappa et al., 2013). In addition, MW irradiation accelerates the synthesis of biogenic-based NPs making the method environmentally friendly, economical, and quick. For instance, K. Ali *et al*. biosynthesized Ag NPs using *Eucalyptus globulus* extract under MW irradiation for 30 s (K. Ali et al., 2015). Also, the properties and morphologies of the nanostructures obtained under MW heating differ from that obtained under conventional heating. Using *Pedalium Murex* plant extract as the bio-reducing agent, Babitha *et al*. synthesized ZnO NPs (crystallites size = 12.52 nm, and E_g=3.42 eV) under MW heating, and ZnO nanosheets (crystallites size = 18.48 nm, and E_g=3.23 eV) under modified sol-gel methods (Babitha et al., 2018). According to this report, ZnO NPs with smaller particle sizes showed higher photocatalytic performance against MB degradation than ZnO nanosheets.

CHAPTER THREE

3. MATERIALS AND METHODS

3.1. Chemicals and Reagents

All the chemicals and reagents used were analytical grade. copper (II) acetate monohydrate ($Cu(CH_3COO)_2$. H_2O), (99%, UNI-CHEM), sodium hydroxide (NaOH), (98%, Loba), zinc (II) acetate dihydrate (($Zn(CH_3COO)_2.2H_2O$), (99%, UNI-CHEM), copper (II) nitrate trihydrate ($Cu(NO_3)_2.3H_2O$), (99%, UNI-CHEM), sodium borohydride ($NaBH_4$), (95%, SRL), methylene blue ($C_{16}H_{18}ClN_3S.3H_2O$), (PJ), sulfuric acid (H_2SO_4), (Loba, 98%), Graphite powder (C), (Blulux, 99.5%), orthophosphoric acid (H_3PO_4), (Loba, 75%), potassium permanganate ($KMnO_4$), (alpha, 99.5%), ascorbic acid ($C_6H_8O_6$), (SRL, 99%), polyethylene glycol 200 (Loba), hydrochloric acid (HCl), (35.4%, Loba), hydrogen peroxide (H_2O_2), (Fine chemicals, 30%) were used.

3.2. Apparatus and Instruments

The apparatuses used throughout the experiment includes glassware (beakers, Erlenmeyer flasks, volumetric flasks, funnel), centrifuge tube, mortar and pestle, measuring cylinder, thermometer, etc. similarly, the instruments used include microwave oven, air drying oven, muffle furnace, centrifuge, hot plate, pH-meter, electroanalytical balance, electric grinder, etc.

3.3. Plant Extract Preparation

The leaves of *Cordia africana* Lam. and *Verbascum Sinaiticum* Benth. were collected from Adama Science and Technology University campus and its surroundings, Adama, Ethiopia. In the preparation of solutions and for washing activities, deionized water (DW) was utilized throughout the experiment.

The leaves of *Cordia africana* Lam. (Figure 7A) were washed thoroughly several times with tap water and DW sequentially to remove dust particles from the surface of the plant and then allowed to air dry. Then, the dried leaves were ground using a grinder. 20 g leaf powder and

200 mL DW were mixed in a 1000 mL conical flask and stirred for 20 min. Then, the mixture was heated up to boiling (~95 °C) and allowed to boil for 10 min under stirring. After cooling to room temperature, stirring continued for 20 min, and then filtered to obtain an extract using Whatman No. 1 filter paper. The resulting extract was stored at about 4°C for further use (Basnet et al., 2018).

Verbascum sinaiticum Benth. plant (Figure 7B) extract was prepared under similar experimental conditions by mixing 10 g powder of *Verbascum sinaiticum* Benth. and 100 mL of DW. The extracts were labeled as CAL for *Cordia africana* Lam. extract and VSB for *Verbascum sinaiticum* Benth extract.

Figure 7. Photographs of plants leave (A) CAL and (B) VSB.

3.4. Synthesis of Nanomaterials

3.4.1. Synthesis of CuO and ZnO NPs using Plant Extracts

CuO NPs were prepared by MW-assisted method using *Cordia africana* (CAL) and *Verbascum sinaiticum* Benth (VSB) extracts (Shaalan et al., 2016). In a typical procedure, 100 mL of 0.310 M aqueous solution of $Cu(CH_3COO)_2.H_2O$ was transferred to a 1000 mL beaker containing and stirred for 20 min. Then, 10 mL of the extract was added to the

$Cu(CH_3COO)_2.H_2O$ solution under stirring. To adjust the pH NaOH (20 wt%) aqueous solution was added drop-wise while stirring. After 20 min of stirring, the mixture was placed into a domestic microwave (MW) oven with a maximum power of 1000 W, and only 50% power output was used for 9 min. The brown precipitates were collected and washed with DW and ethanol sequentially. Finally, the residue was dried at 80 ºC for 12 h, and then at 100 ºC for 2 h. The dried powder was ground using a mortar and pestle. Other CuO samples were also prepared by using 30 mL and 50 mL extract in similar fashion. CuO obtained using CAL was labeled as CuO(L-X) and that of VSB was labeled as CuO(B-X (where X represents the mL of extract used). The flow chart of the synthesis of the CuO NPs using extracts was shown in Figure 8.

Similarly, ZnO NPs were prepared by repeating the procedures and extract volumes used for CuO NPs synthesis replacing $Zn(CH_3COO)_2 \cdot 2H_2O$ (100 mL of 0.310 M) for $Cu(CH_3COO)_2 \cdot H_2O$. The ZnO sample obtained using CAL was labeled as ZnO(L-X) and that of VSB was labeled as ZnO(B-X) (where X represents the mL of extract used). Finally, the resultant CuO NPs and ZnO NPs were employed for the reduction of 4-NPs, and the best-performing NPs were identified for further characterization and analysis.

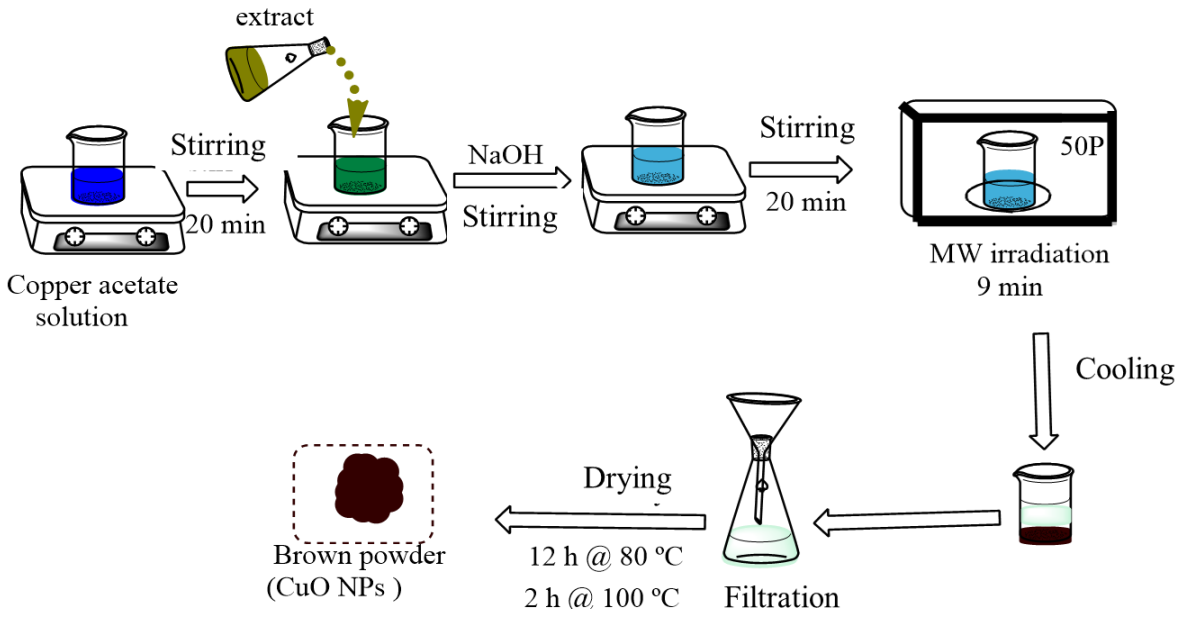

Figure 8. Flow chart for the synthesis of CuO NPs by MW method using CAL and VSB extracts.

3.4.2. Synthesis of CuO-ZnO NCs using Plant Extracts

CuO-ZnO NCs were synthesized by MW-assisted method using $Zn(CH_3COO)_2.2H_2O$ and $Cu(CH_3COO)_2 \cdot H_2O$ metal precursor with CAL and VSB following the reported procedures with some modifications in the amount of precursors used (Mohammadi-Aloucheh et al., 2018b). Typically, 5.0 g $Zn(CH_3COO)_2 \cdot 2H_2O$ and 1.25 g $Cu(CH_3COO)_2.H_2O$ were dissolved in 100 mL DW and heated at 75 °C under stirring. While it is being stirred, 50 mL extract was slowly added to the solution. NaOH (20 wt%) was used for adjusting the pH to 10 and then stirred for 20 min. Subsequently, the mixture was irradiated using a household oven (1000 W, Comet) for 10 minutes at 50% power output. After washing with DW and ethanol, the brown precipitate obtained was dried at 80 °C for 12 h. A pestle was used to hand-crush the resultant solid. Eventually, calcination of the powder was conducted at 500 °C for 3 h using muffle furnace. The resulting product was a 20 wt% CuO content sample. For comparison, other CuO-ZnO samples with CuO contents of 10%, 30%, and 50% by wt% were prepared using the solution containing (0.257 M, 0.194 M, and 0.139 M) zinc (II) acetate dihydrate and (0.033 M, 0.095 M, and 0.150 M) copper (II) acetate monohydrate, respectively. To each of these mixtures, 50 mL extract was added. The remaining procedures were similar to that of the 20 wt% CuO. In addition, pristine ZnO and pristine CuO NPs were also prepared using 100 mL of 0.290 M $Zn(CH_3COO)_2.2H_2O$ and 100 mL of 0.290 M $Cu(CH_3COO)_2 \cdot H_2O$, respectively.

The CuO-ZnO sample with 'X' wt% CuO obtained using CAL was labeled as CuO-ZnO(L)-X% and that of VSB was labeled as CuO-ZnO(B)-X%, where 'X'=10, 20, 30, and 50. Similarly, pristine ZnO and CuO obtained using CAL were labeled as ZnO(L) and CuO(L), while those obtained using VSB were labeled as ZnO(B) and CuO(B). Each of the synthesized samples was tested for photocatalytic degradation of MB and the best-performing sample was used in the subsequent analysis. An overview of CuO-ZnO NCs synthesis using VSB was shown in Figure 9 concisely.

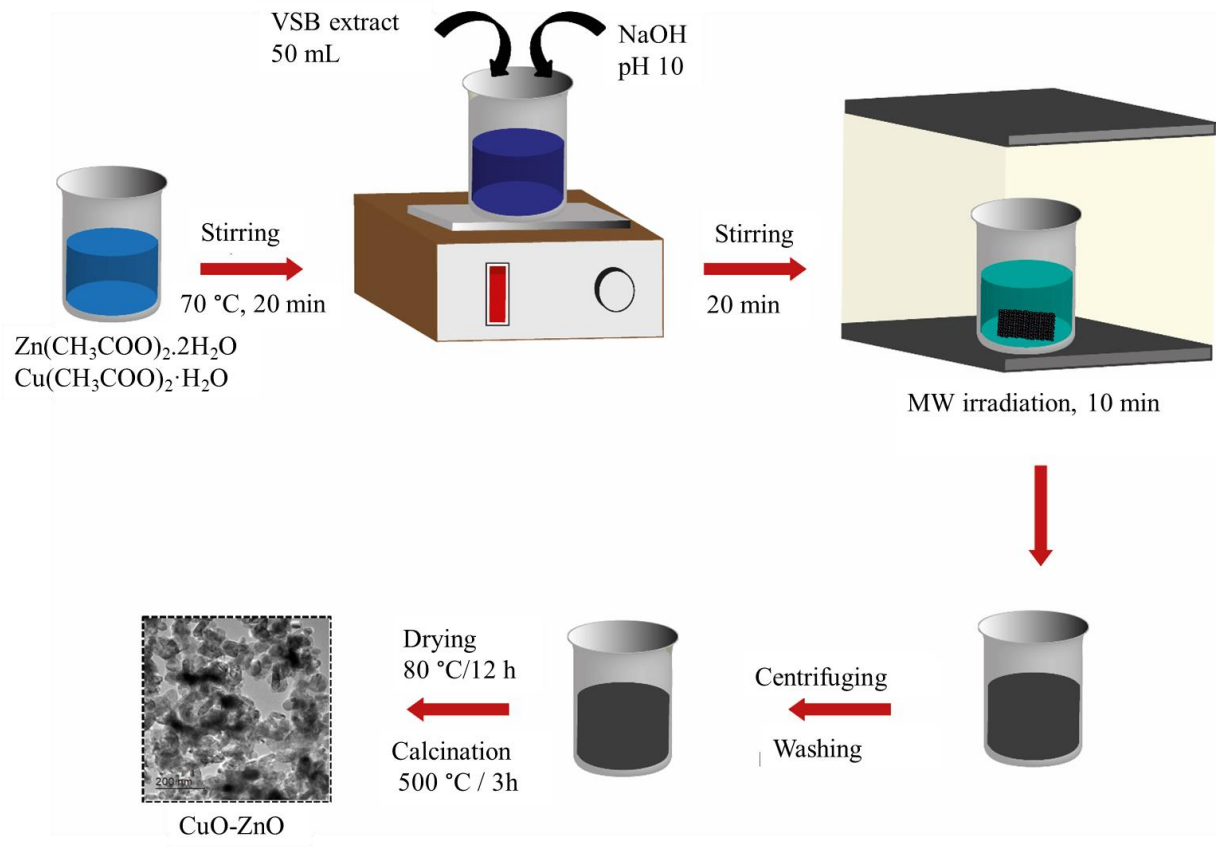

Figure 9. Schematic diagram of MW-assisted CuO-ZnO NCs synthesis using VSB.

3.4.3. Synthesis of GO and rGO

Synthesis of GO

GO was synthesized using an improved Hammer's method according to the following procedures (Zaaba et al., 2017). Briefly, 1 g of graphite powder was added to a 160 mL mixture of H_2SO_4 and H_3PO_4 (volume ratio 9:1) in the ice bath under magnetic stirring. After 30 min of stirring, 6 g of $KMnO_4$ was slowly added to the mixture keeping the temperature below 10 °C using the ice bath. After that, the whole content was stirred for 12 h at a temperature between 35 to 40 °C. To the resulting mixture, 100 mL DW was added slowly under stirring to start oxidation. DW should be added slowly for the reaction is extremely exothermic accompanied by gas evolution/effervescence; the slow addition produces more oxidized graphene avoids destructive oxidation (Luo et al., 2019). Then, an additional 100 mL of DW was added instantly to oxidize the graphite left unoxidized. Eventually, 5 mL H_2O_2 was added to the mix and stirred

for 10 min which resulted in a yellowish solution. The yellow suspension was cooled to room temperature and left standing for 12 h. The supernatant was decanted and the residue was washed repeatedly with DW and finally with ethanol. The resulting brown residue was dried at 60 °C for 12h.

Synthesis of rGO

Ascorbic acid was used to reduce graphene oxide according to the procedure described elsewhere with some modifications in quantities of the reagents used (De Silva et al., 2018). GO dispersion (0.2 mg/ml) was prepared in DW and ethanol mix (with 8:2 volume fraction H_2O/CH_3CH_2OH) utilizing ultrasonication for 1 h. To the resulting 400 mL dispersion, 1.2 g of ascorbic acid was added and stirred for 20 minutes. The pH of the medium was adjusted to 10 by NH_3 aqueous solution. Next, the mixture was subjected to MW-irradiation for 15 minutes at 50% of the 1,000-watt output power oven. Subsequently, the black suspension was left to stand still for 6 h to settle the rGO. To purify the resulting product, the residue was filtered and washed well with DW repeatedly until the filtrate pH reaches 7, and then with ethanol. Lastly, the residue was dried at 80 ºC overnight. The schematic diagram was shown in Figure 10.

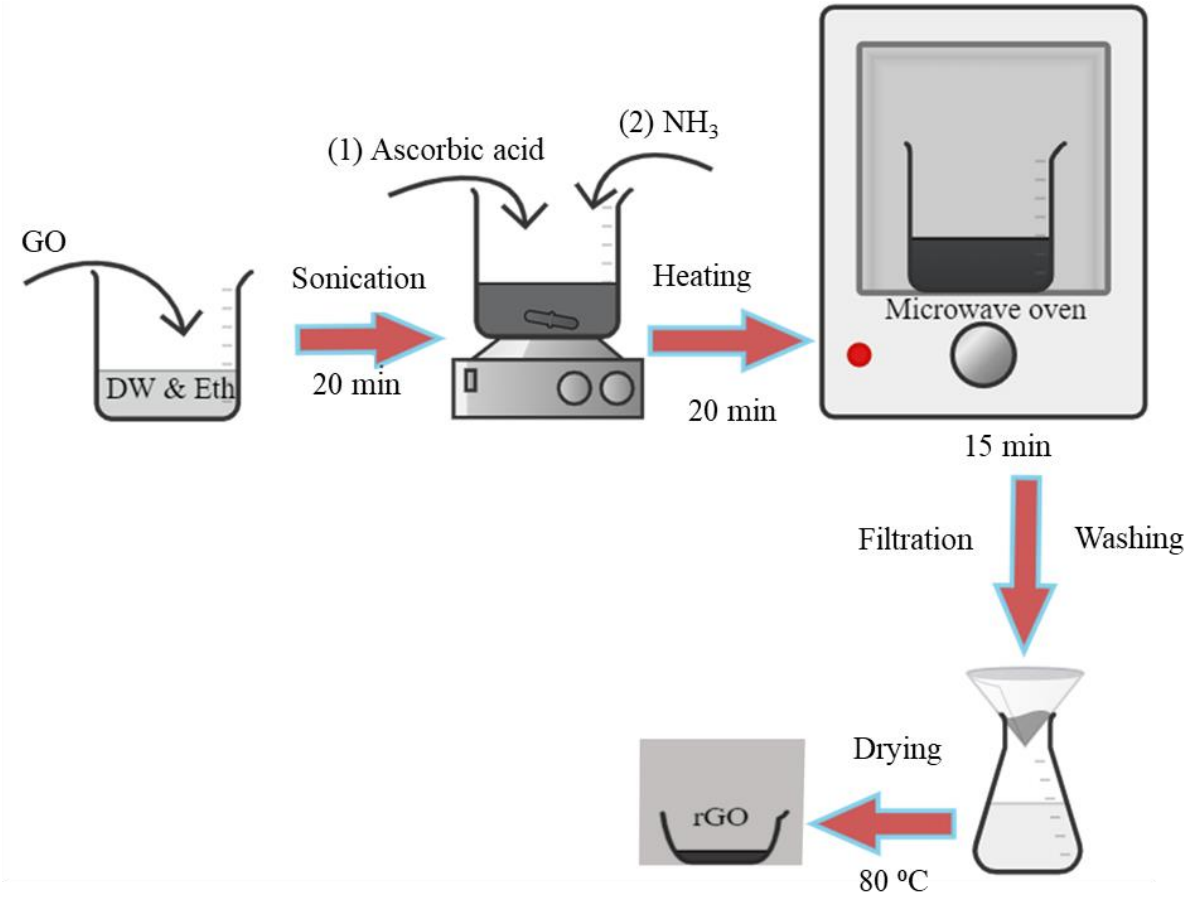

Figure 10. Schematic diagram of MW-assisted reduction of GO to rGO using ascorbic acid (numbers (1) and (2) indicate the sequence of addition).

3.4.4. Synthesis of rGO-ZnO/CuO NCs using PEG

To synthesize rGO-ZnO/CuO NCs, the following procedure was adopted. First, 80 mg rGO was dispersed in a 150 mL mixture of DW and ethanol in a 2:8 ratio under sonication for 30 min. To this dispersion, 50 mL of 0.225 M $Zn(CH_3COO)_2.2H_2O$ was added and then stirred for 20 min at 70 ^{0}C. Then, the pH was adjusted to 10 by NaOH (20 wt%) (Prakash et al., 2013). The resulting greyish-white suspension was put in the microwave oven and irradiated for 10 min at 50% of the 1000-watt output power oven. After cooling to room temperature, the content was stirred for 20 min at 70 ^{0}C. To this suspension, 12 mL $(Cu(NO_3)_2.3H_2O)$ (0.225 M) and then 10 mL polyethylene glycol (PEG-200) were added drop by drop sequentially. The pH was adjusted to 10 by NaOH (20 wt%). The resulting greyish solution was further MW irradiated for 10 min. Finally, the resultant precipitate was washed with DW and, then with ethanol. The residue was

dried at 80 ^{0}C for 6h and then at 200 ^{0}C for 2h in the oven. The resulting product was labeled as rGO-ZnO/CuO(P). For comparison, CuO-ZnO NCs and ZnO NPs were prepared. Hence, the same route was followed as that of rGO-ZnO/CuO (P) except (i) without the step for the addition of rGO (to prepare CuO-ZnO) and (ii) without the step for the of rGO and without adding $Cu(NO_3)_2.3H_2O$ (to prepare ZnO). The products obtained were labeled as CuO-ZnO(P) for CuO-ZnO and ZnO(P) for pristine ZnO. Following a procedure different from that of rGO-ZnO/CuO(P) synthesis, rGO-ZnO/CuO(P2) was prepared. Typically, a mixture of 80 mg rGO (sonicated in 150 mL water-ethanol mix), 50 mL of 0.225 M $Zn(CH_3COO)_2.2H_2O$, 12 mL ($Cu(NO_3)_2.3H_2O$) (0.225 M), and 10 mL PEG-200 in a beaker was stirred for 20 min at 70 ^{0}C. Then, the pH was adjusted to 10 by NaOH (20 wt%). The resulting suspension was put in the MW oven and irradiated for 20 min at 50% of the 1000-watt output power oven. Finally, the resultant precipitate was washed with DW and, then with ethanol. The residue was dried at 80 ^{0}C for 6h and then at 200 ^{0}C for 2h in the oven. The product was labeled as rGO-ZnO/CuO(P2). The schematic overview of the rGO-ZnO/CuO(P) synthesis was given in Figure 11.

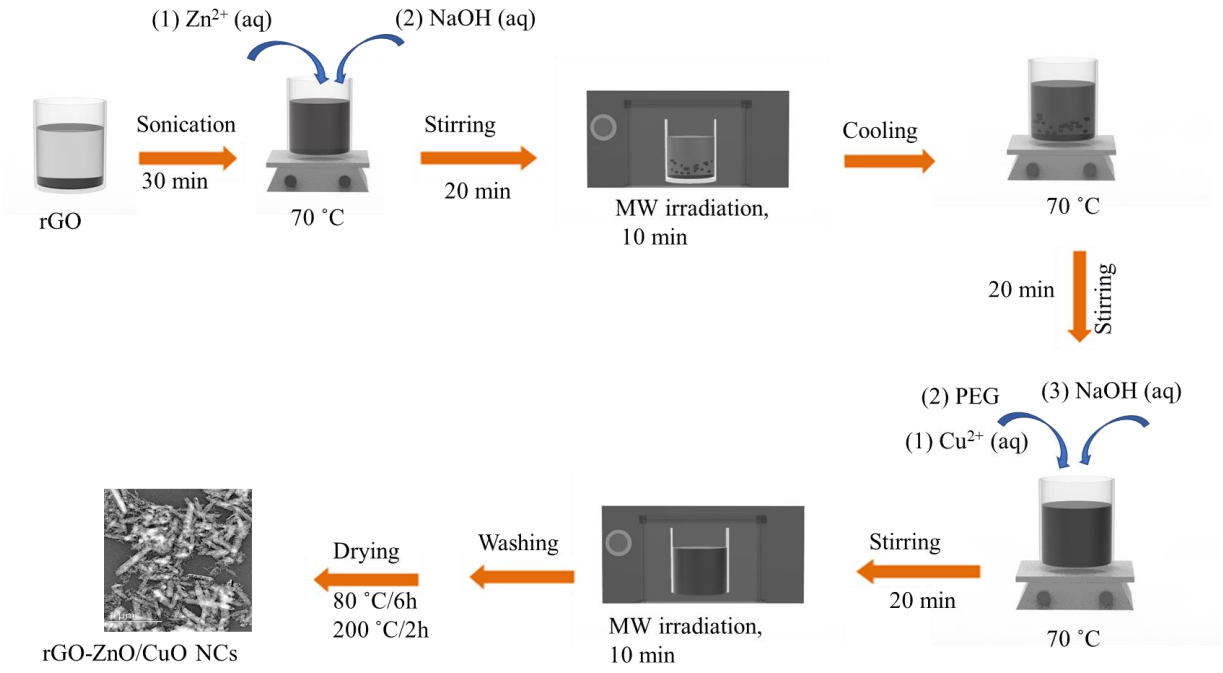

Figure 11. Schematic diagram of MW-assisted synthesis of rGO-ZnO/CuO using PEG (numbers (1), (2), and (3) indicate the sequence of addition).

3.5. Photocatalytic Studies

In this experiment, we used a 150-watt double-ended halogen lamp (Philips) immersed in the center of the borosilicate double-walled immersion well photoreactor. The reactor was surrounded by a circulating water jacket to cool the lamp. The photoreactor was suspended in the beaker containing MB aqueous solution and catalyst. The beaker was covered externally with aluminum foil to reflect the light to the reactant mixture and to prevent penetration of ambient light. The whole setup was kept in the cupboard. The photographic images of the components and the setup of the assembly were shown in Figure 12.

The photocatalytic efficiency of the samples (binary and ternary) was evaluated against MB degradation. The reaction suspension was prepared by mixing 120 mL MB (10 ppm) and 20 mg catalyst. To assure homogenous dispersion of the catalyst and dye molecules, a 30 minutes sonication was employed. Then, it was irradiated by visible light while being magnetically stirred continuously. Every 15 minutes, 4 mL sample was taken and centrifuged to separate the catalysts from the liquid before the absorbance measurement. After the photocatalytic degradation of MB, the absorbance of each sample was measured.

To investigate the main active species involved in photocatalytic degradation of MB using rGO-ZnO/CuO NCs, the trapping experiments were conducted. In the experiment, the scavengers used were ethylenediaminetetraacetic acid disodium (EDTA-2Na), isopropanol (IPA), and $AgNO_3$ to scavenge photogenerated holes (h^+), hydroxyl radicals ($^{\bullet}OH$), and superoxide radicals ($^{\bullet}O_2^-$), respectively. In the experiments, 1mmol of each scavenger were added to the 120 mL MB (10 ppm) and 20 mg catalyst mixture before sonication. Then, the above procedures for photocatalysis were repeated.

In this work, the performance was evaluated in terms of removal efficiency and reaction kinetics. The percentage of photocatalytic degradation (D%) was evaluated using Eqn. 18. The kinetics of the reaction was analyzed using pseudo-first and pseudo-second order equations (Eqn. 19 and 20). The rate constant of the photocatalysis was determined using the best fitting equation from the plots of $\ln(C_t/C_0)$ vs t (Eqn. 19, for pseudo first order) and $(1/C_t)$ vs t (Eqn. 20, for pseudo-second order) reactions (F. Liu et al., 2019).

$$D(\%) = \frac{C_0 - C_t}{C_0} \times 100 \qquad (18)$$

$$\ln\left(\frac{C_t}{C_o}\right) = -kt \qquad (19)$$

$$\frac{1}{C_t} = \frac{1}{C_o} + kt \qquad (20)$$

where k represents the rate constant, C_0, and C_t are the dye (pollutant) concentrations before (or at time=0 min) and after illumination (or at time=t min), respectively.

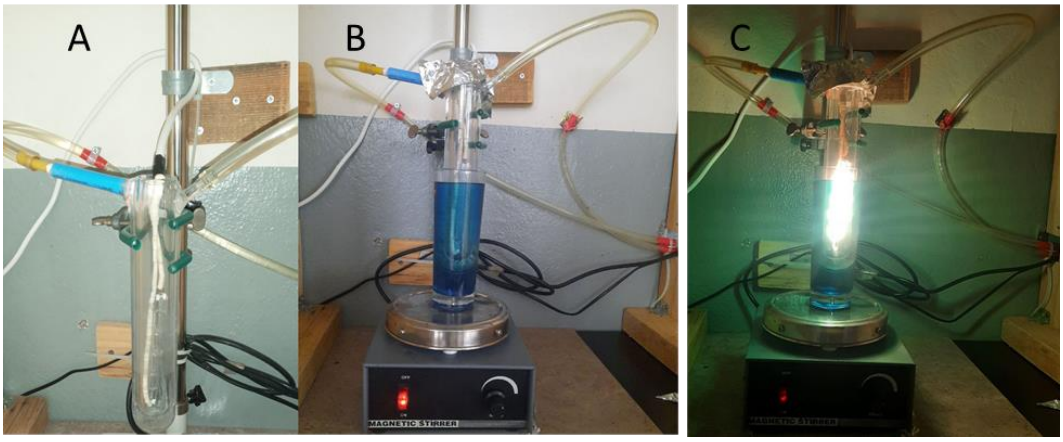

Figure 12. Photographic images of photocatalysis setup (A) empty reactor, (B) reactor with sample, and (C) reactor with sample and during light irradiation.

3.6. Catalytic Reduction Studies

Separate procedures were used for the catalytic reduction of 4-NP. These are: (i) reduction using the pristine metal oxides (CuO and ZnO) synthesized using CAL and VSB extracts (in sections 3.3.1), (ii) catalytic reduction using nanocomposites prepared using CAL, VSB, and PEG (in sections 3.3.2 and 3.3.4).

(i) To evaluate the catalytic performance of the metal oxide NPs, a 4-NP reduction reaction was conducted. Typically, 20 mg $NaBH_4$ and 100 mL 4-NP (20 ppm) aqueous solutions were transferred to a conical flask. After 2 min shaking, 5 mg of catalyst was added to the $NaBH_4$ and 4-NP mixture. The progress of the 4-NP reduction was monitored by a UV-vis

spectrophotometer (SM-1600) at a wavelength of around 405 nm at room temperature. From the resulting mixture, 3 mL was taken out every 3 min and transferred to the cuvette for the absorbance measurement. The kinetic analysis was conducted using a pseudo-first-order equation (Eqn. 19) and pseudo-second order (Eqn. 20), where C_o and C_t correspond to the concentration of 4-NP at times 0 and t, respectively.

(ii) To evaluate the catalytic performance of the nanocomposites prepared using CAL, VSB, and PEG, 4-NP was used as a model pollutant along with $NaBH_4$ as a reductant. Typically, 40 mg catalyst sample and 40 mg $NaBH_4$ were mixed with 100 mL of 20 ppm 4-NP in a 250 mL beaker. The progress of the reaction was followed by measuring changes in absorbance of 4-NP at λ_{max}=400 nm using a UV-vis spectrophotometer (Zelekew & Kuo, 2017). Every 3 min, a 3 mL sample of the mixture was withdrawn and its absorbance spectrum was then measured. And finally, Eqn. 19 and Eqn. 20 were used to analyze the rate of reduction.

3.7. Catalyst Recovery and Reusability

Stability is one of the important factors to consider when it comes to the reusability of the catalyst. To this end, the recyclability of the catalysts was evaluated against the photocatalytic degradation of MB and catalytic reduction of 4-NP on repeated use for up to four successive runs. Catalyst recovery was performed at the end of each cycle, by centrifuging the reactant mixture at 3000 rpm for 15 min to separate catalyst particles from the supernatant effluent, and then washed using DW and ethanol three times each. Finally, the residue was dried at 60 ºC overnight and then reused in the next run (Mathalai Sundaram et al., 2019).

3.8. Antibacterial Activities Study

The antibacterial properties of the synthesized nanoparticles were evaluated by the agar disk-diffusion technique according to the standard procedures developed by the Clinical and Laboratory Standards Institute (Balouiri et al., 2016; Chemingui et al., 2019). The *In vitro* antibacterial activities of the CuO(L-10), ZnO(B), CuO-ZnO(B)-20%, ZnO(P) CuO-ZnO(P), and rGO-ZnO/CuO(P) were evaluated against clinically important human pathogens, namely, *Escherichia coli* (*E. coli*, American type cell culture or ATCC 25922), *Staphylococcus aureus* (*S. aureus*, ATCC 25923), *Pseudomonas aeruginosa* (*P. aeruginosa*, ATCC 27853), and

Streptococcus pyogenes (*S. pyogenes* ATCC19615) collected from Ethiopian Public Health Institute (EPHI).

The medium was prepared from molten nutrients and Mueller–Hinton agar. Ceftriaxone and dimethyl sulfoxide (DMSO) were used as positive and negative controls, respectively. The different concentrations of the nanomaterials were prepared using DMSO as a solvent. Accordingly, 100 mg catalyst was dispersed in 50 mL DMSO yielding stock solution of (2 mg/ml) concentration. Four different concentrations of 37.5, 75, 150, and 300 µg/mL were prepared by diluting using DMSO as a solvent. The antibacterial activity studies were conducted in collaboration with microbiologists.

First, agar plates were inoculated with a standardized inoculum of the test microorganism (*E.coli, S. aureus, P. aeruginosa,* and *S. pyogenes*). The bacteria were cultured in the Muller-Hinton broth at 37°C for 24 h in a bacteriological incubator. Then the filter paper discs (about 6 mm in diameter) were soaked in 1 mL solution of each test concentration. Then after, the soaked filter paper discs containing the test nanoparticle at the desired concentration were placed on the agar surface. The plates were incubated under suitable conditions (37 °C for 36 h) (Balouiri et al., 2016). Finally, the diameters of inhibition growth zones due to the diffusion of the antimicrobial agent into the agar were measured. The overview of procedures of the antibacterial activity was given in Figure 13.

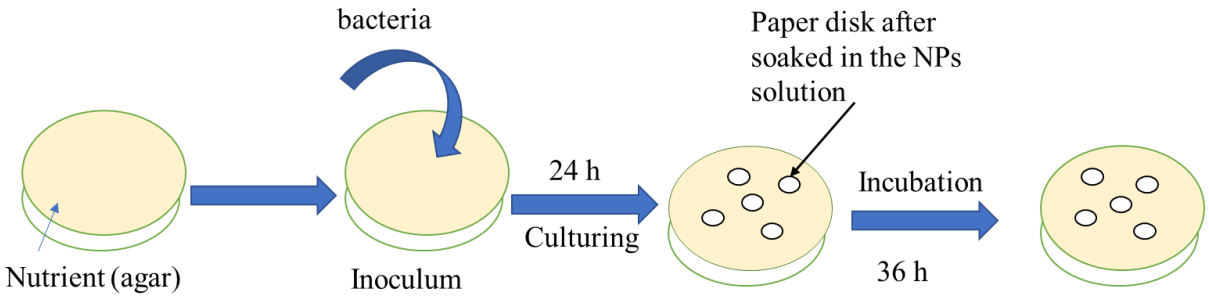

Figure 13. Schematic overview of the major steps for the antibacterial activities.

3.9. Characterization Techniques

3.9.1. X-ray Diffraction

The crystal structure and phase of the obtained nanomaterial samples were probed by an X-ray diffraction (XRD) instrument (Shimadzu, XRD-7000S) with Cu Kα radiation (λ=1.5406 Å) sources. The XRD patterns of the samples were scanned in the 2θ ranging from 10 to 80 degrees at scan rates of 3 or 4 degrees per minute. The samples were used in powder form (100-150 mg). The crystallites size of the sample was calculated using the Scherrer equation (Eqn. 21):

$$D = \frac{k\lambda}{\beta cos\theta} \qquad (21)$$

where: D = crystallite size, λ = the wavelength of the X-ray source applied, β = full width at half maxima (FWHM), θ = the Bragg angle, and *k* = the shape constant ≈ 0.9.

3.9.2. UV-Vis Spectroscopy

UV-Visible absorbance spectra of the nanomaterials were measured using a UV-Vis spectrophotometer (JASCO V-670). The samples were prepared by mixing 3 mg of each sample with 20 mL of ethanol to prepare 0.15 g/mL suspension under sonication for 15 min. The samples characterized are (i) CuO(L-10); (ii) ZnO(B), CuO-ZnO(B)-20%; (iii) CuO(P), ZnO(P), CuO-ZnO(P), rGO-ZnO/CuO(P)and rGO-ZnO/CuO(P2). The progress of all photocatalytic degradation of MB and catalytic reduction of 4-NP were measured by a double-beam UV-Vis spectrophotometer (Azzota: SM-1600).

Using the absorbance spectrum, the bandgap of samples was calculated by applying Tauc's formula (Eqn. 22)

$$(\alpha h\nu)^n = C\left(h\nu - E_g\right) \qquad (22)$$

where α, h, v, E_g, n, and, C were the absorption coefficient, Planck's constant, light frequency, bandgap energy, the power factor of the transition mode (2 for direct, 0.5 for indirect), and constant related to the material, respectively.

3.9.3. Fourier Transform-Infrared Spectroscopy

To identify the functional groups of the synthesized materials or that of the attached groups, FTIR spectra of the samples were recorded using Spectrum 65 FT-IR (PerkinElmer) in the range 4000-400 cm^{-1}. The samples for measurement were prepared by mixing the powder of the samples with KBr forming a homogenous paste and then the resulting paste was molded into pellets.

3.9.4. Photoluminescence

The emission spectra were measured by a fluorescence spectrophotometer (Agilent Cary Eclipse Fluorescence Spectrophotometer). The suspension was prepared by dissolving 3 mg synthesized samples in 15 mL methanol and sonicated for 15 minutes for homogeneous dispersion. From the resulting suspension, 3 mL was put in the quartz cuvette and then emission spectra were recorded at different excitation wavelengths.

3.9.5. Scanning Electron Microscopy with Energy-Dispersive X-ray Spectroscopy

The surface morphologies and elemental composition of the prepared samples were characterized using different types of energy-dispersive spectroscopy hyphenated with scanning electron microscopes (SEM-EDS).

(i). CuO sample synthesized using CAL (i.e. CuO(L-10)) was characterized by scanning electron microscope (SEM, COXEM-30). The fine powder form of the sample was placed on the carbon tape and then the SEM images and EDS spectrum were recorded.

(ii) The surface morphology, EDS elemental mapping, and EDS spectra of other samples ZnO(B), CuO(B), CuO-ZnO(B)-20%, ZnO(P), CuO-ZnO(P), rGO-ZnO/CuO(P), and rGO-ZnO/CuO(P2) were measured by scanning electron microscope (JOEL, JCM-6000Plus) and field emission scanning electron microscope (HITACHI, S-4800). The samples for SEM image measurement were prepared by dispersing the powder in DW (2 mg sample powder in 20 mL DW) and sonicating for 15 min. A few drops of the resulting suspension were placed on the glass slide and allowed to air dry. Then the slides were used for the SEM and EDS measurements.

3.9.6. Transmission Electron Microscopy (HRTEM) with Energy-Dispersive X-ray Spectroscopy

The surface morphology and elemental mapping were measured by Transmission electron microscopy (TEM) FEI (Tecnai G2 F30). TEM analysis was employed for CuO-ZnO(B)-20%, rGO-ZnO/CuO(P), rGO, and GO samples. Samples for TEM analysis were prepared by applying the suspension of the sample on a copper grid and then allowed to dry.

3.9.7. X-Ray Photoelectron Spectroscopy

The elemental composition on the surface was collected using X-Ray Photoelectron Spectroscopy (XPS, Thermo Scientific, Al Kα (hν = 1350 eV)). XPS analysis was conducted for CuO-ZnO(B)-20% nanocomposite. The powder of each sample was mixed with DW (2 mg powder in 20 mL DW) and sonicated for 15 min. A few drops of the resulting suspension were placed on the glass slide and air-dried. Then the slide was used for the XPS measurements.

3.9.8. Surface Area Analysis

To identify the surface area and pore size distribution, standard BET (Brunauer-Emmett-Teller) surface area analysis and BJH (Barrett-Joyner-Halenda) pore size and volume analysis with N2 adsorption-desorption isotherms at 77 K were employed using Micromeritics ASAP 2420 (V2.09 J) instrument. ZnO(B), CuO(B), and CuO-ZnO(B)-20% samples were analyzed using this technique.

3.9.9. Electrochemical Studies

The electrochemical measurements were conducted using the Ivium Technologies system with an IviumSoft and used a standard three-electrode cell with Ag/AgCl reference electrode (saturated), platinum wire counter electrode, and FTO coated with the catalyst sample as working electrode. 0.1 M Na_2SO_4 was used as an electrolyte. Mott-Schottky analyses were conducted over the range of -1.0 V to 1.5 V at a frequency of 1000 Hz. Similarly, electrochemical impedance spectroscopy (EIS) was carried out by applying a sine wave with an amplitude of 5 mV over the frequency region ranging from 100 kHz to 0.01 Hz.

CHAPTER FOUR

4. RESULTS AND DISCUSSION

4.1. Identification of the best Performing MO-based Nanomaterials Obtained using CAL and VSB for Further Analysis and Characterization.

Nanomaterials of CuO, ZnO, and CuO-ZnO were synthesized using extracts from *Cordia africana* Lam and *Verbascum sinaiticum* Benth. The synthesized materials were evaluated against 4-NP reduction and MB photocatalytic degradation. Based on the rate of reaction and efficiency, the nanomaterials with the best performance were identified. The identified materials were characterized for further analysis. Accordingly, the performance of single oxides (CuO and ZnO NPs) was tested for the reduction of 4-NP. On the other hand, the performance of CuO-ZnO NCs was tested against photocatalytic degradation of MB. The details of the analysis were discussed in sections 4.1A and B.

A. Mono-component oxides: ZnO and CuO NPs

To identify the optimum quantity of the extracts to produce the best-performing nanomaterials following the stated protocols, the CuO and ZnO NPs samples were obtained using CAL and VSB extracts of different volumes, i.e. CuO(L-10, 30, 50); ZnO(L-10, 30, 50), CuO(B-10, 30,50), and ZnO(B-10, 30, 50). In this regard, preliminary performance evaluation was employed and the material that has the highest performance against the catalytic reduction of 4-NP in the presence of $NaBH_4$ was identified. The reaction rate constants of the synthesized materials using both CAL and VSB were compared as shown in Figure 14A. According to the result, CuO synthesized using 10 mL or CuO(L-10) showed the highest rate of reduction against the 4-NP. Similarly, other CuO NPs obtained using CAL (30 mL and 50 mL) and VSB (10, 30 and 50 mL) also showed a relatively good performance with reduction rate lower than that of CuO obtained using 10 mL CAL. Whereas all ZnO samples obtained using both extracts showed negligible performance. Thus, we proceed with CuO(L-10) for further characterization and analysis of the effects of other parameters on the performance. The analysis was carried out

using 5 mg catalyst, 20 mg $NaBH_4$, and 100 mL of 20 ppm 4-NP. The rates of reduction reaction of the tested samples were given in Table 4.

B. Binary component: CuO-ZnO NCs

Similar to that of the mono-component oxides, CuO-ZnO NCs were synthesized using *Cordia africana* Lam and *Verbascum sinaiticum* Benth extracts. To identify the optimum wt% of CuO in the CuO-ZnO NCs for photocatalytic applications, CuO-ZnO NCs samples were synthesized using CAL and VSB extracts. Hence, different wt% of CuO samples with CAL, i.e CuO-ZnO(L)-X%~~-X~~ (X=10, 20, 30, 50) and VSB, i.e., CuO-ZnO(B)-X% (X=10, 20, 30, 50) were synthesized. To identify the best-performing nanocomposite, the synthesized materials were tested against MB photocatalytic degradation. In this regard, photocatalytic degradation of MB was performed using 20 mg catalyst and 120 mL of a 10 ppm MB aqueous solution. The rate constant of degradation was displayed in Figure 14B. According to the result, all CuO-ZnO samples obtained using both CAL and VSB extracts showed photocatalytic activities. Among the CuO-ZnO samples, the one with 20 wt% CuO content synthesized using VSB (CuO-ZnO(B)-20%) showed the highest performance. Therefore, CuO-ZnO(B)-20% was used in the subsequent characterization and performance analysis. The detailed rates of photocatalytic reaction were given in Table 5.

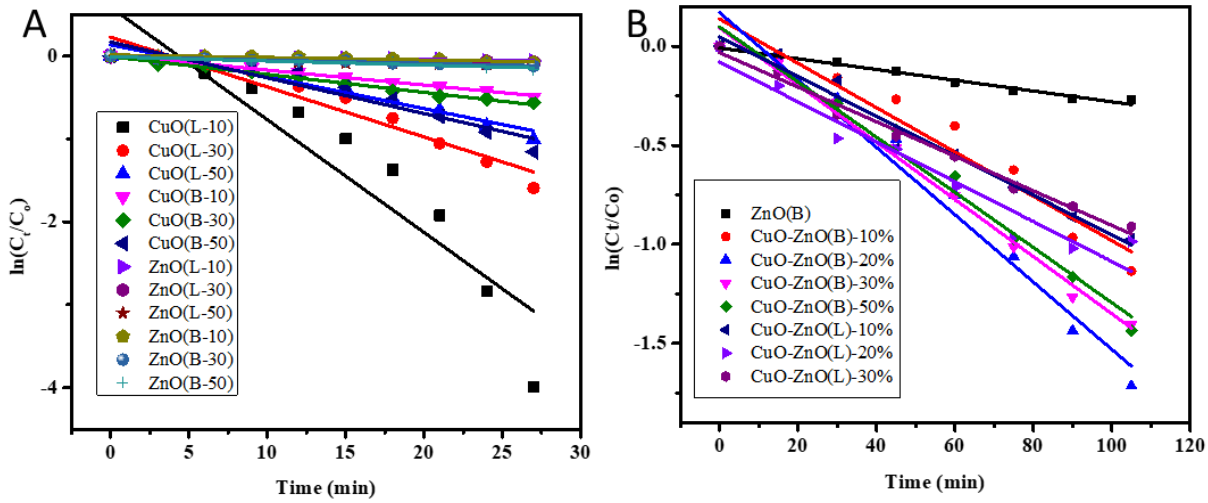

Figure 14. Plot of $\ln(C_t/C_0)$ *vs* t (min)) for catalysts obtained using CAL and VSB: (A) for 4-NP reduction kinetics using CuO and ZnO catalysts, (B) for photocatalytic degradation kinetics using CuO-ZnO catalysts.

Table 4. Rate of 4-NP reduction by CuO and ZnO NPs obtained using VSB extracts.

Extract	**Catalyst**	**Rate constant, min^{-1}**
CAL	CuO(L-10)	0.13577
	CuO(L-30)	0.06017
	CuO(L-50)	0.03842
VSB	CuO(B-10)	0.01808
	CuO(B-30)	0.02155
	CuO(B-50)	0.043
CAL	ZnO(L-10)	0.00211
	ZnO(L-30)	0.00259
	ZnO(L-50)	0.00456
VSB	ZnO(B-10)	0.00296
	ZnO(B-30)	0.00407
	ZnO(B-50)	0.00498

Table 5. Rate of photocatalytic degradation of MB using CuO-ZnO NCs obtained using CAL and VSB extracts.

Extract	Photocatalyst	Rate constant, min-1
VSB	ZnO(B)	0.00272
	CuO-ZnO(B)-10%	0.01118
	CuO-ZnO(B)-20%	0.017
	CuO-ZnO(B)-30%	0.01443
	CuO-ZnO(B)-50%	0.01392
CAL	CuO-ZnO(L)-10%	0.00998
	CuO-ZnO(L)-20%	0.01007
	CuO-ZnO(L)-30%	0.00872

4.2. Characterization of the Synthesized Nanomaterials

4.2.1. XRD Analysis

To investigate the crystallinity and phases of the synthesized materials, the XRD technique was employed. The XRD pattern of the CuO(L-10) samples obtained using CAL extract was displayed in Figure 15. The noticeable peaks positioned at 2θ values of 32.44, 35.46, 38.68, 48.7, 53.50, 58.0, 61.49, 66.14, and 74.89 degrees correspond to (110), (002), (111), (20-2), (020), (202), (11-3), (31-1), and (004) crystal planes, respectively. These values agree with the monoclinic CuO phase (Card number # 00-048-1548). The absence of peaks matching $Cu(OH)_2$ and Cu_2O in the pattern with the appearance of all peaks corresponding to the monoclinic CuO phase signifies the formation of pristine crystalline CuO by the MW-assisted synthesis method. The average crystallite size of the CuO NPs calculated for the highest peaks at 35.46° and 38.68° was around 9 nm. The resolved sharp peaks with a crystallite size of about 9 nm suggest the formation of the nanocrystalline CuO (Ahamed et al., 2014).

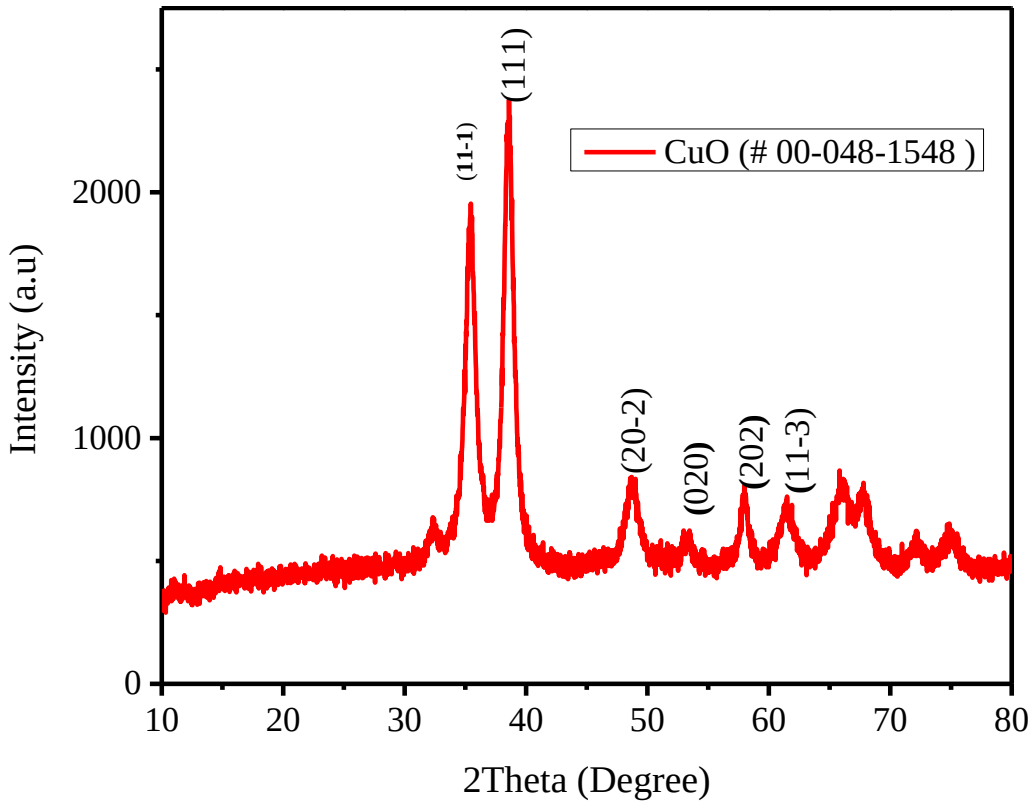

Figure 15. XRD patterns of CuO(L-10).

Furthermore, the XRD patterns of calcined samples: CuO(B), ZnO(B), and CuO-ZnO(B)-20% were displayed in Figure 16. As displayed in the Figure, the XRD pattern of the ZnO(B) sample at 2θ values of (31.79, 34.45, 36.26, 47.58, 56.6, 62.88, 66.4, 67.98, and 69.11), are indexed as (100), (002), (101), (102), (110), (103), (200), (112), and (201), respectively, corresponding to the hexagonal ZnO phase (card no. 00-036-1451). Similarly, the diffraction peaks of the CuO(B) sample obtained at 2θ values of (32.48, 35.62, 38.78, 48.94, 53.5, 58.29, 61.7, 65.9, 66.4, 68.08, and 72.46) indexed as (110), (11-1), (111), (20-2), (020), (202), (11-3), (022), (31-1), (220), and (311) planes, respectively, were assigned to the monoclinic CuO phase (card no. 00-048-1548). Moreover, the diffraction peaks of CuO-ZnO(B)-20% were observed at 2θ values of (31.76, 34.4, 36.28, 47.58, 56.62, 62.84, 66.36, 67.98, and 69.14) matched with the ZnO phase and those at 2θ values of (35.54, 38.72, 48.74, 53.42, 58.33, 61.6) matched with the CuO phase, confirming the formation of CuO-ZnO NCs. The diffraction patterns of the composite do not contain peaks other than CuO and ZnO, indicating the prepared sample is free of impurities (Taufique et al., 2018). The average crystallites were determined using Scherrer's formula (Eqn.

21) for the first three intense peaks (100), (002), and (101) for ZnO; (11-1), (111), and (20-2) for CuO; and (100), (002), and (101) for the CuO-ZnO NCs, respectively (Witoon et al., 2013). The calculated average crystallites sizes were 22 nm, 14 nm, and 18 nm for ZnO(B), CuO(B), and CuO-ZnO(B)-20% samples, respectively. The values obtained indicated that the synthesized samples have crystallites in the nano-size range. Because of the possibility that photocatalysts could be improved by reducing the crystallites size, the nano-size range crystallites of the synthesized CuO-ZnO(B)-20% samples make the materials an attractive photocatalyst candidate (Kirankumar & Sumathi, 2020).

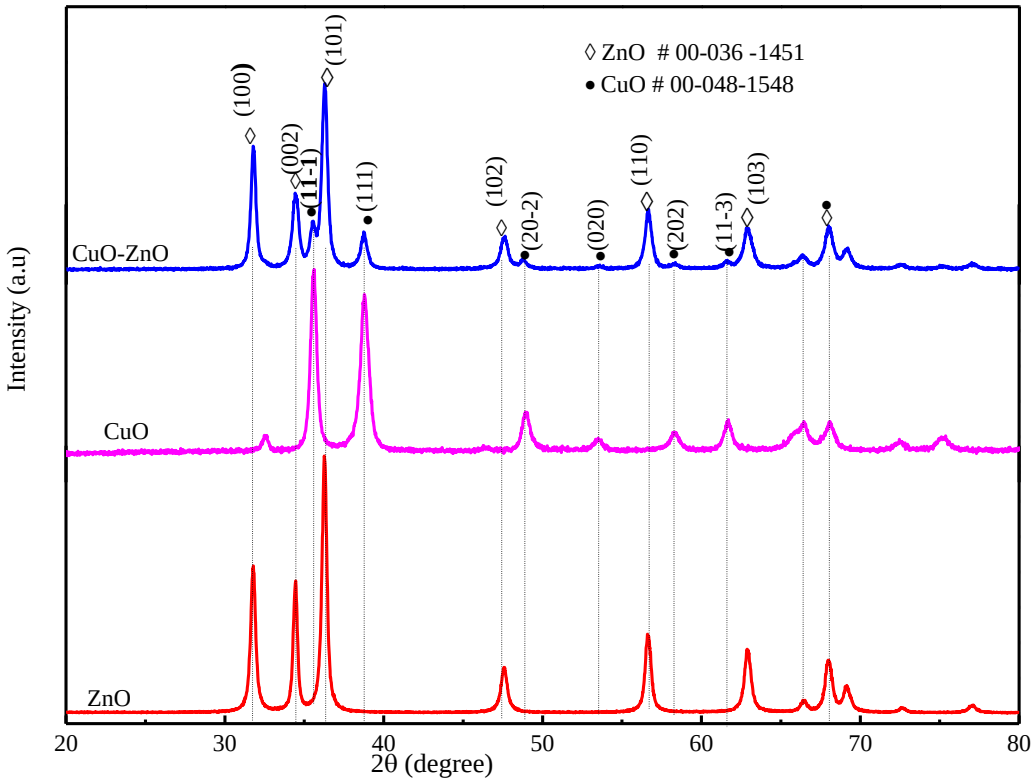

Figure 16. XRD patterns of ZnO(B), CuO(B), and CuO-ZnO(B)-20% samples.

Similarly, Figure 17 shows the characteristic XRD peak of graphite (Gr), graphene oxide (GO), and reduced graphene oxide (rGO) displayed at 2θ of 26.4º, 9.9º, and 24.4º with the corresponding interlayer distance of about 0.3368 nm, 0.8906 nm, and 0.3640 nm, respectively. The relatively wider interlayer distance of GO could be attributed to the presence of carboxyl, hydroxyl, and epoxide groups introduced by the oxidation of the graphite (Alam et al., 2017; Kalantari Bolaghi et al., 2019; Thakur & Karak, 2012). Whereas the reduction of GO to rGO

resulted in a decreased interlayer distance to about 0.3640 nm which is closer to that of the bulk graphite suggesting the reduction of the hydroxyl, carboxyl, and epoxide functional groups. This value is consistent with the previously reported value (Thakur & Karak, 2012). The disappearance of the peak at 2θ of 9.9º and the appearance of a new peak at 2θ of 24.4º for rGO indicates the reduction of the oxygen-containing functional groups of GO. Besides, the closer spacing between rGO layers to that of graphite layers could be ascribed to the effective reduction and restacking of graphene layers due to the strong π-π interaction (Alam et al., 2017; Thakur & Karak, 2012). The strong and sharp peak at 2θ = 26.4º of pristine graphite with the corresponding spacing of 0.3368 is consistent with previous reports (M. Khan et al., 2015).

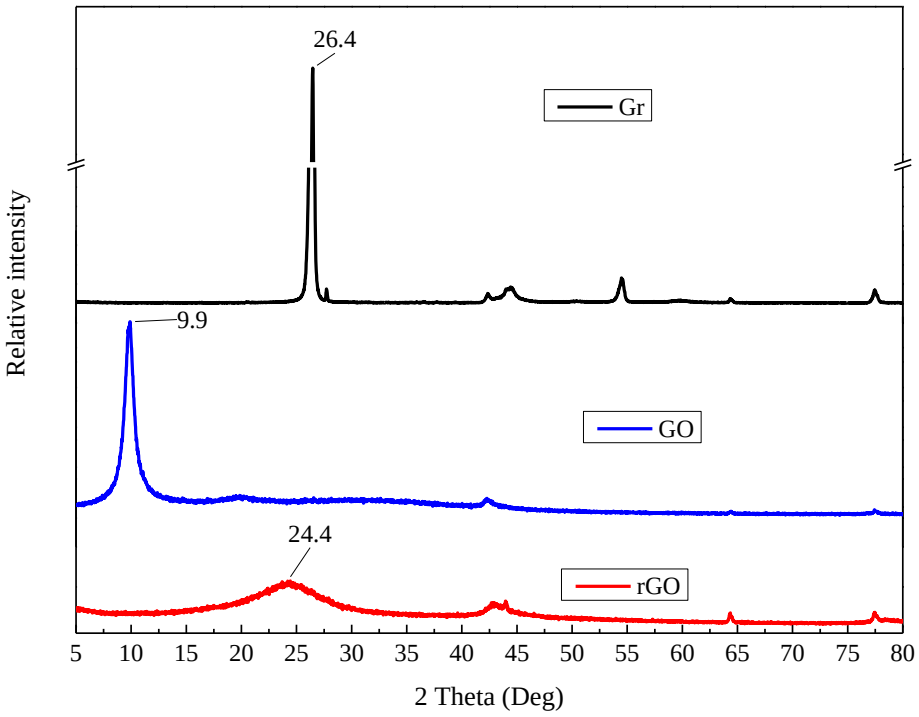

Figure 17. XRD patterns of graphite powder (Gr), graphene oxide (GO), and reduced graphene oxide (rGO) samples.

The XRD patterns of the samples synthesized using PEG: ZnO(P), CuO-ZnO(P), and rGO-ZnO/CuO(P) were displayed in Figure 18. The diffraction patterns of rGO-ZnO/CuO(P) appeared at 2θ of (31.76, 34.42, 36.26, 47.56, 56.62, 62.88, and 67.98) which could be assigned to the planes (100), (002), (101), (102), (110), (103), and (112) of hexagonal ZnO phases according to JCPDS card (36-1451), respectively. The diffraction patterns of rGO-

ZnO/CuO(P2) were almost similar to that of rGO-ZnO/CuO(P). Most of the diffraction peaks arising from CuO were weak and masked by strong peaks from the ZnO phase related to the relatively smaller CuO content. Hence, the weak diffraction peaks appeared at 2θ of (35.54, 38.90, 58.26, and 61.52) assigned to planes ((11-1), (200), (202), and (11-3)) belonging to the monoclinic CuO phases according to JCPDS card (36-1451), respectively. Distinct peaks related to the rGO were not seen in the pattern of rGO-ZnO/CuO which might be due to the low crystallinity and small amount of rGO producing low intensity (Kalantari Bolaghi et al., 2019; Omar et al., 2014).

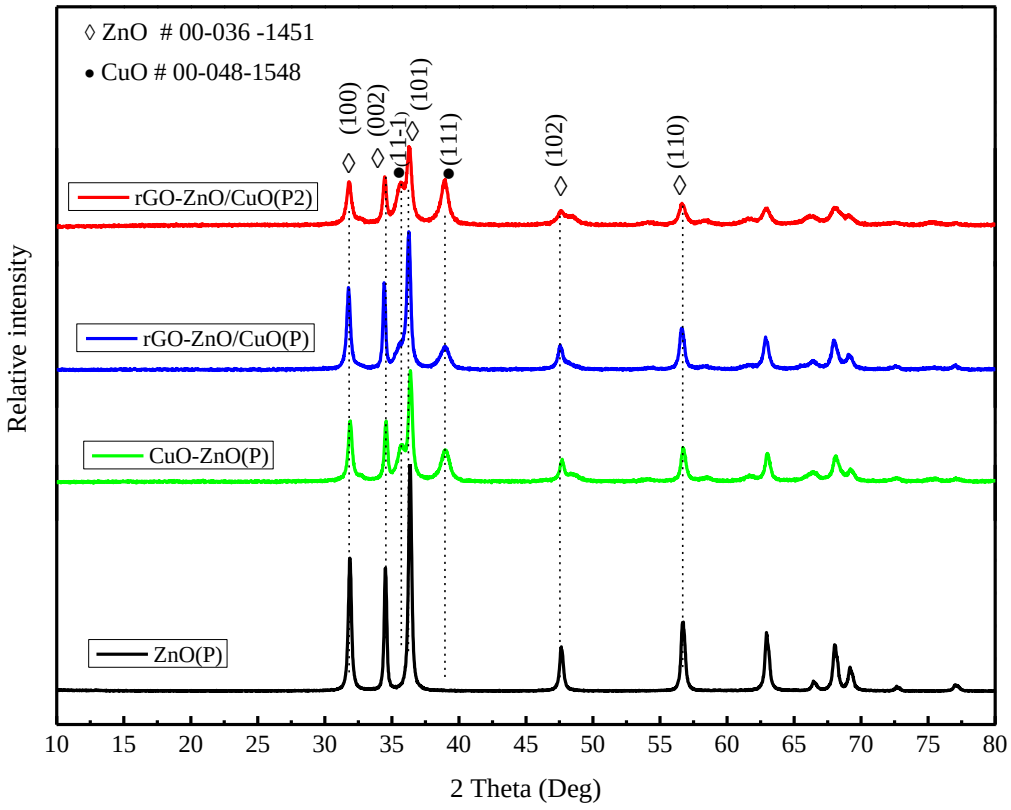

Figure 18. XRD patterns of ZnO(P), CuO-ZnO(P), rGO-ZnO/CuO(P) and rGO-ZnO/CuO(P2) samples

4.2.2. UV-Vis Spectroscopic Analysis

The UV-Vis spectra of nanomaterials can provide information about the size, band gap, and other interactions between the excited electrons and light. In this regard, the UV-Vis absorption spectra of CuO(L-10), ZnO(B), and CuO-ZnO(B)-20% were given in Figure 19A and C.

CuO(L-10) showed absorbance over a wide range of wavelength (UV and visible range) with absorbance maximum, λ_{max}=388 nm (Figure 19A). Similarly, both ZnO(B) and CuO-ZnO(B)-20% samples absorbed strongly in the UV region (λ_{max}=374 nm) which is consistent with previous works (Islam et al., 2019; L. Zhu et al., 2018). Portions of the absorption spectrum fall in the visible range with the tail reaching 800 nm, which could be attributed to the light scattering in the colloidal suspension (Islam et al., 2019). Comparatively, the CuO-ZnO(B)-20% sample showed a broader absorption spectrum over the range between 250 and 800 nm. In comparison to pristine ZnO NPs, the presence of CuO is responsible for a broader optical response in the visible region, indicating enhanced visible light absorption of CuO-ZnO(B)-20% (Sathishkumar et al., 2011). In addition, the bandgap of both CuO(L-10), ZnO(B), and CuO-ZnO(B)-20% samples were estimated using Tauc's formula (Eqn. 22)(Momeni, 2015; Saravanakkumar et al., 2018). The direct bandgap energy of the samples was obtained from the curves fitting of $(\alpha h\nu)^2$ vs $h\nu$ as depicted in Figure 19B and D (X. Lei et al., 2019) by extrapolating the slope of the linear region to the x-axis intersection (i.e., at $(\alpha h\nu)^2 = 0$). Accordingly, the results were approximately found to be 2.24 eV for CuO (L-10), 3.01 eV for ZnO(B) and 2.74 eV for CuO-ZnO(B)-20% (Figure 19B and D). The result revealed that the bandgap of the CuO-ZnO(B)-20% is lower than the ZnO(B) NPs. The low bandgap and improved efficiency of visible light-harvesting capacity makes CuO-ZnO(B)-20% suitable candidate for photocatalytic application (J. Yu et al., 2015).

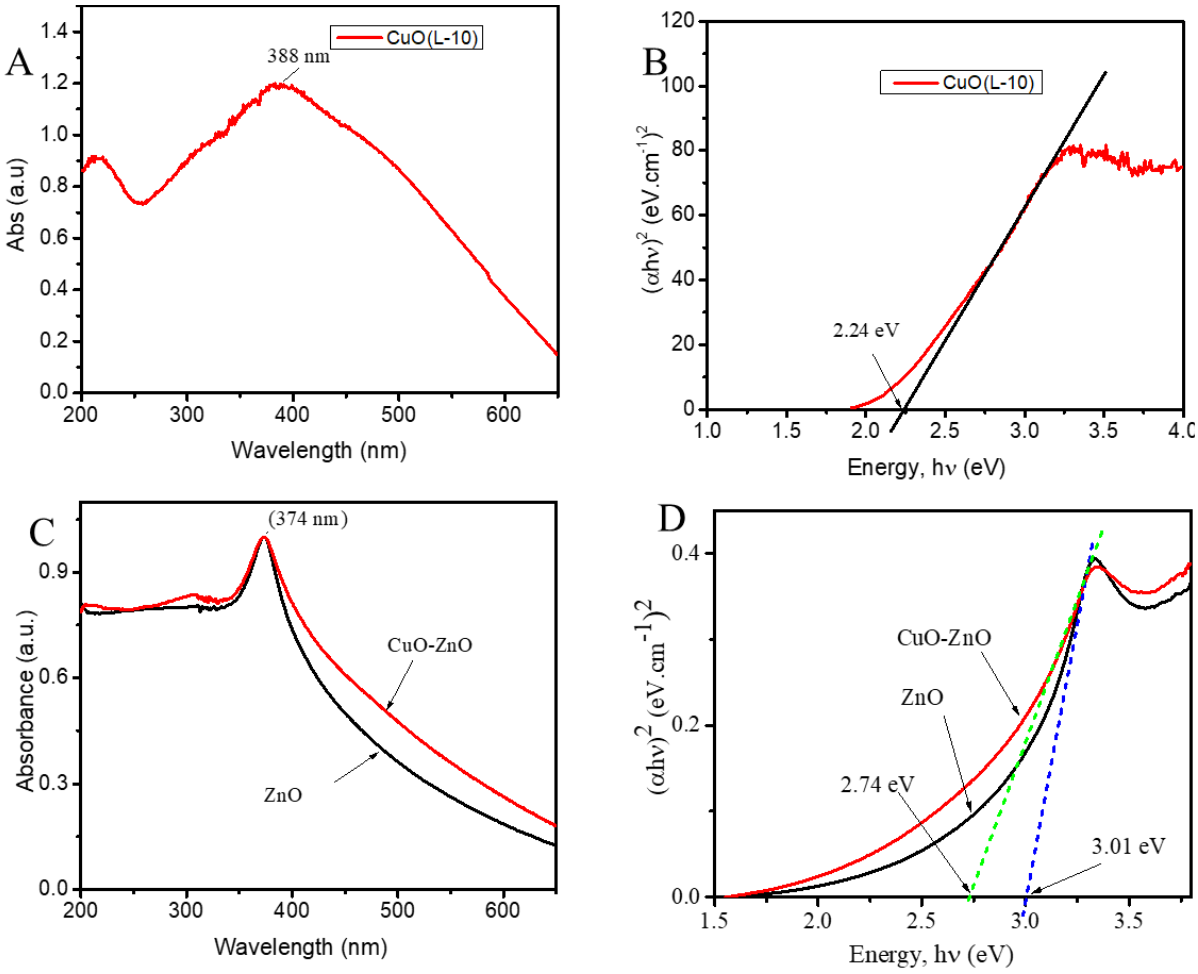

Figure 19. UV-Vis absorbance spectra: (A) CuO(L-10), (C) ZnO(B) and CuO-ZnO(B)-20%; Tauc's plot: (B) CuO(L-10), (D) ZnO(B) and CuO-ZnO(B)-20%.

Similarly, the UV-Vis absorbance spectra of the samples of GO and rGO synthesized were presented in Figure 20. The Figure shows the UV-Vis absorption spectrum of the synthesized GO and rGO suspension in ethanol and photographs of their powder as well as the corresponding aqueous suspensions. A strong absorption band at 235 nm and a weak shoulder at 303 nm were observed for GO. The intense band at 235 nm could be assigned to the π-π* transitions of aromatic C=C bonds, and the weaker shoulder around 303 nm could be due to the n-π* transitions of C=O bonds (Arias et al., 2020). Upon reduction of GO, the shoulder peak at 303 nm disappeared, and that at 235 nm was red-shifted to the broader peak at around 265 nm attributed to the aromatic C=C π→π* transition indicating the restoration of the aromatic structure electronic conjugation (Mahendran et al., 2020). The results for both GO and rGO are

in close agreement with the values reported elsewhere (Johra et al., 2014; Momeni et al., 2018). The tail of the rGO spectrum in the visible region is significantly higher than that of the GO indicating the recovery of the sp^2-electronic conjugation of the graphene (Rabchinskii et al., 2018). Therefore, the shift in the 235 nm peak to the 265 nm and the color change from brown to deep black suspension in water confirms the reduction of GO (Mahendran et al., 2020; Rabchinskii et al., 2018).

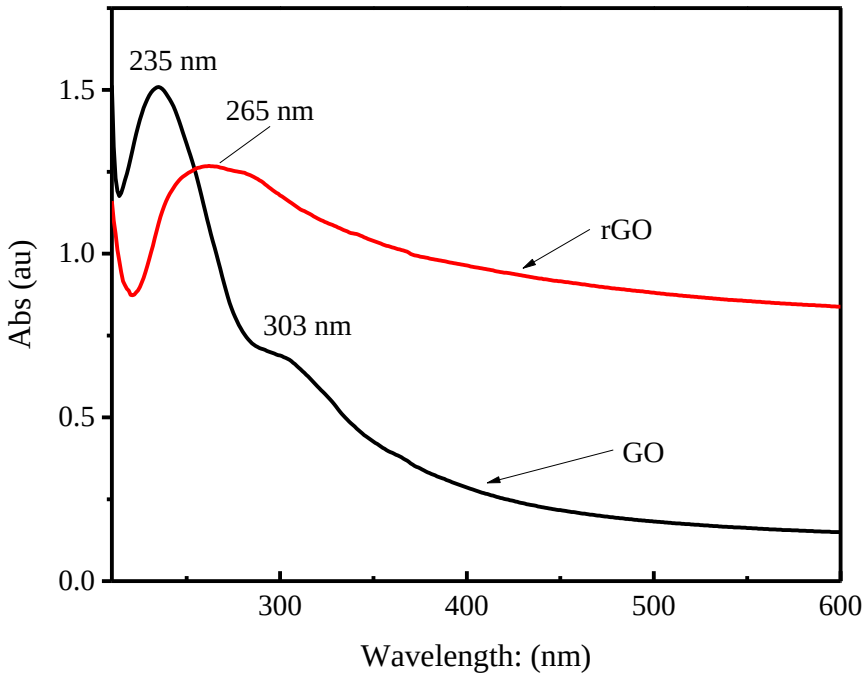

Figure 20. UV-Visible absorbance spectra of GO and rGO.

The UV-Vis absorption spectra and the corresponding Tauc's plots of ZnO(P), CuO-ZnO(P), rGO-ZnO/CuO(P), and rGO-ZnO/CuO(P2) samples were illustrated in Figure 21. All samples showed a strong absorption band in the UV region (λ_{max}≈367 nm) which is consistent with the absorbance of ZnO nanoparticles reported elsewhere (Figure 21A) (D. K. Singh et al., 2013). As can be seen from the Figure, CuO-ZnO(P), rGO-ZnO/CuO(P), and rGO-ZnO/CuO(P2) displayed a significant portion of their absorption spectra in the visible range compared to the ZnO sample, indicating the smaller energy bandgap compared to ZnO(P) (Islam et al., 2019). An estimated bandgap was obtained using Tauc's formula was 3.14 eV for ZnO(P), 2.91 eV for CuO-ZnO(P), 2.48 eV for rGO-ZnO/CuO(P), and 2.32 eV for rGO-ZnO/CuO(P2) (Figure 21B). Therefore, modifying ZnO NPs with CuO and rGO resulted in a low bandgap with an improved

visible light harvesting capacity of rGO-ZnO/CuO(P) which makes it a potential candidate for a visible light-based photocatalytic degradation of pollutant dyes (Sathishkumar et al., 2011; J. Yu et al., 2015).

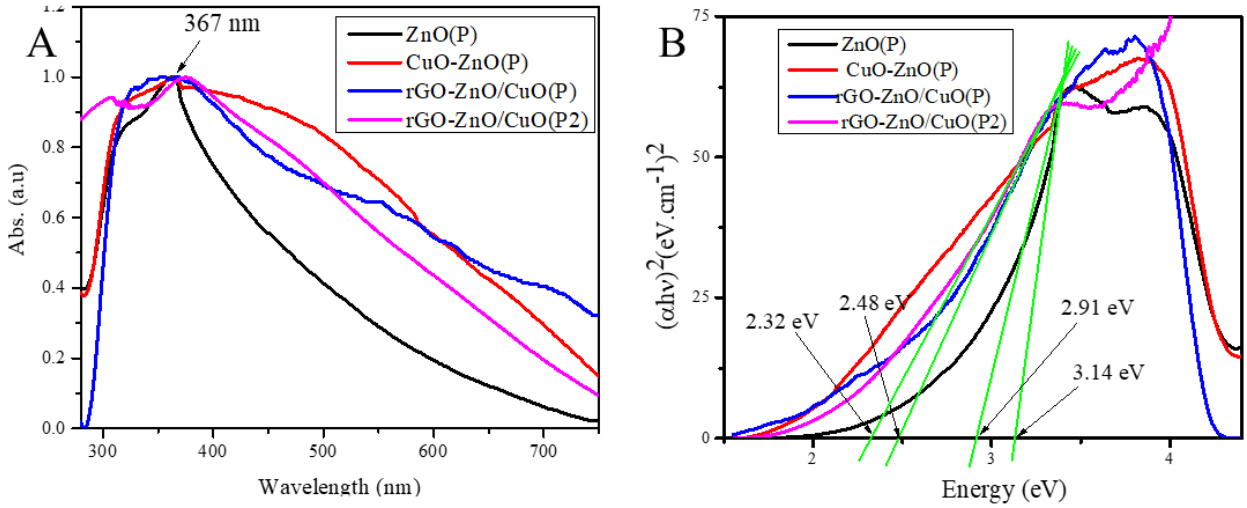

Figure 21. UV-Vis absorbance spectra and Tauc's plot of ZnO(P), CuO-ZnO(P), rGO-ZnO/CuO(P), and rGO-ZnO/CuO(P2).

4.2.3. FTIR Analysis

The FTIR spectral analysis of materials provides the functional groups of the materials. Particularly, in the case of metal oxide nanomaterials, the FTIR spectra can be used to identify the metal-oxygen bond and the type of molecules adsorbed to the nanomaterial surface. In addition, the analysis can be used to predict whether the reagents used in the synthesis are completely removed or not during the washing process. In this regard, the FTIR analysis of the synthesized materials using (i) extracts of CAL and VSB: CuO(L-10), ZnO(B), CuO-ZnO(B)-20%, CuO(B); (ii) GO and rGO; and (iii) PEG: ZnO(P), CuO-ZnO(P), rGO-ZnO/CuO(P), rGO-ZnO/CuO(P2).

The FTIR spectra of the aqueous extract of CAL and the CuO NPs synthesized using CAL extract were shown in Figure 22. Several characteristic bands were shown in the spectra of both the CAL extract and CuO NPs synthesized using the extract CuO(L-10). In both spectra (Figure 22), the bands at 3400, and 2920 cm^{-1} correspond to the O–H, and C-H functional groups stretching vibrational frequencies, respectively. Similarly, the bands at 1603 and 1300 to 1000

cm^{-1} (CAL extract) belong to the stretching vibrations of the C=C aromatic ring and C– OH (Nasrollahzadeh, Sajadi, & Maham, 2015). The sharp peaks that appeared at 1555 and 1393 cm^{-1} CuO(L-10) could be attributed to the carboxylate C-O stretching vibrations (asymmetric and symmetric). The bands arising due to the vibrational frequencies of the metal-oxygen (M–O) bond generally appear in the region below 1000 cm^{-1}. Hence, the peaks positioned at 497 and 591 cm^{-1} belong to characteristic vibrations of the Cu–O bond, revealing CuO NPs formation (Buazar et al., 2019). No infrared active modes from Cu_2O were detected indicating that under the conditions stated in the synthesis method, only the CuO phase was selectively produced. A comparison of the spectrum of the extract with that of CuO(L-10) shows that the molecules of the extract are found adsorbed on the surface of the CuO NPs. Furthermore, the FTIR results indicated the formation of the CuO phase supporting the XRD result.

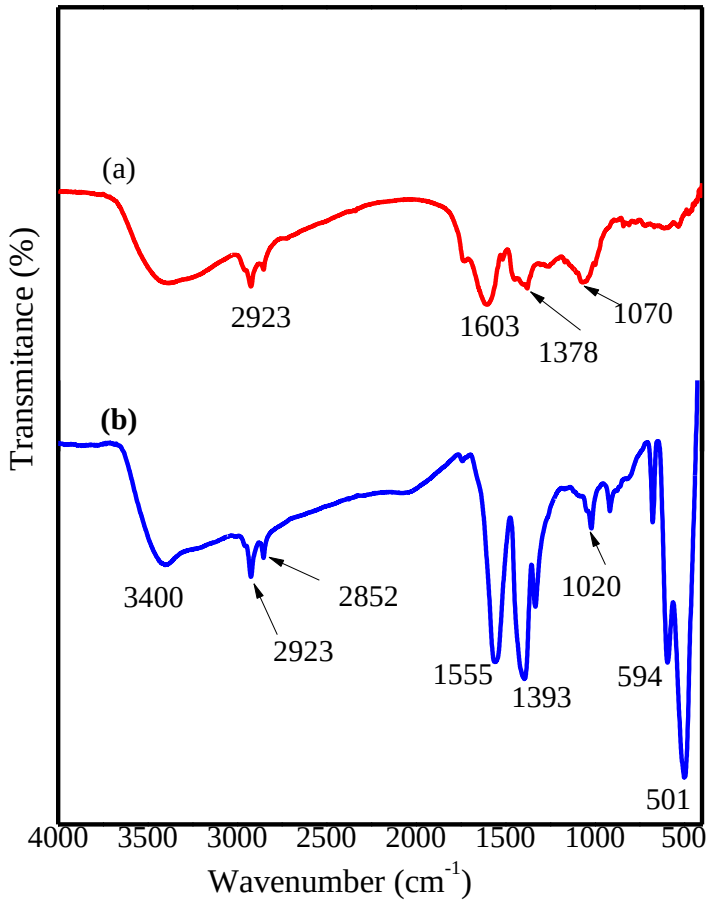

Figure 22. FTIR spectra of (a) CAL extract and (b) CuO(L-10).

In the case of materials synthesized using VSB extract (CuO(B), ZnO(B), CuO-ZnO(B)-20%), the FTIR was given in Figure 23. Since the M-O stretching vibrations of metal oxides usually appear in the ranges between 400 and 600 cm^{-1} of the FTIR spectrum, the characteristic intense peaks observed in the range 400-510 cm^{-1} belong to the Cu–O and Zn–O vibrations of CuO(B) and ZnO(B) samples respectively (Harish et al., 2017). The CuO(B) sample displayed a band at 435 cm^{-1} (Figure 23) corresponding to the Cu-O stretching band, whereas the ZnO sample showed a stronger intense peak at around 415 cm^{-1} and a weak band at 475 cm^{-1} (Figure 23) corresponding to Zn-O stretching. Also, the CuO-ZnO(B)-20% sample showed a much more intense peak at around 415 cm^{-1}, similar to the Zn-O vibration band of the ZnO sample. The peak from Cu-O vibration was not visible due to the low CuO composition of the CuO-ZnO (Govindasamy et al., 2021). Comparatively, peaks from adsorbed moisture or CO_2 are very weak.

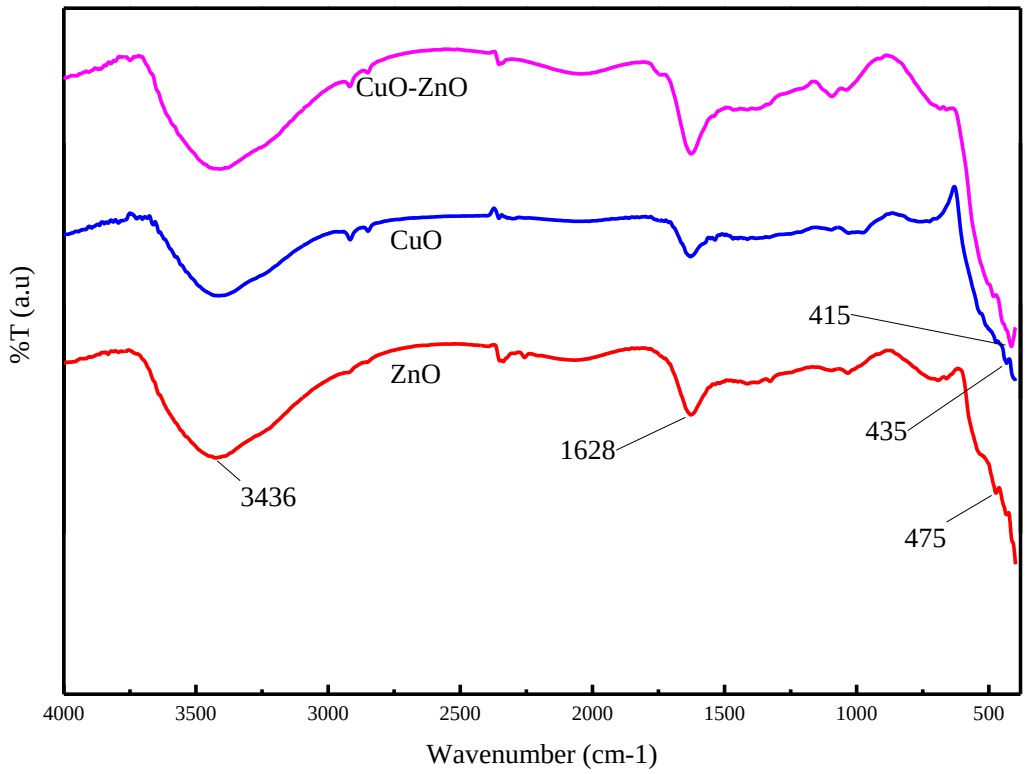

Figure 23. FTIR spectra of ZnO(B), CuO(B), and CuO-ZnO(B)-20% nanomaterials obtained using VSB.

Similarly, the FTIR spectra of GO and rGO samples were given in Figure 24. The FTIR spectrum of GO displayed characteristic peaks at about 3400, 1732, and 1622 cm^{-1} corresponding to the stretching vibrations of O-H, C=O, and C=C functional groups, respectively (Alam et al., 2017). The broad band that appeared around 3400 cm^{-1} is attributed to the overlapping bands from the O-H stretching vibration of alcohol, carboxylic acid, and adsorbed water molecules (Rabchinskii et al., 2018). In addition, the band at 1048 cm^{-1} can be assigned to the bending vibrations of the hydroxyl functional groups. In the case of rGO, distinctive vibration modes were observed at 3429, 2922, 2852, and 1636 cm^{-1} belonging to stretching vibrations of O-H stretching mode arising from the adsorbed water molecules or alcohol functional groups, asymmetric stretching modes of the $–CH_2$ group, symmetric stretching modes of the $–CH_2$ group, and aromatic C-C stretching, respectively (Alam et al., 2017; Emiru & Ayele, 2017; Majumdar et al., 2017). The FTIR spectra of both GO and rGO obtained are consistent with the literature reports (Emiru & Ayele, 2017). The C-H stretching bands for GO are weak relative to that for rGO indicating that there are more dangling C-H

functional groups in rGO than in GO as expected. Thus, the much lower intensity of the C=O bands in the rGO and the stronger peaks of the C-H stretching bands indicate the reduction of the oxygen-containing functional groups of GO (Alam et al., 2017).

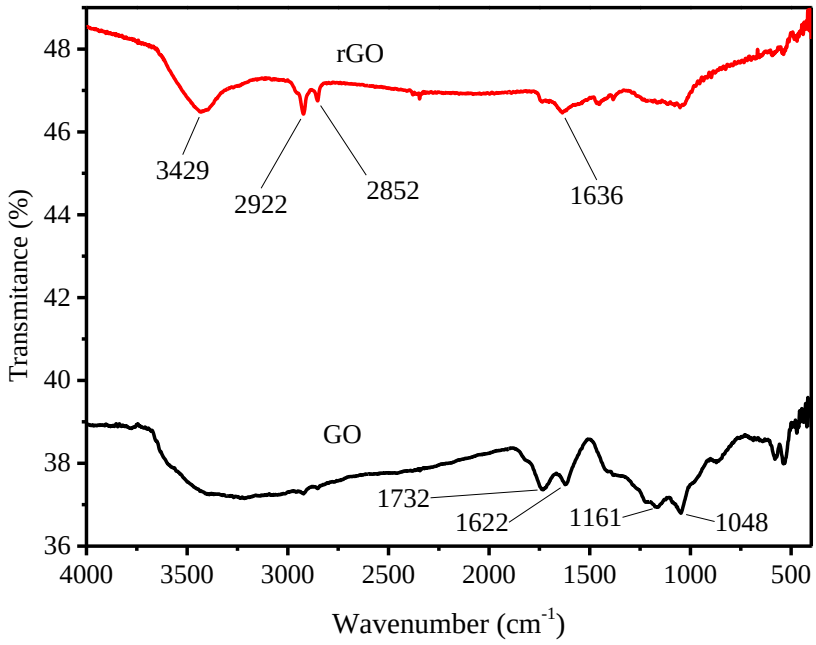

Figure 24. FTIR spectra of GO and rGO.

Further, the FTIR spectra of ZnO(P), CuO-ZnO(P), rGO-ZnO/CuO(P), and rGO-ZnO/CuO(P2) were measured over the range of 400-4000 cm^{-1} as shown in Figure 25. The bands at 3422 and 1300 cm^{-1} correspond to the O–H groups stretching and bending vibrational frequencies, respectively. Similarly, the bands at 1628 cm^{-1} could be attributed to the stretching vibrations of the C=O bond (Priyadharsan et al., 2018). The source of the O-H and C=O functional groups could be due to the adsorbed H_2O and CO_2 molecules during sample preparation. The M-O stretching vibrations of metal oxides usually appear in the ranges between 400 and 600 cm^{-1} of the FTIR spectrum. In light of this, the peaks in the range 400-510 cm^{-1} could belong to the Cu–O and Zn–O vibrations of CuO and ZnO, respectively (Harish et al., 2017). The ZnO(P) sample showed a peak at around 480 and 410 cm^{-1} corresponding to Zn-O vibrations (Islam et al., 2019). Similarly, the CuO-ZnO(P), rGO-ZnO/CuO(P), and rGO-ZnO/CuO(P2) samples showed peaks between 410 and 490 cm^{-1} belonging to the Cu-O and Zn-O vibration band (Islam et al., 2019;

Renuka et al., 2017). The peaks from rGO vibration were not visible due to the low rGO composition of the rGO-ZnO/CuO samples (Govindasamy et al., 2021).

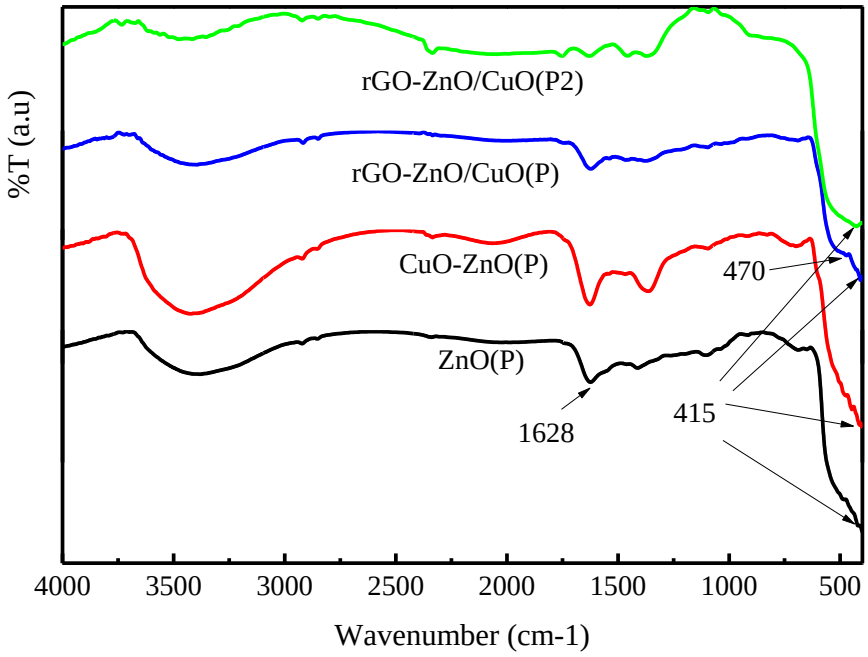

Figure 25. FTIR spectra of ZnO(P), CuO-ZnO(P), and rGO-ZnO/CuO(P) nanomaterials.

4.2.4. Photoluminescence Studies

Photoluminescence (PL) characterizations were carried out to investigate the effect of the components on the rate of the photogenerated charge carriers' recombination and the defect level of the materials. Hence, PL analysis of the materials employed for photocatalysis was conducted. The materials used for photocatalysis are those that are synthesized using VSB extracts: ZnO(B), and CuO-ZnO(B)-20% and PEG: ZnO(P), CuO-ZnO(P), rGO-ZnO/CuO(P), and rGO-ZnO/CuO(P2). The PL spectra of ZnO(B) and CuO-ZnO(B) suspension in methanol were displayed in Figure 26A. When the samples are excited at 340 nm, the PL spectra showed a strong emission band around 388 nm and a relatively weaker emission band around 463 nm including a shoulder band around 418 nm. The strong narrow emission band around 388 nm was attributed to the exciton recombination corresponding to the near band edge (L. Xu et al., 2017). Whereas the other peaks that appeared around 418 nm and 463 nm could be originated from deep-level defects (Lavín et al., 2019). Since PL emission is induced when the photogenerated e^-/h^+ recombine, the relatively lower PL intensity of the CuO-ZnO(B)-20%

compared to ZnO(B) indicated the decreased radiative recombination rate in the composite which could be attributed to the better e^-/h^+ separation and prolonged exciton lifetime (L. Xu et al., 2017). Thus, coupling CuO and ZnO revealed decreased rate of exciton recombination with improved visible light absorption (C. Chen et al., 2020).

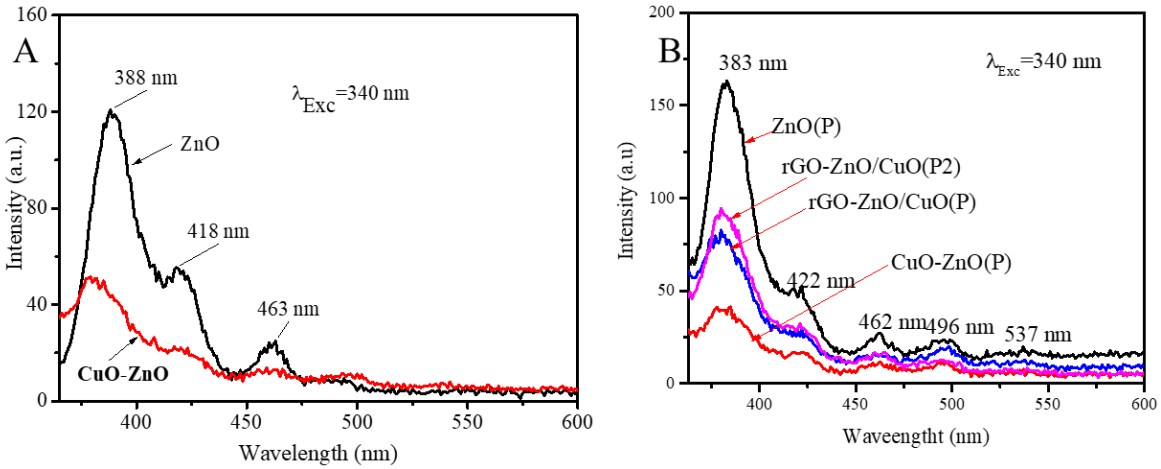

Figure 26. Photoluminescence spectra of ZnO(B) and CuO-ZnO(B)-20%, (B) ZnO, CuO-ZnO, and rGO-ZnO/CuO nanomaterials obtained using PEG.

Concerning ZnO(P), CuO-ZnO(P), rGO-ZnO/CuO(P), and rGO-ZnO/CuO(P2), the room temperature PL spectra were shown in Figure 26B. At an excitation wavelength of 340 nm, the PL spectra of ZnO(P), CuO-ZnO(P), rGO-ZnO/CuO(P), and rGO-ZnO/CuO(P2) samples showed an emission band similar to that of the ZnO(B) and CuO-ZnO(B)-20% with a strong emission band at around 383 nm originating from the near band edge of ZnO and relatively weaker emission bands at 462 and 496 nm originating from the deep-level defects (Lavín et al., 2019; L. Xu et al., 2017). As is displayed in Figure 26B, the emission intensity from pristine ZnO, i.e. ZnO(P), is higher than that of the composite both from the near band edge and from the defect levels, which could be attributed to the better e^-/h^+ separation and decreased defect level in the CuO-ZnO and rGO-ZnO/CuO NCs (Park et al., 2015; L. Xu et al., 2017). Therefore, modifying ZnO with CuO and rGO indicated the decreased recombination rate with improved visible light absorption could make the resulting modified nanomaterials a potential candidate for photocatalysis (C. Chen et al., 2020).

4.2.5. Morphological Analysis

The morphology of the synthesized nanomaterials was studied by using SEM and TEM images. The SEM image and EDS spectrum of the CuO NPs synthesized by MW-assisted method using CAL extract was illustrated in Figure 27. The SEM image indicated a uniformly distributed cluster of spherical-shaped morphology (Figure 27A). The image taken showed that some particles having spherical-shaped morphology are found in the clusters (Figure 27B). Furthermore, its EDS spectrum given in Figure 27C confirmed that the sample is composed of only Cu and O elements, supporting the XRD analysis.

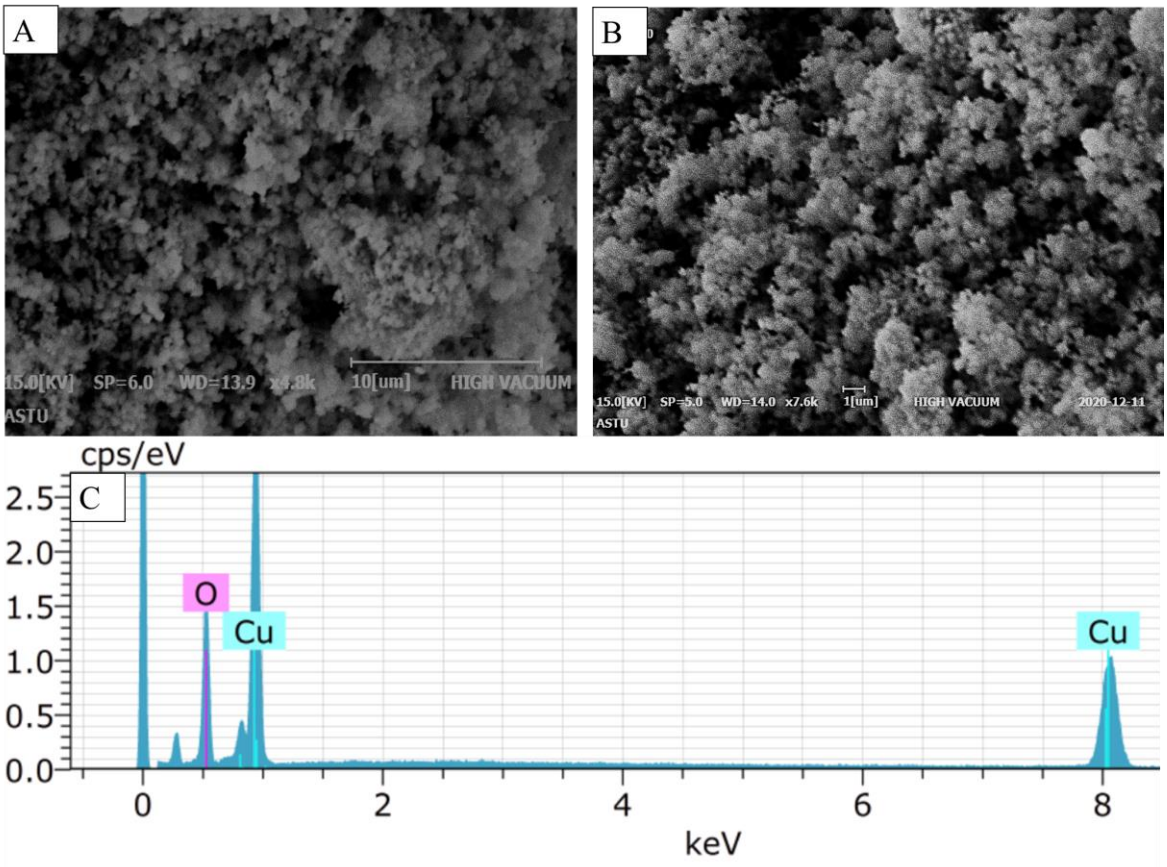

Figure 27. SEM images of CuO(L-10) synthesized with CAL extract (A) and its EDS spectrum(B).

The SEM images of the ZnO(B), CuO(B), and CuO-ZnO(B)-20% samples prepared using VSB extract were given in Figure 28A-C. The micrograms indicated that ZnO and CuO were found in a cluster of spherical-like NPs, while CuO-ZnO(B)-20% were found in a plate-like

morphology with noticeable pores. Further analysis using FESEM (Figure 28D-F) supports the SEM results.

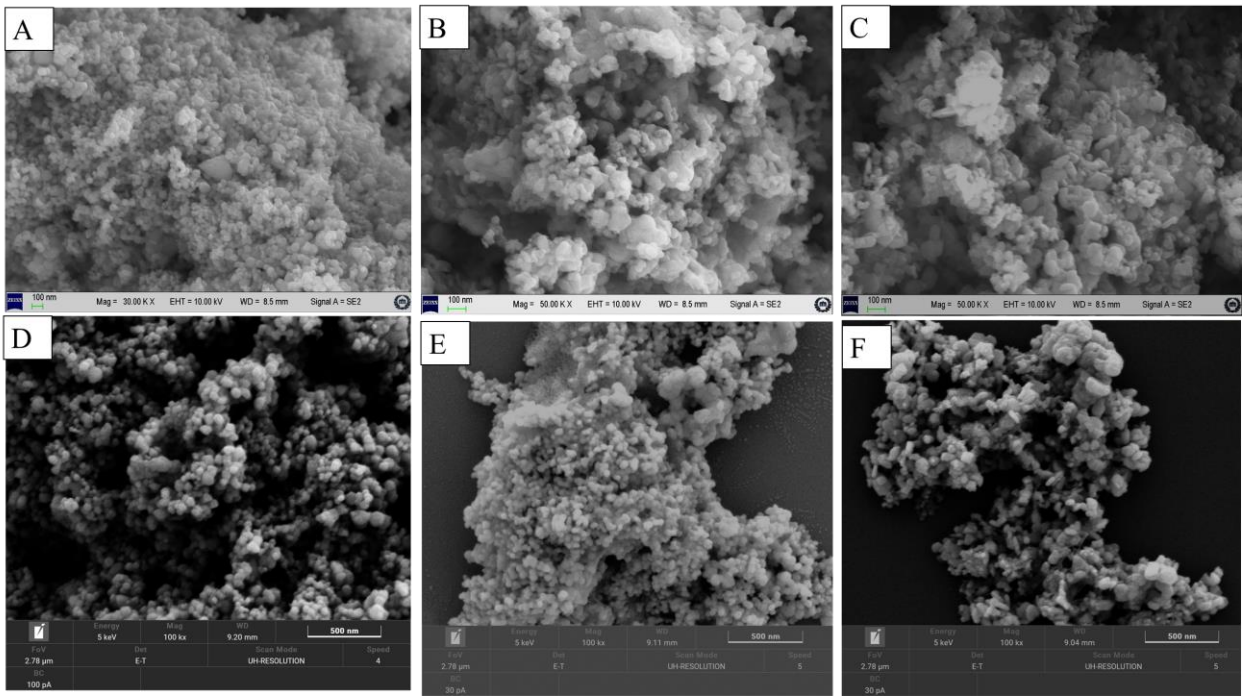

Figure 28. SEM images: (A, B) ZnO(B), (C,D) CuO(B), and (E,F) CuO-ZnO(B)-20%.,

The typical high-angle annular dark-field scanning transmission electron microscopy (HAADF-STEM) image (Figure 29A) and corresponding energy-dispersive X-ray spectroscopy (EDS) mappings of CuO-ZnO(B)-20% (Figure 29B-E) with EDS spectrum (Figure 29F) demonstrated the homogeneous distribution of Zn, Cu, and O elements throughout the CuO-ZnO(B)-20% sample (X. Lei et al., 2019). The morphology and crystal structure of the CuO-ZnO(B)-20% sample was further evaluated by TEM analysis, as depicted in Figure 29G. The result illustrated that the prepared CuO-ZnO(B)-20% possess plate-like nanostructures, supporting the SEM analysis. Following examination by HRTEM, the lattice fringes for CuO-ZnO(B)-20% were observed (Figure 29H). From the analysis, 0.26 nm interplanar spacing between the (002) planes of hexagonal ZnO (card no 000-036-1451), and 0.27 nm spacing between the (110) plane of monoclinic CuO (card no 00-048-1548) were observed. This result is very consistent with the literature reports and XRD analysis (J. Li et al., 2020; J. Zhang et al., 2019).

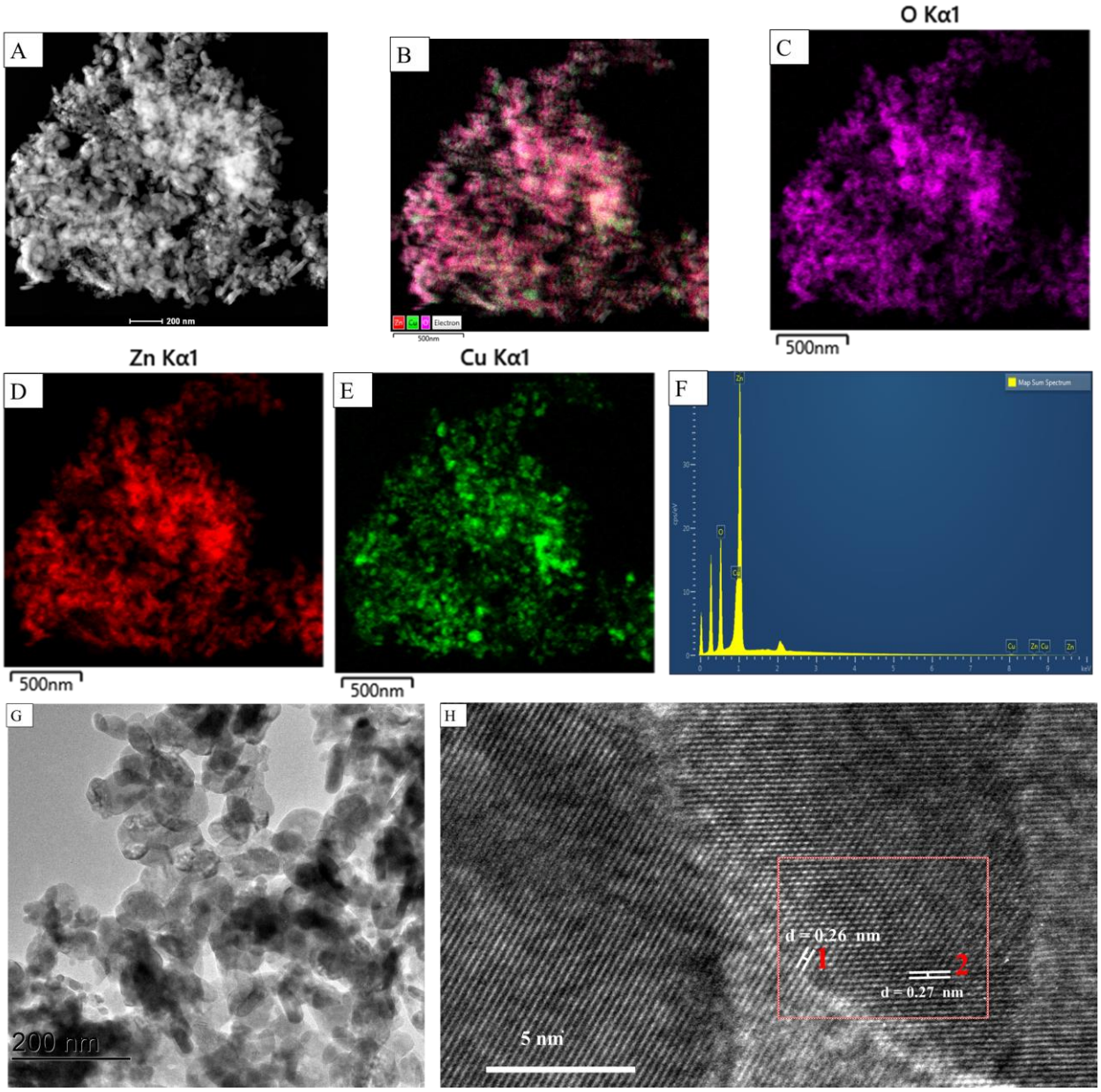

Figure 29. STEM image, EDS mappings/spectrum, and TEM images of CuO-ZnO(B)-20% samples: (A) HAADF-STEM image, (B) EDS layered mappings, EDS elemental mappings: (C) oxygen, (D) zinc, (E) copper, (F) EDS spectrum, (G) TEM image and (H) HRTEM lattice fringes.

In the case of nanomaterials prepared using PEG, the SEM images of ZnO(P), CuO-ZnO(P), rGO-ZnO/CuO(P), and rGO-ZnO/CuO(P2) samples were shown in Figure 30. Pristine ZnO (Figure 30A and B) samples are composed of hexagonal rod-like shaped nanoparticles with an

average diameter of 65 nm and different lengths. The SEM image of CuO-ZnO(P) samples (Figures 30C and D) displayed one-dimensional heterostructures (ribbon-like and short rod-like nanostructures). Similar to that of ZnO(P), rGO-ZnO/CuO(P) samples exhibited random arrays of rod-shaped morphology (Figures 30E and F). The high-magnification SEM micrographs (Figure 30F) showed that the whiskers or ribbon-like structures were uniformly distributed on the rod-like nanostructures. The NRs appear to be cylindrical with a few hexagonal shapes. The rod-shaped crystals fall in the nanoscale regime with an average diameter of 70 nm. Whereas varying the procedure of synthesis from two-step irradiation to a one-step resulted in a flower-like morphology rGO-ZnO/CuO(P2) (Figure 30F). The flower is an assembly of trigonal-shaped nanoplates/sheets.

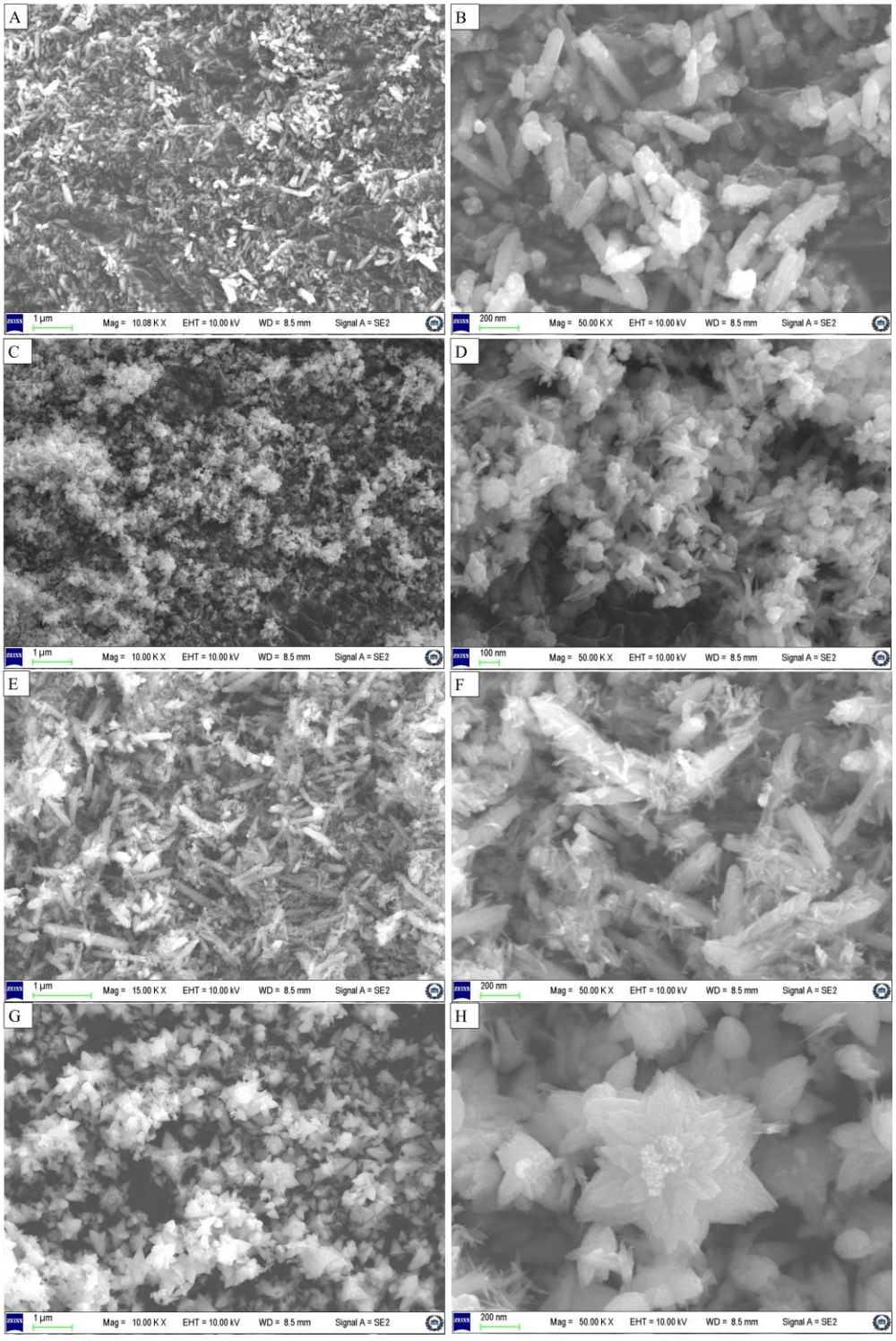

Figure 30. SEM images of (A,B) ZnO(P), (C,D) CuO-ZnO(P), (E,F) rGO-ZnO/CuO(P), and (G,H) rGO-ZnO/CuO(P2) samples with different resolution.

In addition, the EDS spectrum of the rGO-ZnO/CuO(P) and rGO-ZnO/CuO(P2) depicted in Figure 31A and G, respectively showed that the samples were composed of C, O, Cu, and Zn elements, confirming the presence of the expected elements in the samples. Furthermore, the EDS mapping analysis illustrated that Cu, Zn, C, and O elements were homogeneously distributed throughout the rGO-ZnO/CuO(P)(B-F) and rGO-ZnO/CuO(P2) (H-L) samples.

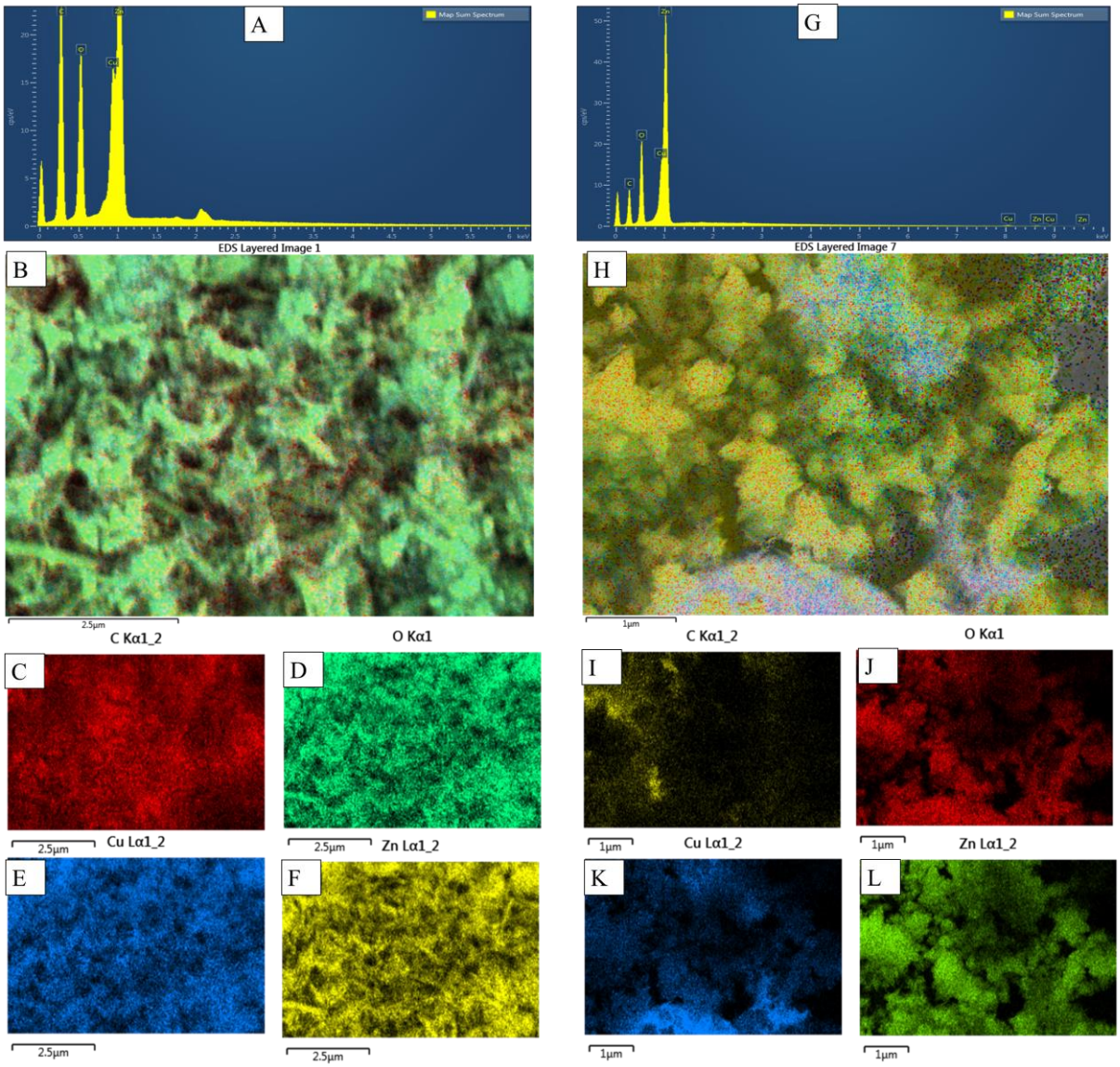

Figure 31. EDS spectra, EDS layered image, and elemental mappings (A-F) rGO-ZnO/CuO(P) and (G-L) rGO-ZnO/CuO(P2); elemental mappings: carbon (C&I), oxygen (D&J), copper (E&K), and zinc (F&L).

The homogenous distribution of elemental C throughout the composite sample could imply that the rGO sheets were integrated with the composite (Y. Wang et al., 2020). In addition, the absence of traces of other elements in the EDS spectra signifies the purity of the rGO-ZnO/CuO samples supporting the XRD data (A. Kumar et al., 2017).

The morphologies and structures of GO and rGO were investigated by TEM image analysis. TEM images of GO and rGO at different magnifications were depicted in Figure 32. A lower-resolution TEM image of GO shows multilayer flake-like structures (Figure 32A). A closer look at the thin transparent layers on the peripheries, however, reveals exfoliated GO sheets (Figure 32B) (Aziz et al., 2014). In the case of rGO, sheet-like morphologies were observed (Figures 32C and D). The lower resolution image (Figure 32C) consists of a thick dark region indicating overlapped sheets, and a transparent region with wrinkles corresponding to a thin graphene sheet (monolayer and few-layer) (Lee et al., 2019; J. Wang et al., 2017). The wrinkled appearances in the TEM image are the inherent properties of rGO. Wrinkles appear to be caused by coupling between folds of a graphene sheet through π-π interactions to attain thermodynamic stability (H. M. Ju et al., 2010). The results of the TEM image analysis of rGO support the XRD and UV-Vis analysis. Furthermore, the obtained result is consistent with previous reports (Amir Faiz et al., 2020; H. Liu et al., 2018).

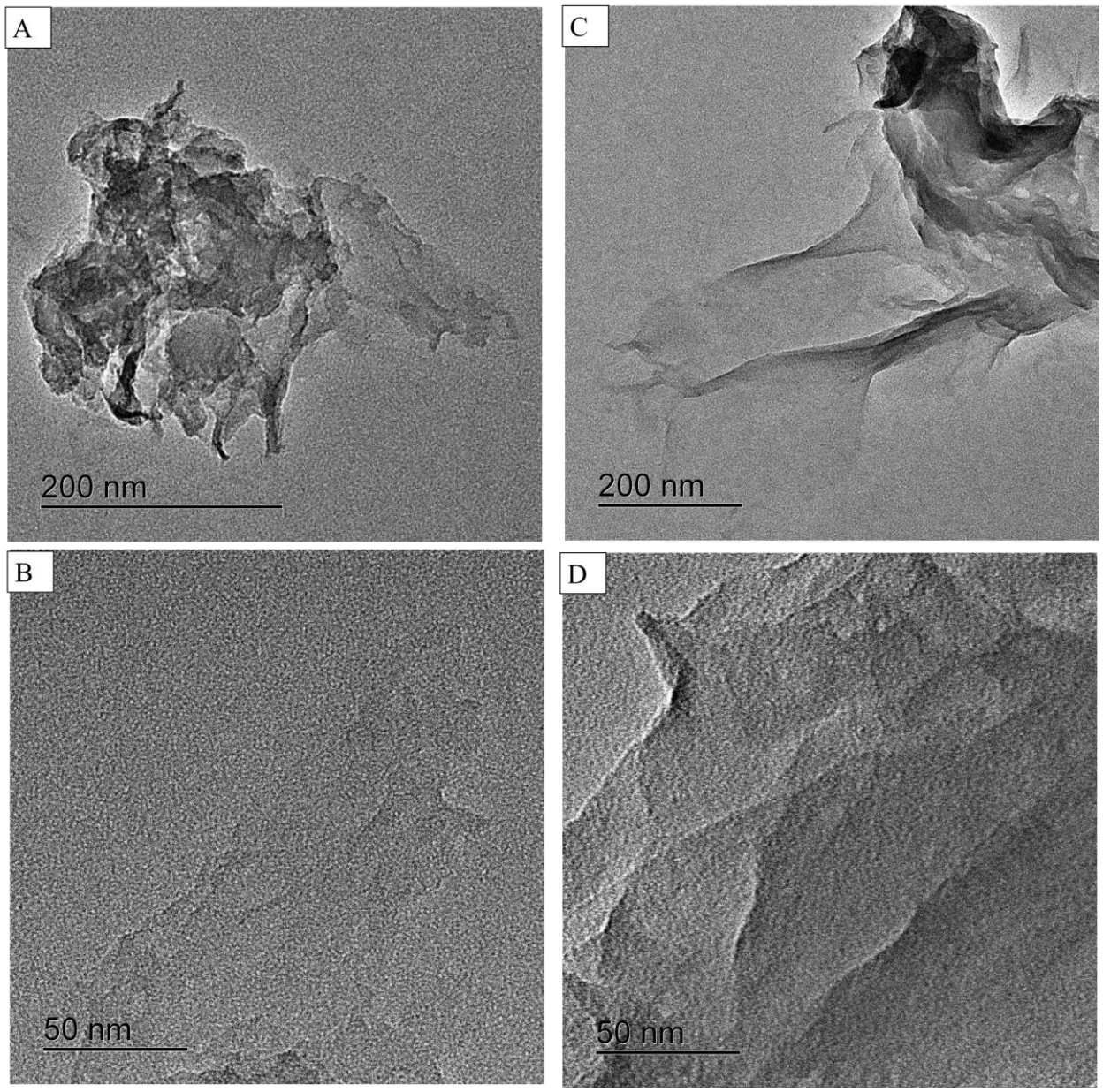

Figure 32. TEM images of GO (A, B) and rGO (C, D)

Figure 33 illustrates TEM images of rGO-ZnO/CuO(P) samples with rod-like morphologies, consistent with the SEM image. It is composed of particles that range from 230 nm to 780 nm in length and 30 nm to 96 nm in diameter. As shown in Figure 33, the microstructure exhibited lattice fringes, showing high crystallinity (Galani & Panda, 2019). The calculated inter-planar spacings were found to be 0.191 nm and 0.196 nm corresponding to the hexagonal ZnO (102) and monoclinic CuO (-112) planes, respectively. In both cases, the results agree with literature values [JCPDS 361451] for ZnO and [JCPDS 481548] for CuO.

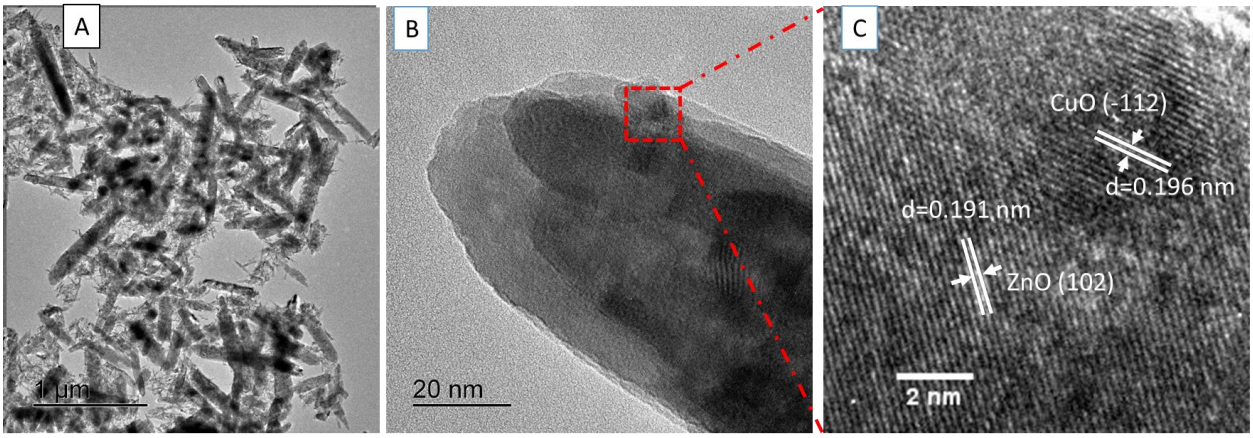

Figure 33. TEM images of rGO-ZnO/CuO(P) (A, B) and HRTEM (C).

4.2.6. XPS Analysis

XPS study was utilized for the survey of oxidation states and compositions of the CuO-ZnO(B)-20% nanocomposite samples surface. The XPS spectrum of the CuO-ZnO(B)-20% sample was displayed in Figure 34. The peaks observed in the full survey spectrum displayed in Figure 34A indicated the presence of O, Cu, and Zn species. As shown in Figure 34B, XPS peaks at 1021.26 and 1044.78 eV were assigned to the Zn energy levels designated as $2p_{3/2}$ and $2p_{1/2}$, respectively (X. Zhang et al., 2019). Similarly, the peaks centered at 933.18 and 952.88 eV were related to the $2p_{3/2}$ and $2p_{1/2}$ levels of Cu, respectively (Figure 34C) (C. Chen et al., 2020). Satellite peaks appeared at the upper energy sides, 943 eV for Cu 2p3/2 and 961 eV for Cu 2p1/2 (Figure 34C) confirming the existence of Cu in the Cu^{2+} state, i.e., CuO (Z. Zhang & Wang, 2012). Furthermore, the peak located at 530.18 eV is attributed to the O 1s from the lattice oxygen (O^{2-}) bound to metals, and the shoulder peak at 531.67 corresponds to the oxygen (O^{2-}) in the oxygen-deficient region indicating the presence of oxygen vacancy (O_V). Hence, the XPS study revealed the presence of CuO and ZnO in the CuO-ZnO(B)-20% sample, which is consistent with results from XRD, HRTEM, and EDS elemental mapping studies.

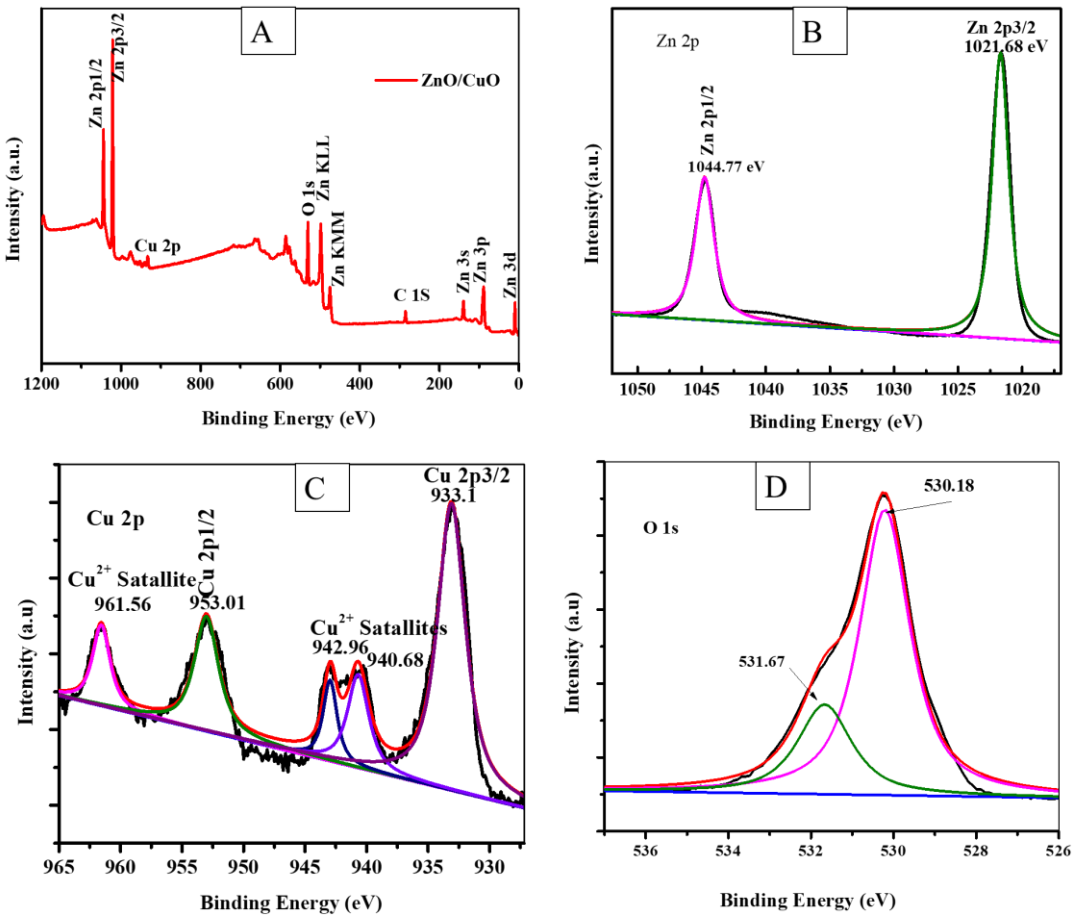

Figure 34. XPS spectra of CuO-ZnO(B)-20%: (A) full survey, (B) Zn 2p, (C) Cu 2p, and (D) O 1s

4.2.7. Surface Area Analysis

The surface area of the materials is one of the important characteristics that determine the performance of materials in several applications, particularly, in photocatalysis. In line with this, the surface area of the photocatalyst materials synthesized (ZnO(B), CuO(B), and CuO-ZnO(B)-20%) was analyzed. The N_2 adsorption-desorption isotherm and pore size distributions of ZnO(B), CuO(B), and CuO-ZnO(B)-20% samples were shown in Figure 35. As it was depicted in Figures 35A and B, the nitrogen adsorption-desorption isotherms of all samples exhibit typical type IV isotherms (J. Huang et al., 2010). According to the IUPAC classification, type IV isotherms are observed by the mesoporous adsorbents where the initial monolayer-multilayer adsorption on the mesopore walls is followed by the pore condensation (Thommes et al., 2015). The isotherms displayed type H3 hysteresis loop in the p/p^0 ranges of 0.62–0.99 indicating the

adsorption-desorption of the mesopore by capillary condensation (Figure 35B) (Thommes et al., 2015). According to the BET surface area analysis, the specific surface area calculated from the linear region of Figure 35A in the range of 0.05 to 0.3P/Po was given in Table 6. The linear fit was displayed in Figure 35C. The data showed that ZnO(B) and CuO-ZnO(B)-20% samples displayed a specific surface area of approximately 18 m^2/g. The pore size obtained by the BET method showed that CuO-ZnO(B)-20% samples possess a smaller adsorption average pore diameter of about 23.78 nm compared to the 38.99 nm and 39.64 nm adsorption average pore diameter for ZnO(B) and CuO(B) samples, respectively. The corresponding distribution of the pore sizes from the Barrett-Joyner-Halenda (BJH) method (Figure 35D) indicated that the textural porosity of all ZnO(B), CuO(B), and CuO-ZnO(B)-20% falls under mesoporous materials.

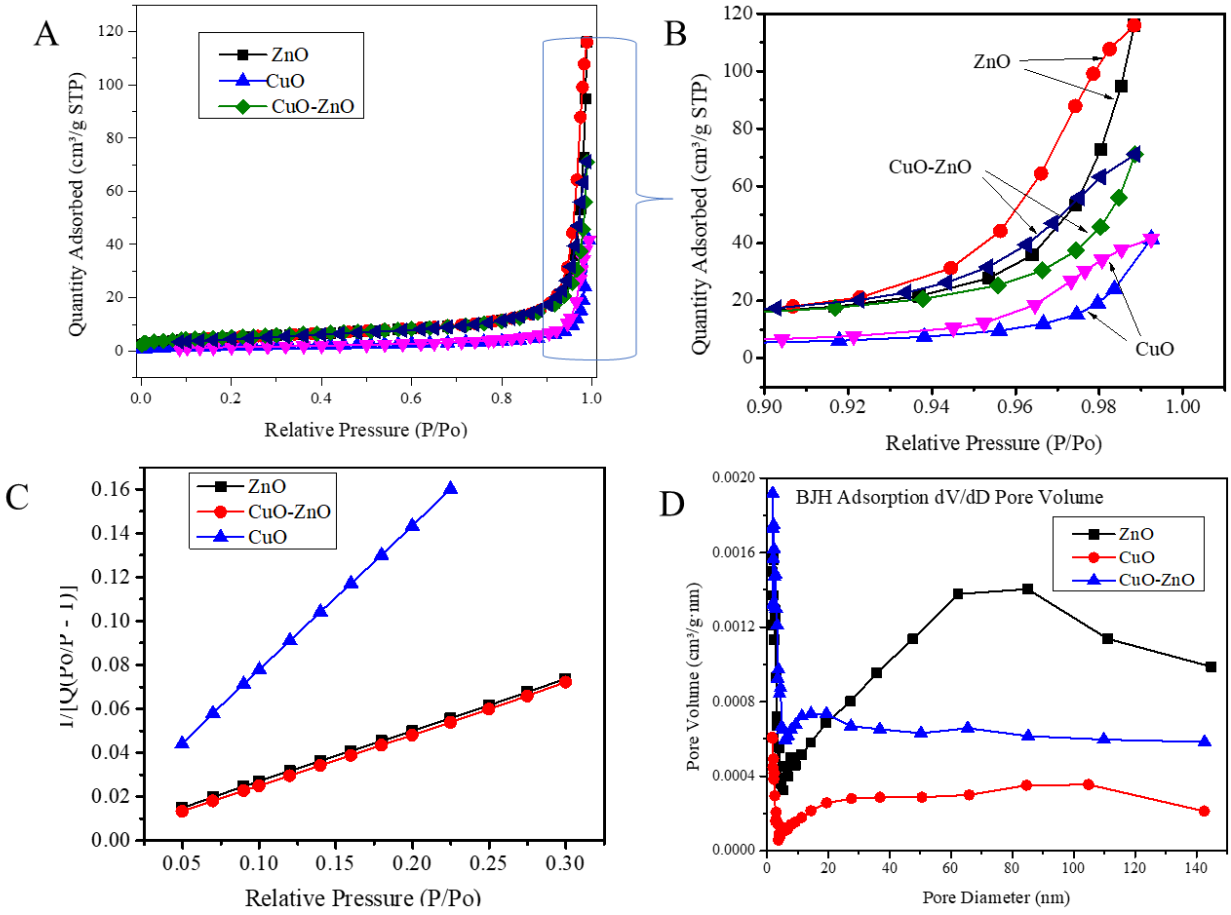

Figure 35. Adsorption-desorption isotherm of N_2 (A) and BJH pore size distribution of ZnO(B), CuO(B), and CuO-ZnO(B)-20% samples obtained using VSB.

Table 6. BET surface area, pore sizes, and pore volume distribution of ZnO(B), CuO(B), and CuO-ZnO(B)-20% samples.

Sample	**BET, m^2/g**		**Pore size, nm**	**Pore volume, cm^3/g**
		Corr. Coef/R^2		
ZnO(B)	18.4022	0.9999	38.997	0.179
CuO(B)	6.4843	0.9999	39.639	0.064
CuO-ZnO(B)-20%	18.4927	0.9999	23.782	0.110

4.2.8. Electrochemical Analysis

To understand the electrochemical behavior of the synthesized photocatalyst materials, electrochemical impedance spectroscopy and Mott-Schottky (MS) analyses were conducted. In this case, the EIS and MS results of CuO-ZnO(B)-20% were compared with ZnO(B), and that of rGO-ZnO/CuO(P) were compared with rGO-ZnO/CuO(P2), CuO-ZnO(P) and ZnO(P) as well as literature values.

4.2.8A. Electrochemical impedance spectroscopy analysis

The EIS was used to identify the resistive and capacitive properties of the materials describing the charge carriers' separation, transfer, and recombination behavior across the semiconductor-electrolyte interface of the nanomaterials. The EIS spectra of the nanomaterials synthesized using VSB (ZnO(B), CuO(B), and CuO-ZnO(B)-20%) were presented in Figure 36A. According to the Figure, the radius of the EIS spectra arc of the CuO-ZnO(B)-20% was smaller compared to that of pristine ZnO(B) and CuO(B) indicating lower resistance to the interface charge transfer rate of CuO-ZnO(B)-20% making it a better photocatalyst. Further, there is no small semicircle in the high-frequency region, meaning that the charge transfer resistance is negligible (X. Ju et al., 2020). Therefore, modifying ZnO by coupling with CuO suppressed the rate of charge carriers' recombination which is consistent with the results from the PL analysis (Figure 26B). On the other hand, the impedance analysis of ZnO(P), CuO-ZnO(P), rGO-ZnO/CuO(P), and rGO-ZnO/CuO(P2) was shown in Figure 36B. From the Figure, the CuO-ZnO(P) have shown the smallest impedance arc radius than ZnO(P), rGO-ZnO/CuO(P), and rGO-ZnO/CuO(P2) corresponding to high recombination resistance due to the fast electron

transfer across the interface between CuO-ZnO(P) and surrounding solution (Prabhu et al., 2019). In the EIS analysis, the smaller semicircle arc of the Nyquist plots indicates better conductivity of the materials (John et al., 2019). This implies that photocatalyst materials with smaller semicircles can facilitate the transfer of photogenerated charge carriers improving the photocatalytic performance of the materials. However, rGO-modified samples, rGO-ZnO/CuO(P) and rGO-ZnO/CuO(P2) with the same ratio of Cu to Zn displayed a larger impedance arc radius than CuO-ZnO(P) but smaller than bare ZnO(P). The obtained EIS results support the PL analysis given in Section 4.2.4 (Figure 26B).

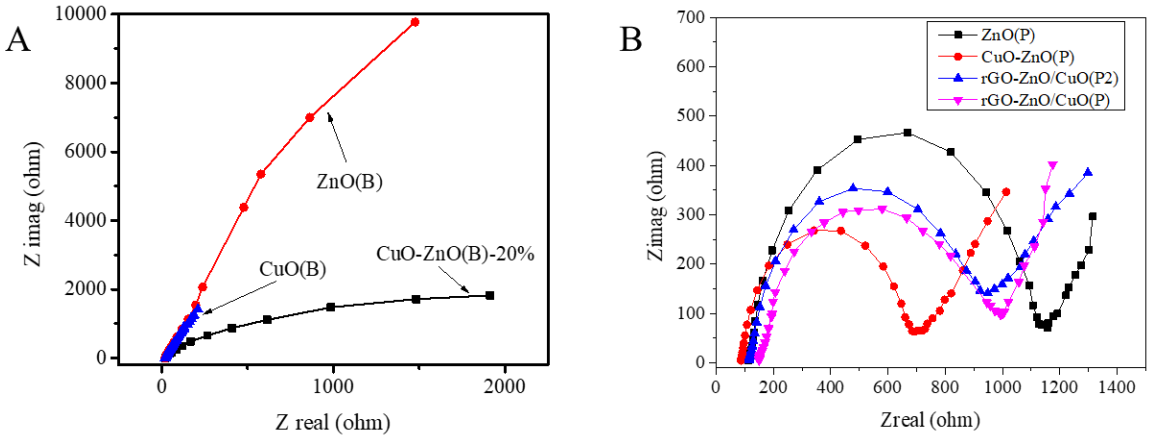

Figure 36. EIS Nyquist plots of nanomaterials obtained using (A) VSB: ZnO(B), CuO(B) and CuO-ZnO(B)-20%; (B) PEG: rGO-ZnO/CuO(P), rGO-ZnO/CuO(P2), CuO-ZnO(P), and ZnO(P).

4.2.8B. Mott-Schottky analysis

The Mott-Schottky plot analysis of the prepared samples was used to experimentally determine the approximate positions of the conduction (CB) and valence band (VB) of the semiconductors through the interpretation of impedance (Mott–Schottky) plots. The Mott–Schottky plots of ZnO(B), CuO(B), and CuO-ZnO(B)-20% were given in Figure 37. Flat band potential was obtained by extrapolating the plot of $1/C^2$ vs potential to the X-axis. As can be seen from the Figure, ZnO(B) and CuO-ZnO(B)-20% showed a positive slope indicating an n-type semiconductor with a flat band potential of -0.51 V and -0.73 V vs Ag/AgCl, respectively. CuO-ZnO(B)-20% was expected to show both positive and negative slopes. However, there are reports indicating only positive slope in the range displayed (Man et al., 2020). Whereas CuO(B)

showed a negative slope indicating a p-type semiconductor with a flat band potential of 0.82 V vs Ag/AgCl. The potential measured using Ag/AgCl reference electrode can be converted to the potential relative to the reversible hydrogen reference electrode (RHE) using the Nernst equation (Eqn. 23) (Wei et al., 2018).

$$E_{RHE} = E_{Ag/AgCl} + E^{0}_{Ag/AgCl} + 0.059\ pH \quad (23)$$

where $E^{0}_{Ag/AgCl(sat)}$ =0.197 V and the electrolyte pH is 7. Hence, the flat band potentials relative to RHE could be 0.10 V for ZnO(B), -0.12 V for CuO-ZnO(B)-20%, and 1.43 V for CuO(B). Flat band potentials of the n-type semiconductors are close to the conduction band edge and that of the p-type semiconductors is close to the valence band edge (F. Guo et al., 2021). Thus, the CB of ZnO(B) and CuO-ZnO(B)-20% could be 0.10 V and -0.12 V vs RHE, respectively. Similarly, the VB of CuO(B) could be around 1.43 V vs RHE. Combining these values with the bandgap energy obtained from Tauc's formula, the calculated VB of ZnO(B), CuO-ZnO(B)-20%, and the CB of CuO(B) can be calculated using Eqn. 24 (F. Guo et al., 2021).

$$E_{VB} = E_{CB} + E_{g} \quad (24)$$

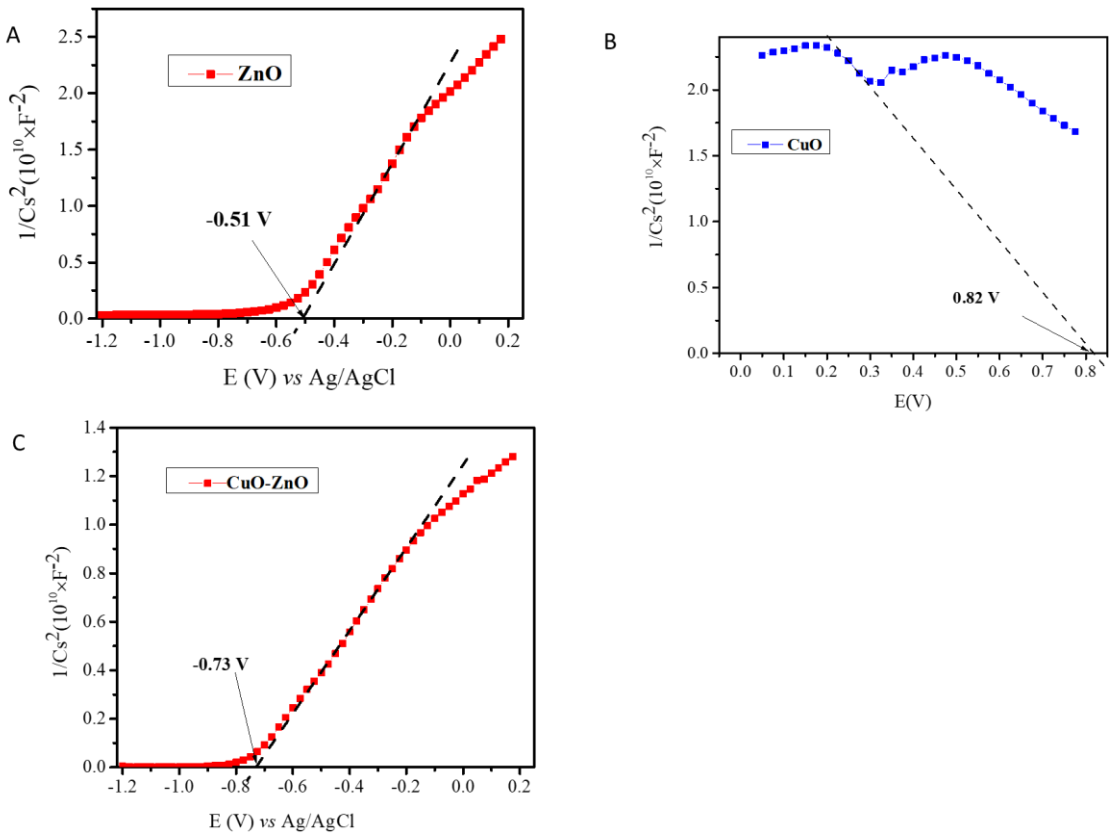

Figure 37. Mott-Schottky plots of nanomaterials obtained using VSB: (A) ZnO(B), (B) CuO(B), and (C) CuO-ZnO(B)-20% *vs* Ag/AgCl.

The bandgap energies were found to be 3.01 eV for ZnO(B), 2.74 eV for CuO-ZnO(B)-20%, and 2.18 eV for CuO(B). Therefore, the calculated VB edge position of ZnO, CuO-ZnO(B)-20%, and CB edge position of CuO(B) are 3.11, 2.62, and -0.75 V, respectively.

With regard to the ZnO(P), CuO-ZnO(P), rGO-ZnO/CuO(P), and rGO-ZnO/CuO(P2) nanomaterials, the Mott–Schottky plots were illustrated in Figure 38. The Mott–Schottky plot of ZnO(P) showed a positive slope indicating the n-type semiconductor with the flat band potential -0.4 V. However, in the case of rGO-ZnO/CuO(P) rGO-ZnO/CuO(P2), and CuO-ZnO(P), both negative and positive slopes were observed indicating the development of p-n heterojunction between the p-type CuO and the n-type ZnO (H. Xu et al., 2020). Thus, the co-existence of positive and negative slopes with flat band potential values, -0.4 V for ZnO, -0.4 and 1.2 V for CuO-ZnO(P), -0.37 and 1.3 V rGO-ZnO/CuO(P), -0.32 and 1.2V rGO-ZnO/CuO(P2) were shown in Figures 38A-D relative to the Ag/AgCl electrode. The

corresponding flat band potential relative to RHE were given in Table 7. Using the flat band potentials and the previously calculated band gaps, the conduction and valence band potentials of ZnO(P), CuO-ZnO(P), rGO-ZnO/CuO(P2), and rGO-ZnO/CuO(P2) were calculated (Table 7).

Table 7. Summary of the flat band, CB, and VB potentials of ZnO and CuO components for ZnO(P), CuO-ZnO(P), rGO-ZnO/CuO(P), and rGO-ZnO/CuO(P2) from Mott-Schottky plots.

Nanomaterials	**Band gap (eV)**	**Flat band (V)**		**CB (V)**		**VB (V)**	
		ZnO	CuO	ZnO	CuO	ZnO	CuO
ZnO(P)	3.14	0.21		0.21		3.35	
CuO-ZnO(P)	2.91	0.21	1.81	0.21	-1.1	3.12	1.81
rGO-ZnO/CuO(P)	2.48	0.24	1.91	0.24	-0.57	2.72	1.91
rGO-ZnO/CuO(P2)	2.32	0.29	1.81	0.29	-0.51	2.61	1.81

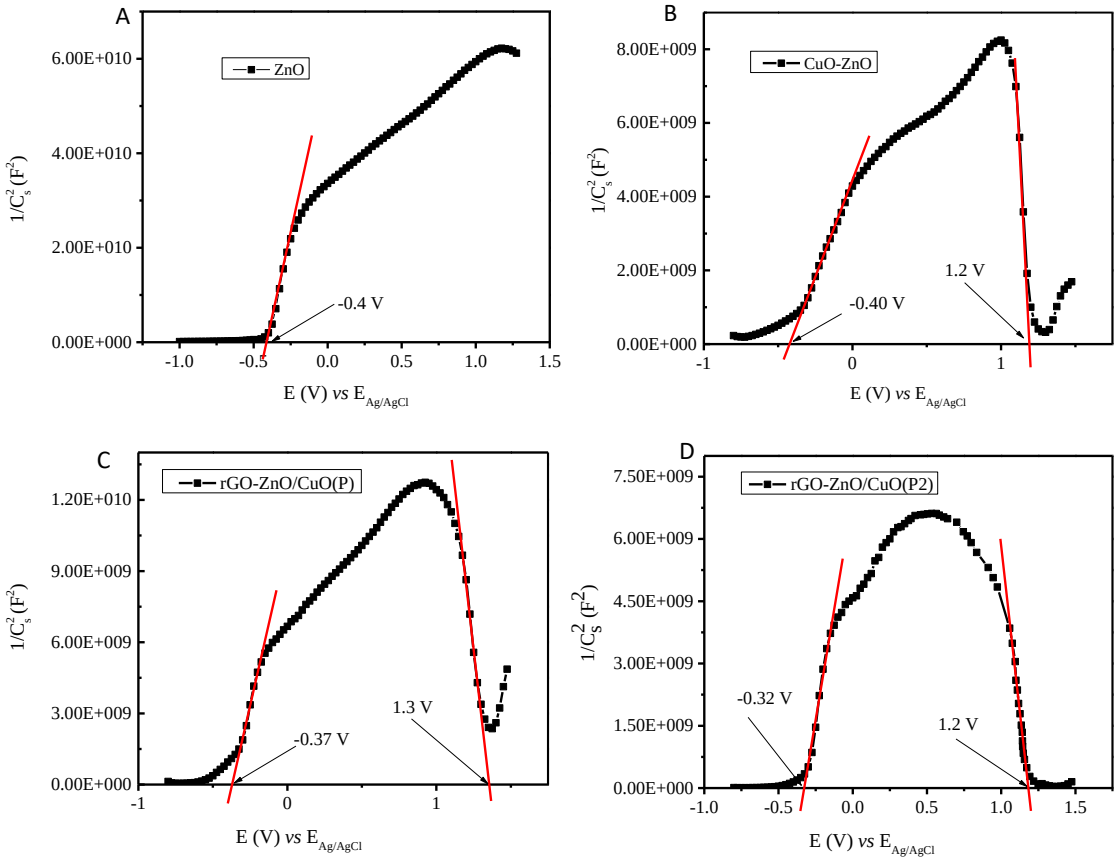

Figure 38. Mott-Schottky plots of (A) ZnO(P), (B) CuO-ZnO(P), (C) rGO-ZnO/CuO(P), and (D) rGO-ZnO/CuO(P2) *vs* Ag/AgCl.

4.3. Applications of the Synthesized Nanomaterials

The nanomaterials prepared using CAL, VSB, and PEG were employed for catalytic reduction of 4-NP, photocatalytic degradation of MB, and antibacterial activities. In this regard, CuO(L-10) was employed for 4-NP reduction and antibacterial activity; CuO-ZnO(B)-20% and rGO-ZnO/CuO(P) were employed for catalytic reduction of 4-NP, photocatalytic degradation of MB, and antibacterial applications. The rate of reaction and proposed mechanisms of each of these applications were given in detail.

4.3.1. Catalytic Reduction

The reduction of 4-NP into 4-AP by $NaBH_4$ is a thermodynamically feasible reaction (Zelekew & Kuo, 2017). However, the rate of reduction reaction is slow due to the kinetic barrier in the

reaction steps. Catalysts allow the reaction to take routes with relatively lower energy barriers leading to a faster rate of reaction. Nanostructured catalysts were often employed to accelerate the reduction of 4-NP into 4-AP by $NaBH_4$. The performance of the as-synthesized CuO(L-10) as a catalyst was evaluated against 4-NP reduction in the presence of $NaBH_4$ as a reducing agent. Figure 39 shows the reduction of 4-NP into 4-aminophenol. The UV-vis absorbance of 4-NP in the absence of $NaBH_4$ displayed a peak at around 319 nm. However, the peak at 319 nm disappeared and a new intense peak at around 405 nm appeared when $NaBH_4$ was added to the 4-NP solution (Figure 39A). In alkaline media, a light yellowish 4-NP solution changes to an intense yellowish-orange 4-nitrophenolate ion with absorbance at around 405 nm (Figure 39A). The intense spectra of the mixture of 4-NP and $NaBH_4$ without catalysts showed slight change over the 27 min period, indicating the slow 4-NP reduction reaction (Figure 39B).

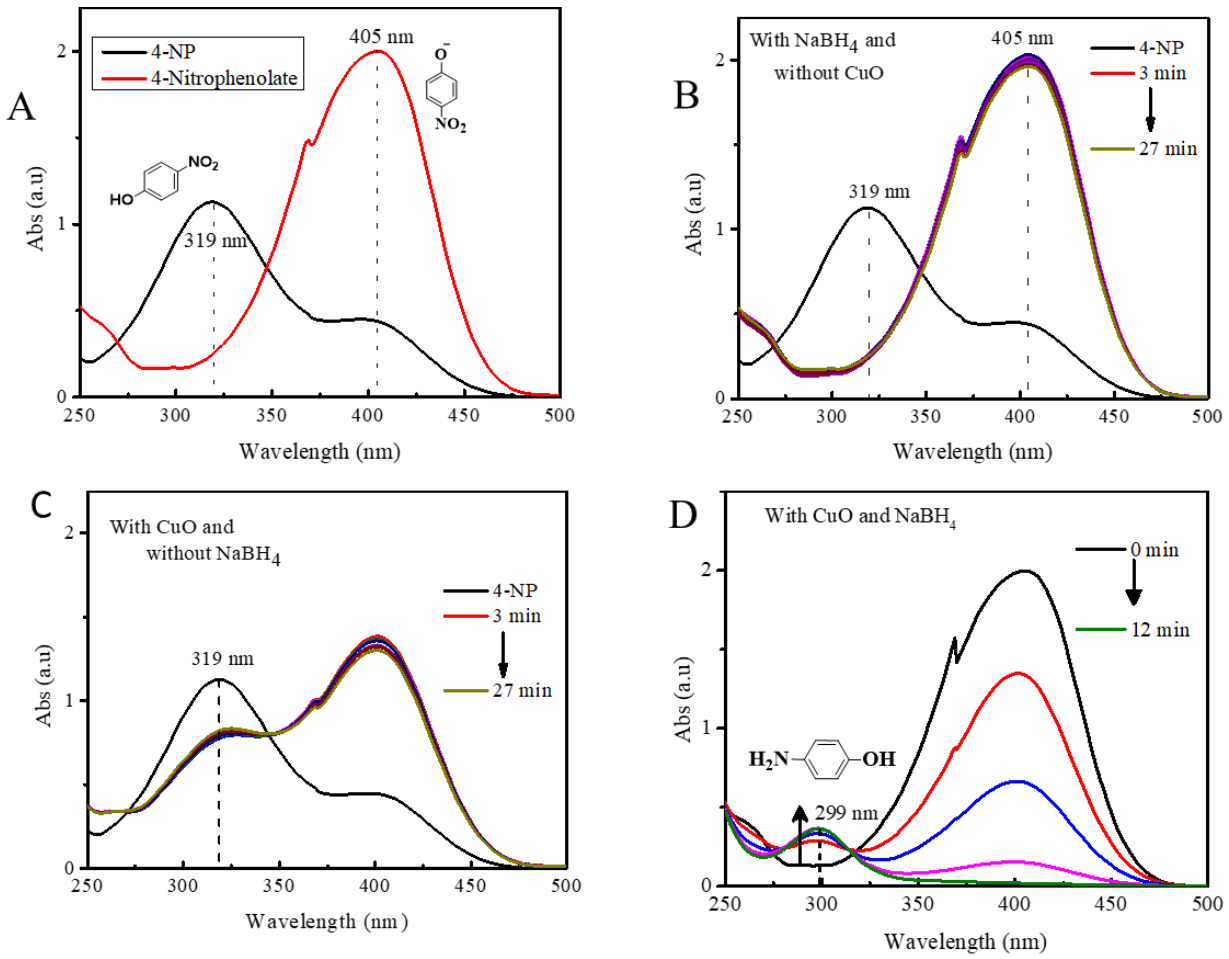

Figure 39. Absorption spectra of 4-NP aqueous solution: (A) before and after the addition of $NaBH_4$, (B) with $NaBH_4$ for 27 min, (C) with CuO after 27 min, (D) in the presence of both $NaBH_4$ and CuO catalyst for 12 min.

After CuO(L-10) catalyst addition to the mixture of 4-NP and $NaBH_4$, the peak at 405 nm was gradually decreasing while the new peak at around 299 nm started growing, representing the conversion of the 4-nitrophenolate ion into 4-aminophenol as indicated in Scheme 5 and Figure 39D. The time taken for the complete conversion of 4-NP was measured based on the disappearance of the absorbance peak at around 405 nm in the presence of CuO(L-10) catalyst. It took less than 12 min for the complete conversion of 4-NP into 4-aminophenols when both CuO(L-10) and $NaBH_4$ were used together, while only slight change was observed in the absence of either the catalyst or $NaBH_4$ (Figure 39D). The pH at which the CuO NPs were synthesized has a significant influence on the reducing capability of the resulting CuO catalysts. As depicted in Figure 40A-C, CuO NPs synthesized at pH 7 performed better than those

synthesized at higher pH values. The difference in performance could be due to the variation in the surface charge of the materials synthesized at different pH (Yuan et al., 2014).

The kinetics of the 4-NP reduction reaction in the presence of CuO catalyst synthesized at different pH values was shown in Figure 40D and Figure 41. The calculated rate constant of the reduction reaction is the highest for CuO catalyst synthesized at pH 7 using CAL extract. In the reduction of 4-NP, the surface having a positive surface charge facilitates the adsorption of both BH_4^- and 4-nitrophenolate anions on their surfaces, which could make the transfer of hydride from the BH_4^- to 4-nitrophenolate fast. Consequently, fast rate of reaction (A. Sharma et al., 2017). Since the concentration of $NaBH_4$ is much higher than that of 4-NP, the analysis was done using concentration 4-NP alone (Imangaliyeva et al., 2019). The apparent rate constant (k_{app}) of the reaction obtained from the slope of the linear fit plots of $\ln(C_t/C_o)$ *vs* t (pseudo-first-order) and $1/C_t$ *vs* t (pseudo-second-order) were given in Figure 41 and Table 8 with the corresponding correlation coefficients. The applicability of the kinetics model was decided by comparing R2 values (correlation coefficients) (K. Sharma et al., 2017). In the present work, a higher value of correlation coefficients for the pseudo-first-order compared to the second-order kinetic indicates that the experimental data of 4-NP catalytic reduction using CuO(L-10) well followed the pseudo-first-order rate model (Eqn. 19).

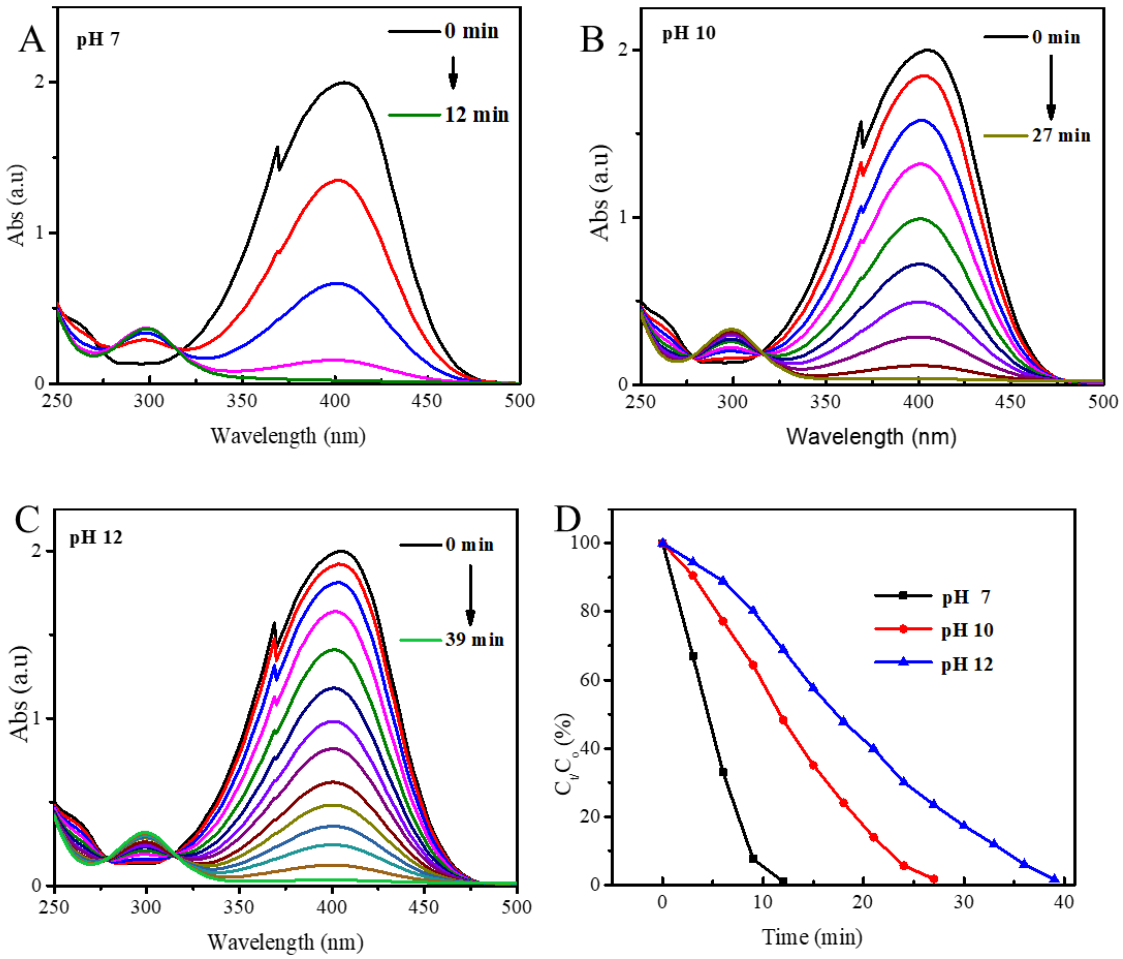

Figure 40. Reduction of 4-NP using CuO(L-10) nanostructures synthesized at different pH value: (A) pH=7, (B) pH=10, (C) pH=12, (d) plots of C_t/C_0 versus reaction time (min)

Table 8. Rate constants of CuO(L-10) in the reduction of 4-NP from 1st and 2nd-order linear fits.

Catalyst	**1st order fit**		**2nd order fit**	
	Rate constant /min^{-1}	R^2	Rate constant /$min^{-1}ppm^{-1}$	R^2
CuO(L-10)@pH7	0.37947	0.8902	3.49299	0.46122
CuO(L-10)@pH 10	0.13659	0.86263	0.65013	0.41913
CuO(L-10)@pH 12	0.08811	0.84097	0.3878	0.33115

The catalytic performance of the CuO(L-10) nanocatalyst is compared with previously reported CuO-based nanocatalysts for the 4-NP reduction under different reaction conditions (Table 9). The results indicated that the CuO NPs synthesized using CAL extract performed well against

4-NP reduction with activity parameters constant (ratio constant k_r) of 75.8 $min^{-1}g^{-1}$. This value is higher than that reported for CuO nanoleaves, CuO@C, and CuO/ZnO/Eggshell NCs (Bhattacharjee & Ahmaruzzaman, 2015; Kassem et al., 2021; X. Zhang et al., 2019).

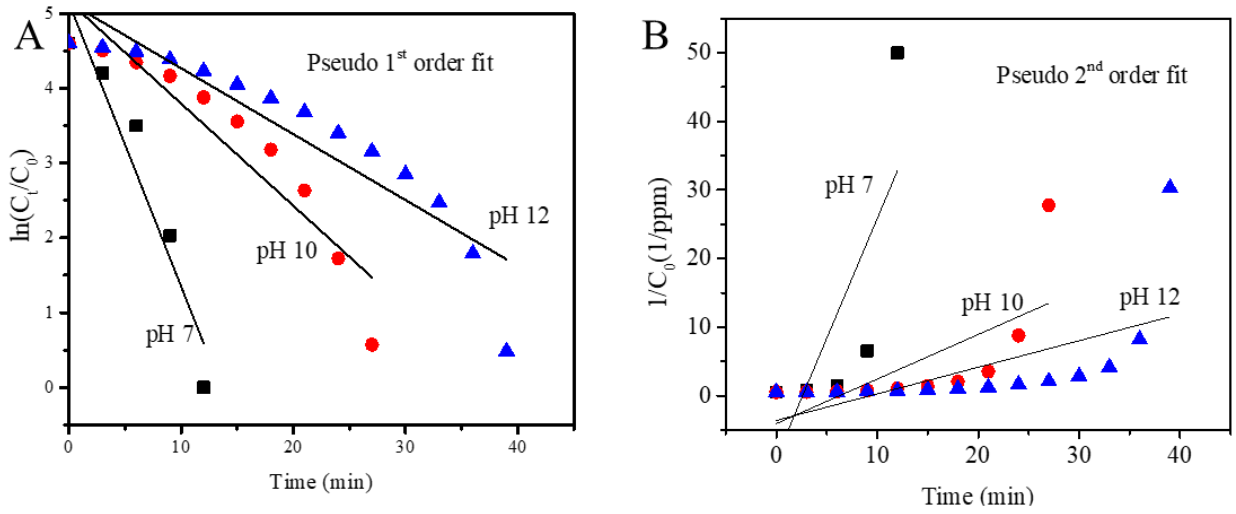

Figure 41. Plots of pseudo 1st and 2nd order fit of CuO(L-10) synthesized at different pH: (A) plot of $\ln(C_t/C_0)$ *vs* t, (B) plot of $1/C_t$ *vs* t.

Table 9. Comparison of the catalytic activity of CuO NPs with the previously reported CuO-based catalysts for the reduction of 4-NP.

Catalyst	4-NP ($x10^{-3}$ mmol)	$NaBH_4$ ($x10^{-3}$ mmol)	Catalyst amount (mg)	Time (min)	Rate constant, k_{app} (min^{-1})	Ratio constant k_r, ($min^{-1}g^{-1}$)	Ref.
CuO	0.36	30	1	15	0.022	22	(Bhattacharjee & Ahmaruzzaman, 2015)
CuO	0.25	50	2	4	0.565	282.5	(Sahu, Singhal, et al., 2020)
Pd/CuO	62.5	6250	7	1	3.3	471	(Nasrollahzadeh, Sajadi, Rostami-Vartooni, et al., 2015)
CuO@C	100	2250	50	18	0.36	7.2	(Kassem et al., 2021)
CuO/ZnO/Eggshell	2	1320	20	30	0.2037	6.79	(X. Zhang et al., 2019)
CuO/Cu_2O	0.25	50	0.1	4	0.5014	125.35	(Sahu, Satpati, et al., 2020)
CuO	14.38	528	5	12	0.379	75.8	present work

Similarly, the catalytic reduction activity of CuO-ZnO(B)-20% catalysts was also tested for 4-NP. For comparison purposes, the performance of ZnO(B) was also tested for the reduction of 4-NP. The progress of reduction and corresponding kinetics in the presence of ZnO(B) and CuO-ZnO(B)-20% catalysts were given in Figure 42. Upon the addition of CuO-ZnO(B)-20% powder to the solution of 4-NP and $NaBH_4$, the peak intensity at 405 nm drops while a new peak at 300 nm emerges confirming the 4-AP formation. CuO-ZnO(B)-20% showed strong catalytic efficiency with reaction completion in less than 12 min (Figures 42B and C). On the other hand, ZnO(B) showed insignificant change in the 4-nitrophenolate ion (in 12 min) suggesting the lower catalytic performance of ZnO(B) compared to CuO-ZnO(B)-20% against the reduction of 4-NP.

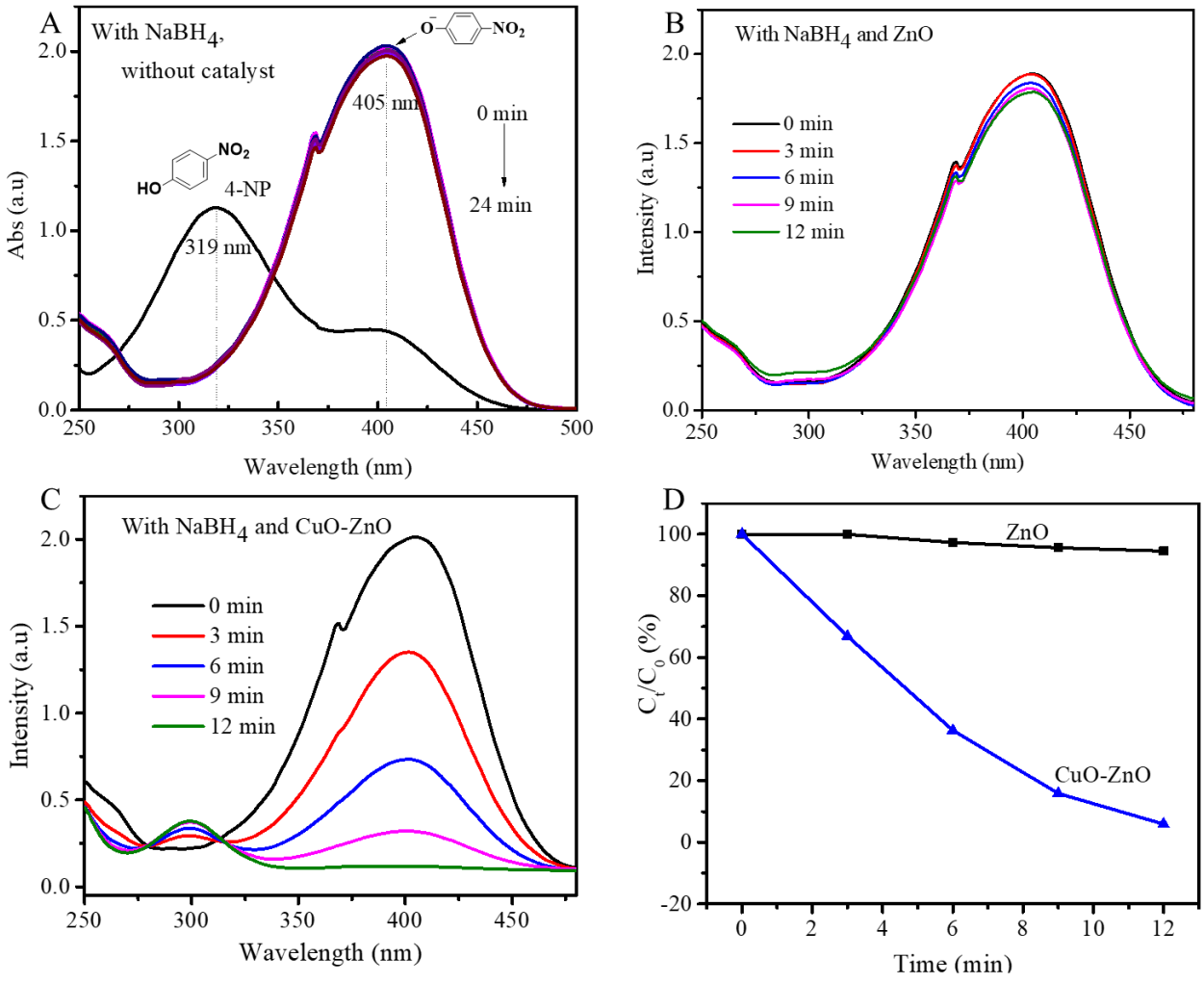

Figure 42. Absorption spectra of 4-NP: (A) with and without $NaBH_4$, (B) with $NaBH_4$ and ZnO(B), (C) CuO-ZnO(B)-20%; and (D) plots of C_t/C_0 *vs* reaction time (min).

Besides, the reduction kinetics of 4-NP with $NaBH_4$ and catalysts was shown in Figure 42D and Figure 43. The rate of reduction reaction fit was tested for both pseudo-first and Pseudo-second order reactions (Figure 43). The rate constants of the reduction reaction were obtained from the slope of the linear fitted plots of $\ln(C_t/C_o)$ *vs* time (for 1st order) and $1/C_t$ (for 2nd order) of reaction as depicted in Figure 43A (applying Eqn. 19, Eqn. 20) and Table 10. The result indicated that rate of reduction of 4-NP using ZnO(B) fits both Pseudo-1st and Pseudo-2nd order reactions which could be due to the insignificant catalytic activity of ZnO(B). However, the CuO-ZnO(B)-20% nanocatalyst showed significant reduction activity and the rate fitted better

the Pseudo-1st order reaction with the corresponding the ratio constants k_r of 5.925 $min^{-1}g^{-1}$ (X. Zhang et al., 2019).

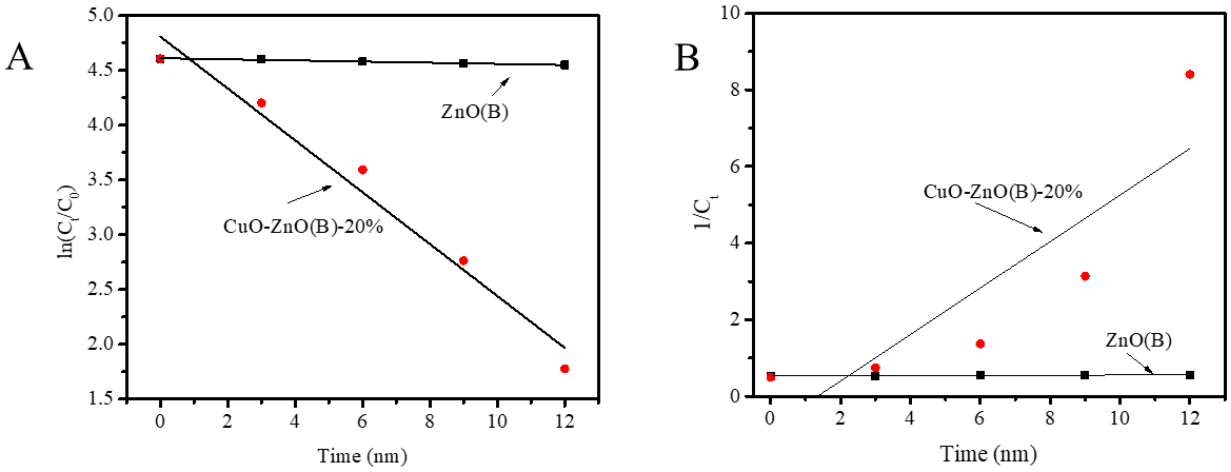

Figure 43. Kinetic analysis for 4-NP reduction: (A) plot of $\ln(C_t/C_0)$ *vs* t (pseudo 1st order fit), (B) plot of $1/C_t$ *vs* t (pseudo 2nd order fit).

Table 10. Rate constants of ZnO(B) and CuO-ZnO(B)-20% in the reduction of 4-NP from 1st and 2nd-order linear fits.

Catalyst	**1st order fit**		**2nd order fit**	
	Rate constant/min^{-1}	R^2	Rate constant/$min^{-1}ppm^{-1}$	R^2
ZnO(B)	0.00523	0.9345	0.00285	0.9354
CuO-ZnO(B)-20%	0.23654	0.9645	0.60683	0.6921

Similarly, the performance of ZnO(P), CuO-ZnO(P), rGO-ZnO/CuO(P), and rGO-ZnO/CuO(P2) was also tested against the 4-NP reduction. Their progress of reduction was presented in Figure 44. Upon addition of rGO-ZnO/CuO(P) to the $NaBH_4$ containing 4-NP solution, absorbance at 405 showed decreasing while a new peak at 300 nm appeared revealing the formation of 4-AP. rGO-ZnO/CuO(P2), CuO-ZnO(P), and ZnO(P) were also used for comparison purposes. The result indicated that both rGO-ZnO/CuO(P) and CuO-ZnO(P) reduced almost all 4-NP in less than 9 minutes, while it took rGO-ZnO/CuO(P2) to reduce all 4-NP about 21 min. whereas ZnO(P) exhibited insignificant catalytic activity suggesting the

poor catalytic performance of ZnO(P) compared to CuO-ZnO(P), rGO-ZnO/CuO(P), and rGO-ZnO/CuO(P2) (Figures 44A-D).

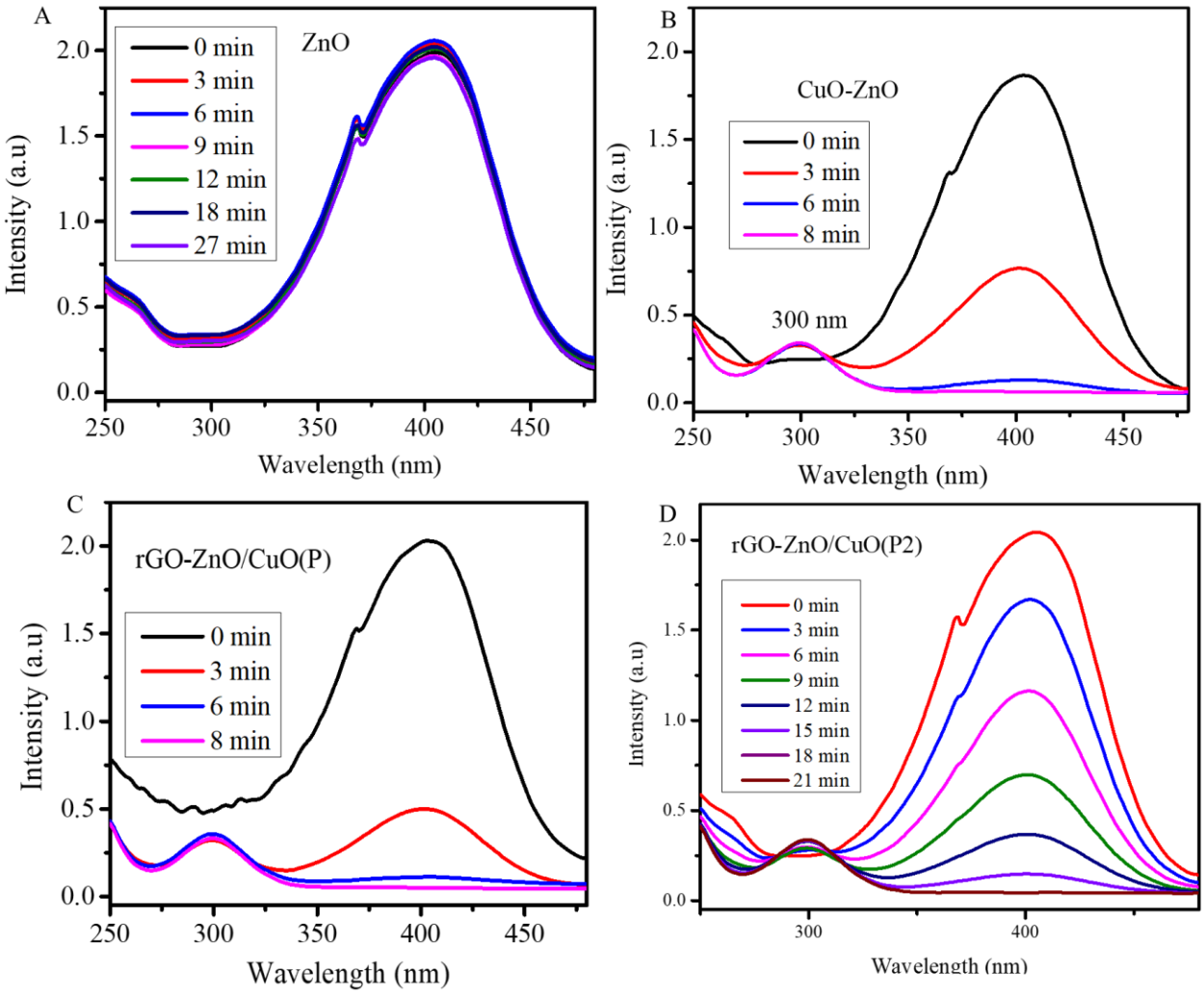

Figure 44. Absorption spectrum of 4-NP: progress of catalytic reduction using catalysts (A) ZnO(P), (B) CuO-ZnO(P), (C) rGO-ZnO/CuO(P), and (D) rGO-ZnO/CuO(P2).

Further, the kinetics of the catalytic reduction was tested for pseudo 1st and 2nd order reactions using the linear fits of Eqn. 19 and 20 (Figure 45 and Table 11). The results indicated that the data best fit with the pseudo-first-order reaction equation (Eqn. 19) as shown in Figure 45A (Imangaliyeva et al., 2019). From the slope of the linear fitted plot of $\ln(C_t/C_o)$ *vs* time of reaction, the rate constants of ZnO(P), CuO-ZnO(P), rGO-ZnO/CuO(P), and rGO-ZnO/CuO(P2) were found to be 0.00026, 0.465, 0.468, and 0.12058 min^{-1}, respectively. The

result showed that the rate of reduction reaction was high when the NCs were used compared to the pristine ZnO (i.e., ZnO(P)). In addition, rGO-ZnO/CuO(P) showed enhanced rate of reduction compared to rGO-ZnO/CuO(P2). The difference could be accounted based on the difference in the surface charges that affect the adsorption capacity of the catalyst.

Table 11. Rate constants (k) of ZnO(P) and CuO-ZnO(P), and rGO-ZnO/CuO(P) in the reduction of 4-NP from 1st and 2nd order linear fits.

Catalyst	**1st order fit**		**2nd order fit**	
	k/min^{-1}	R^2	$k/(ppm^{-1}\ min^{-1})$	R^2
ZnO(P)	0.000260	-0.49724	0.000141	-0.4967
CuO-ZnO(P)	0.46539	0.97303	1.85139	0.78643
rGO-ZnO/CuO(P)	0.46806	0.99834	2.34069	0.77412
rGO-ZnO/CuO(P2)	0.12058	0.94783	0.10461	0.84623

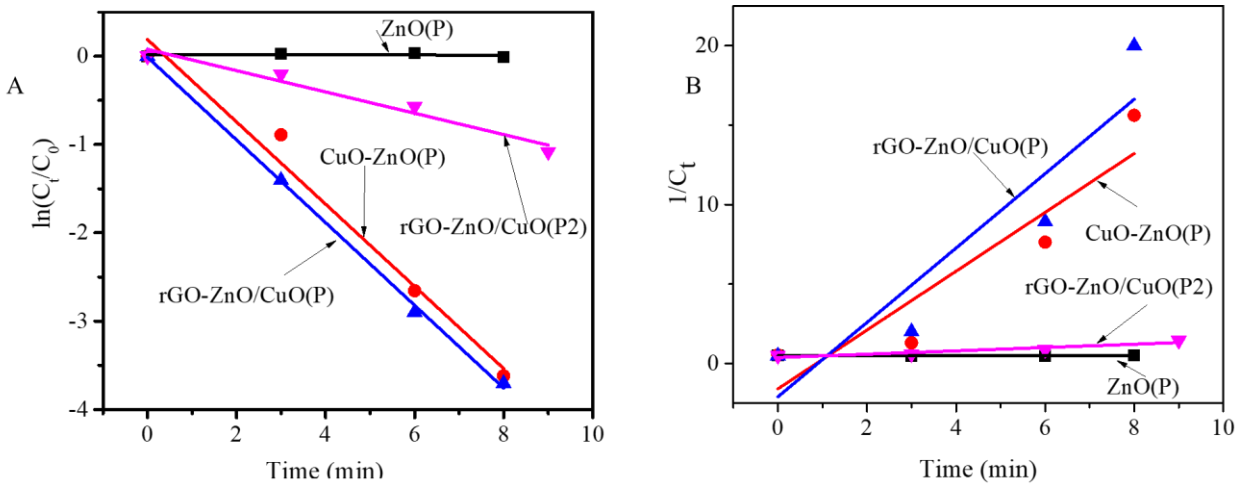

Figure 45. Kinetic analysis for 4-NP reduction: (A) plot of $\ln(C_t/C_0)$ *vs* t (pseudo 1st order fit), (B) plot of $1/C_t$ *vs* t (pseudo 2nd order fit).

4.3.1A. Mechanism of the catalytic reduction

There are different catalytic mechanisms proposed for the reduction reaction of nitroarene compounds into aminoarene. Generally, the mechanism of the 4-NP reduction reaction using

metal oxide catalysts involves major steps including (i) adsorption of BH_4^- and 4-NP to the catalyst surface, (ii) transfer of electrons from BH_4^- to the adsorbed 4-NP through catalysts (Kandula & Jeevanandam, 2016), (iii) transfer of protons from the BH_4^- and aqueous solution to the 4-NP completing reduction reaction (Zhao et al., 2019), and (iv) desorption steps (R. K. Sharma & Ghose, 2014; Shultz et al., 2020). Additionally, the nanocomposites possess a built-in electric field from the p-n heterojunction (between CuO and ZnO) that facilitate the adsorption process and transfer of charged species (Zelekew & Kuo, 2017). The proposed reaction mechanism with major steps for the conversion of 4NP into 4-AP by $NaBH_4$ along with metal oxide-based catalysts is given in Scheme 5 (Sun et al., 2019).

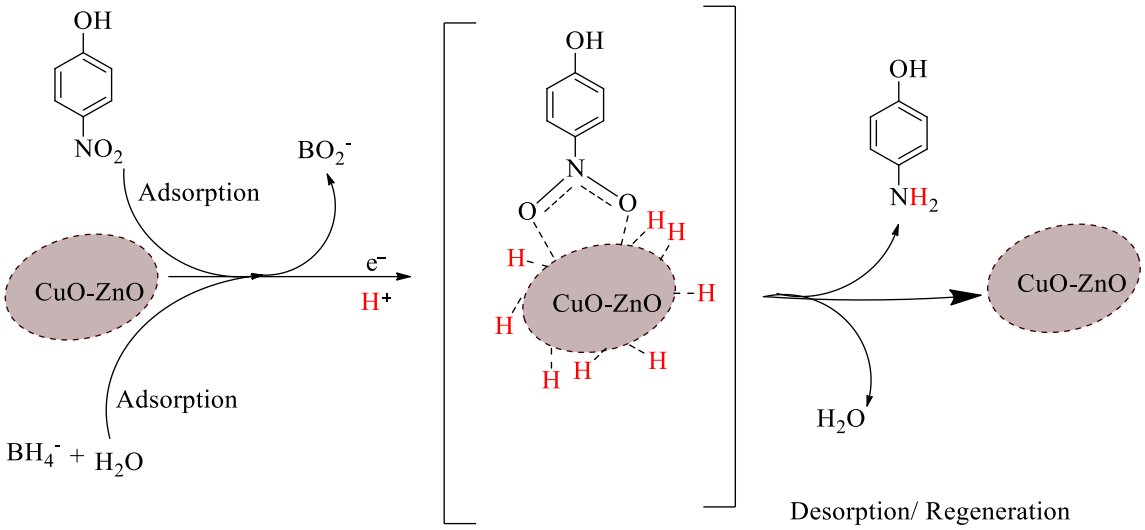

Scheme 5. Presumed catalytic reaction mechanism of 4-NP reduction using CuO-ZnO NCs as a catalyst.

4.3.2. Photocatalytic Degradation

The photocatalytic performance of the nanocomposites, CuO-ZnO(B)-20% and rGO-ZnO/CuO(P) was evaluated against degradation of MB under visible light irradiation and the result was compared with ZnO, i.e, ZnO(B) and ZnO(P). The efficiency and kinetics of degradation were analyzed. The photocatalytic activity of CuO-ZnO(B)-20% was tested against MB degradation and the corresponding results were given in Figure 46. The UV-Vis absorbance of MB showed a strong peak at 664 nm (Thatikayala & Min, 2021). In the presence of catalysts, irradiating MB aqueous solution with visible light resulted in decreasing absorbance with time

indicating photodegradation of the MB. Also, the study on how the CuO contents affect the activity of the prepared catalyst against MB was conducted by varying CuO contents. The results depicted in Figures 46A-C showed MB degradation efficiency of 24%, 65%, 82%, 75%, and 76% for samples having 0, 10, 20, 30, and 50% CuO wt%, respectively. More specifically, the CuO-ZnO(B)-20% showed the highest photocatalytic performance (82%) compared to the pristine ZnO NPs (24%) as shown in Figure 46.

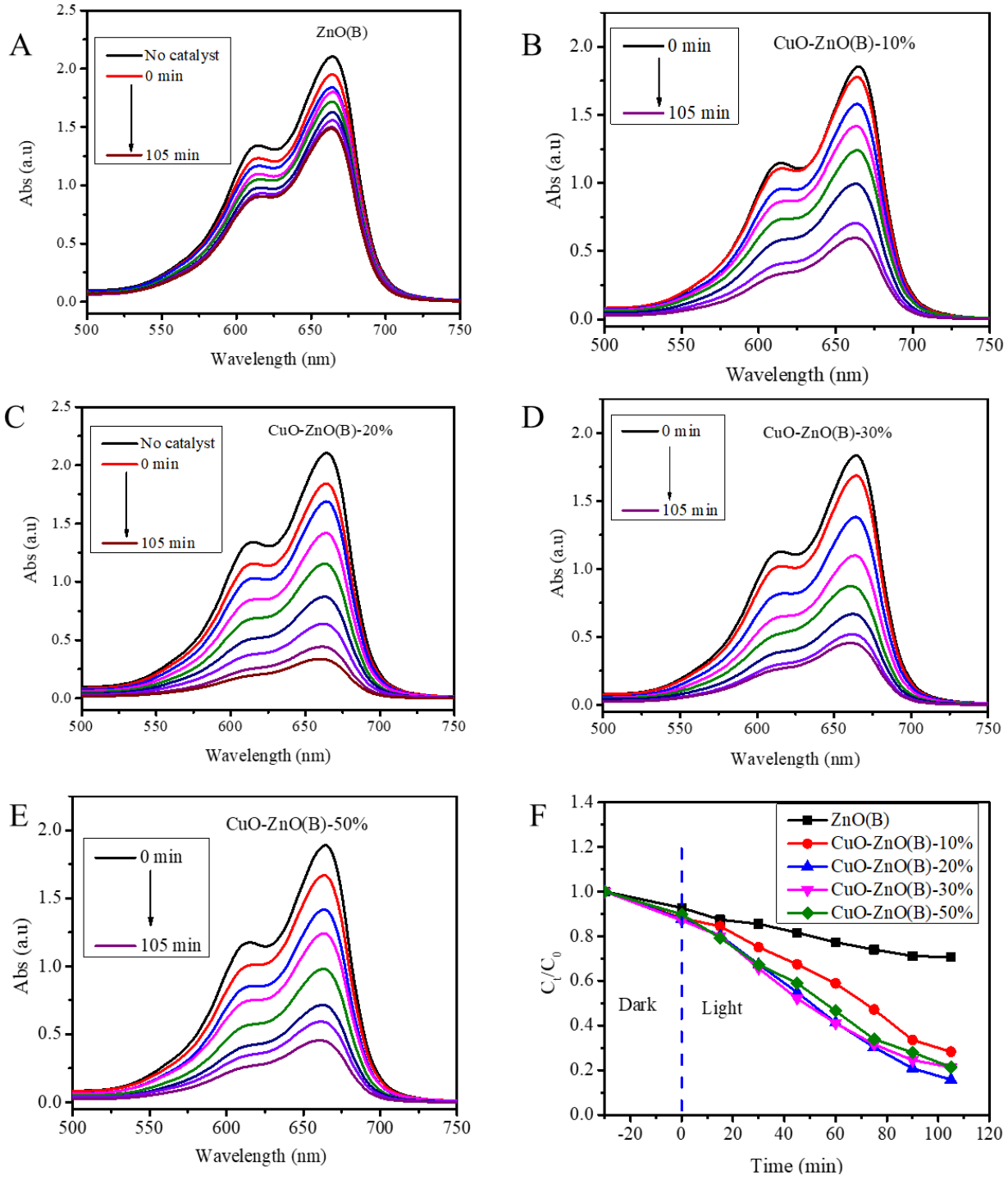

Figure 46. Photocatalytic removal of MB using CuO-ZnO with different CuO loading (wt%): (A) 0%, (B) 10%, (C) 20%, (D) 30%, (E) 50%; and (F) plots of (C_t/C_0) *vs* reaction time (min).

Based on the rate constant (k) calculated from the linear fitted plots (Figure 47 and Table 12), the data best fit the pseudo-first-order reaction. Thus, the calculated rate constants from the

pseudo-first-order kinetics were found to be 0.0027, 0.0112, 0.0170, 0.0139, and 0.0144 min^{-1} for 0%, 10%, 20%, 30%), and 50% loading of Cu^{2+} precursor, respectively (Figure 47A). While all CuO-ZnO samples showed higher performance than pristine ZnO NPs, CuO-ZnO NCs with 20 wt% CuO displayed the highest performance. This implies that there exists an optimum amount of CuO component in CuO-ZnO beyond which photocatalytic activity diminishes (Bharathi et al., 2019). As reported in previous studies, the decreased performance of CuO-ZnO with increased CuO content beyond the optimum value could be explained by the increased agglomeration of CuO that masks surface photoactive sites or enhance the rate of e^-/h^+ recombination (S. G. Babu et al., 2019). The enhanced performance could be the result of coupling a p-type CuO with an n-type ZnO. Specifically, the improved visible light absorption capacity of CuO-ZnO (from UV-Vis analysis), and the minimized rate of e^-/h^+ recombination (from PL and EIS analysis) could be the main reason for the enhancement (Pirhashemi et al., 2018).

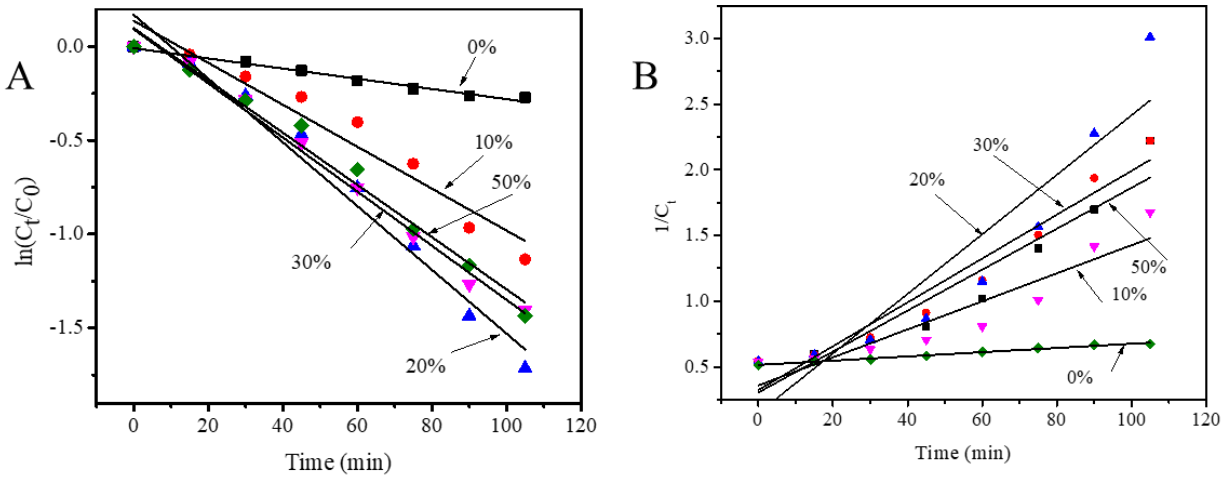

Figure 47. Kinetic analysis for MB degradation using ZnO(B) (0%) and CuO-ZnO NCs with different CuO loadings (10, 20, 30, 50%): (A) plot of $\ln(C_t/C_0)$ *vs* t (pseudo 1st order fit), (B) plot of $1/C_t$ *vs* t (pseudo 2nd order fit).

Table 12. Rate constants (k) from 1st and 2nd-order linear fits of MB degradation using ZnO(B) and CuO-ZnO NCs with different CuO loadings.

Catalyst	**1st order fit**		**2nd order fit**	
	k/(min^{-1})	R^2	k/(ppm^{-1} min^{-1})	R^2
ZnO(B)	0.00272	0.98173	0.00161	0.98436
CuO-ZnO(B)-10%	0.01118	0.93291	0.01068	0.84635
CuO-ZnO(B)-20%	0.017	0.96753	0.02269	0.84922
CuO-ZnO(B)-30%	0.01443	0.98798	0.0167	0.93583
CuO-ZnO(B)-50%	0.01392	0.9781	0.01559	0.89341

Table 13 compares the activities of this work to the earlier reports using ZnO-based NCs against MB degradation under different experimental conditions. Despite the different experimental conditions, the CuO-ZnO NCs obtained by using VSB exhibited superior photocatalytic performance compared to the previously reported literature values based on their ratio constants (Table 6). It degraded 82 % of the initial MB amount within 105 min with a rate constant of 0.017 min^{-1} or ratio constant of 0.85 $min^{-1}g^{-1}$ (ratio of k to the mass of catalyst).

Table 13. Comparison of the CuO-ZnO photocatalyst synthesized using VSB with previously reported ZnO-based NCs for photocatalytic degradation of MB.

Catalyst	Experimental conditions			Performance		Ref.
	Amount catalyst (mg)	Concentration of MB	Light	Rate const., k (min^{-1})	Ratio const., K ($min^{-1}g^{-1}$)	
CuO-ZnO	25	10^{-3} M	Vis	0.0235	0. 94	(Ullah et al., 2021)
Cr_2O_3/ZnO	25	10 ppm (125 mL)	Vis	0.015	0.6	(Zelekew et al., 2021)
ZnO/CuO	40	20 ppm	Vis	0.022.3	0.56	(Renuka et al., 2017)
CuO-ZnO	50	15 ppm (100 mL)	UV	0.01948	0.39	(Mageshwari et al., 2015)
CuO-ZnO	20	20 ppm	Vis	0.017	0.85	This work

Following the same procedure as that of CuO-ZnO(B)-20%, the photocatalytic performance of rGO-ZnO/CuO(P) was also analyzed and the corresponding results were given in Figure 48. In addition, the performance of ZnO(P), CuO-ZnO(P), rGO-ZnO/CuO(P), and rGO-ZnO/CuO(P2) obtained using PEG were also analyzed and the results were compared with that of the rGO-ZnO/CuO(P). According to the result, ZnO(P), CuO-ZnO(P), rGO-ZnO/CuO(P), and rGO-ZnO/CuO(P2) degraded about 37%, 80 %, 90 %, and 86% of the initial MB concentration within 105 min, respectively as depicted in Figures 48A-D.

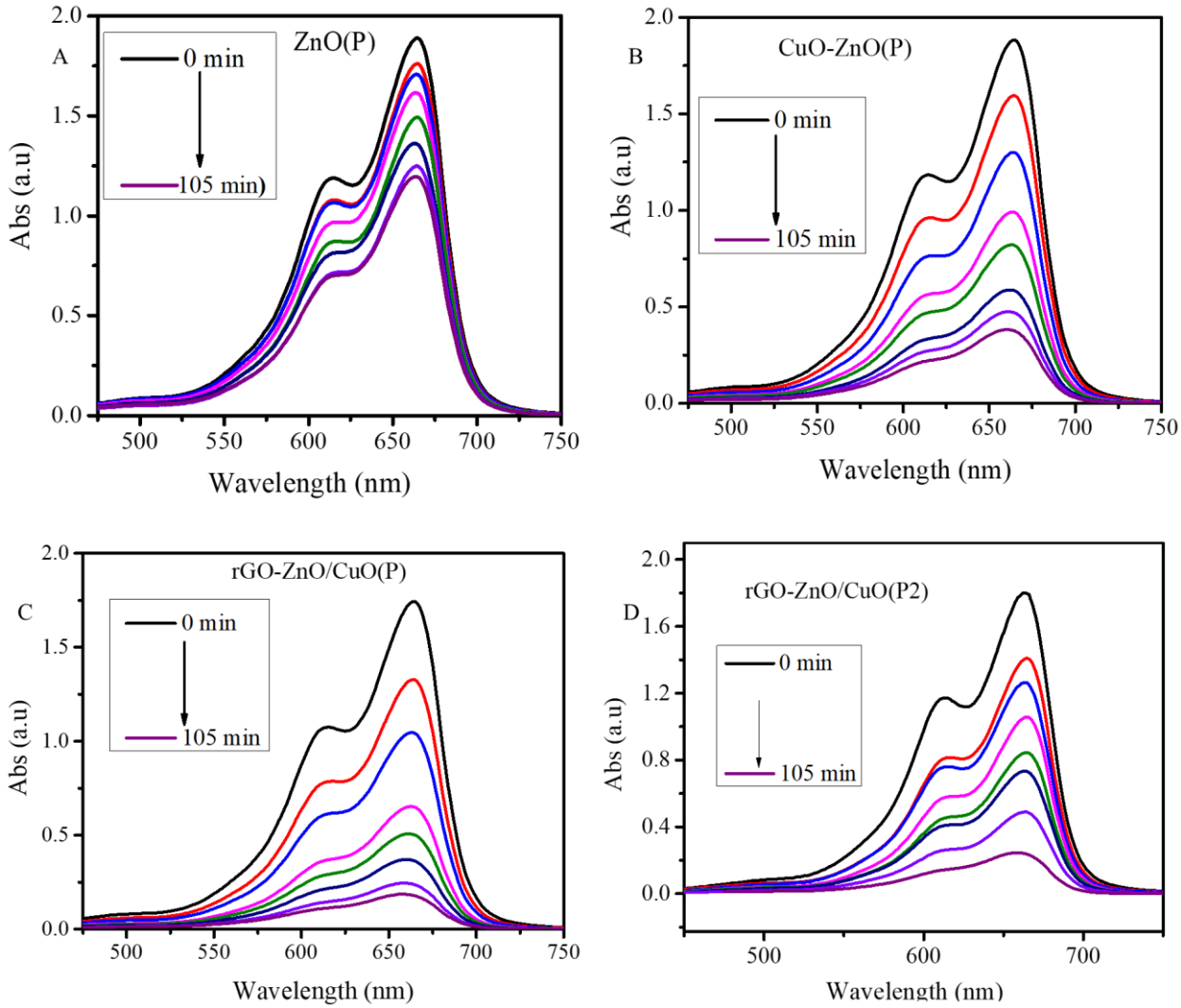

Figure 48. Photocatalytic degradation of MB using catalysts: (A) ZnO(P), (B) CuO-ZnO(P), (C) rGO-ZnO/CuO(P), and (D) rGO-ZnO/CuO(P2).

The kinetics of the degradation reaction was displayed in Figure 49. The rate constant (k) was calculated from the pseudo-first-order equation linear fitted plots of $\ln(C_t/C_o)$ *vs* time (Figure 49B), Table 14**)** and found to be 0.0045 min^{-1}, 0.0158 min^{-1}, and 0.0221 min^{-1}, 0.01687 min^{-1} for ZnO(P), CuO-ZnO(P), rGO-ZnO/CuO(P), and rGO-ZnO/CuO(P2), respectively. This enhancement in the photocatalytic performance compared to pristine ZnO signifies that the introduction of CuO and rGO improved the visible light absorption and suppressed the rate of recombination that have a significant effect on the performance of the catalyst (Pirhashemi et al., 2018). The result from the optical studies supported the improved performance of the NCs.

Particularly, the weaker PL intensity of the composite than pristine ZnO suggests the enhanced separation of the excitons (Fang et al., 2018; Shaker-Agjekandy & Habibi-Yangjeh, 2016). In other words, a higher charge separation assists the migration of excitons to the surface of the catalyst to react with the adsorbed species, leading to the higher PC activities of the composite compared to the pristine ZnO or ZnO(P) (Fang et al., 2018).

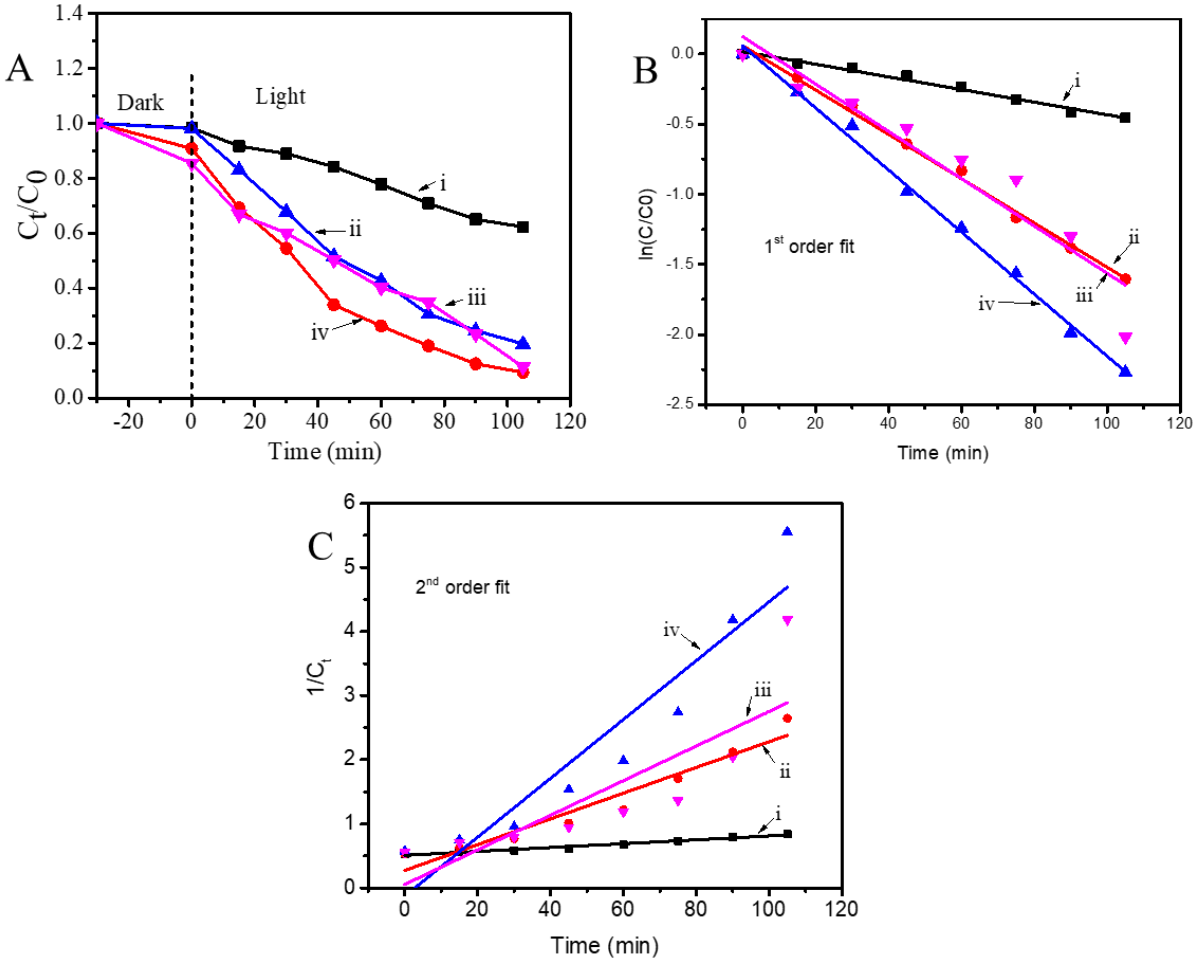

Figure 49. Kinetic analysis for MB degradation using (i) ZnO(P), (ii) CuO-ZnO(P), (iii) rGO-ZnO/CuO(P2) and (iv) rGO-ZnO/CuO(P). (A) plot of C_t/C_0 *vs* t, (B) plot of $\ln(C_t/C_0)$ *vs* t (pseudo 1st order fit), and (C) plot of $1/C_t$ *vs* t (pseudo 2nd order fit).

Table 14. Rate constants (k) from 1st and 2nd-order linear fits of MB degradation using ZnO(P) and CuO-ZnO(P) and rGO-ZnO/CuO(P).

Catalysts	**1st order fit**		**2nd order fit**	
	k/(min^{-1})	R^2	k/(ppm^{-1} min^{-1})	R^2
ZnO(P)	0.0045	0.983	0.00302	0.968
CuO-ZnO(P)	0.0158	0.994	0.02007	0.927
rGO-ZnO/CuO(P)	0.02213	0.995	0.0459	0.879
rGO-ZnO/CuO(P2)	0.01687	0.896	0.02699	0.642

Comparing the efficiency of the MB photocatalytic degradation with the nanomaterials synthesized using VSB and PEG, the rGO-based rGO-ZnO/CuO NCs obtained using PEG showed an enhanced performance (90%). The CuO-ZnO NCs in both cases have comparable performance with 82% for CuO-ZnO(B)-20% and 80% for CuO-ZnO(P).

4.3.2A. Mechanism of photocatalysis

Generally, the reaction mechanism of semiconductor-based photocatalyst involves light absorption, exciton (e^-/h^+) generation, and exciton separation and migration to the surface-active sites/trap states. At the active sites, the e^-/h^+ reacts (photoreduction and photooxidation reactions) with the adsorbed species (O_2, OH^-/H_2O, pollutant RH, etc.) generating highly reactive species depending on the potential of charge carriers and redox potentials of the adsorbed species (Nosaka & Nosaka, 2017; Ong et al., 2018). Among the active species formed by the reaction with e^-/h^+ are pollutant radical ($R^\bullet$) and reactive oxygen species (ROS) like hydroxyl radicals ($^\bullet OH$), superoxide anion radicals ($O_2^{\bullet-}$), singlet oxygen species ($^1O_2$), and peroxide molecules (H_2O_2). These species have a high tendency of oxidizing or degrading organic pollutants into less toxic substances or mineralizing them into CO_2, H_2O and others. Finally, regeneration of the photocatalyst surface follows.

In the case of CuO-ZnO(B)-20%, the light of appropriate energy illumination generates exciton where e^- accumulate in the conduction band (CB) and h^+ in the valance band (VB). Coupled CuO with ZnO semiconductor provides the band alignment in which the electrons in the CB of

CuO are pushed to the relatively less negative CB of ZnO. Thus, the h^+ in the VB oxidizes H_2O/HO^- (or organic pollutant RH) resulting in $HO^\bullet$ (or $R^\bullet$) depending on the potential of the hole in the VB (Scheme 6). And also, the e^- in the CB will be trapped by the dissolved oxygen and produce ROS that finally degrades the pollutant (Scheme 6) (Thatikayala & Min, 2021). In this regard, the degradation of MB in the presence of CuO-ZnO(B)-20% under visible light irradiation could end up producing H_2O, CO_2, and other inorganic ions like NO_3^-, SO_4^{2-}, and Cl^- as shown in Scheme 6 (F. Huang et al., 2010).

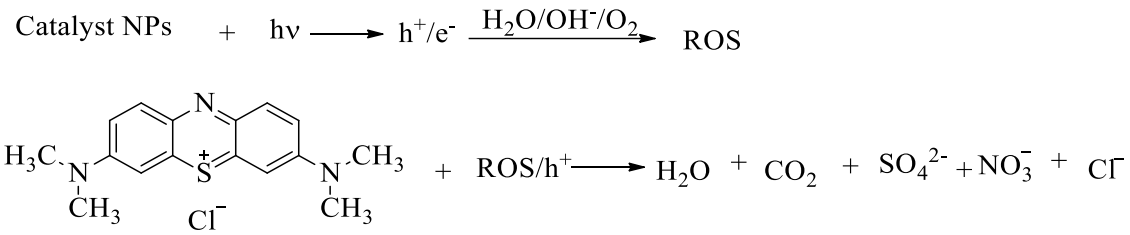

Scheme 6. Possible mechanism of NPs-based photocatalytic degradation of MB.

To investigate the main active species involved in photocatalytic degradation of MB using rGO-ZnO/CuO NCs, the trapping experiments were conducted. In the experiment, the scavengers used were ethylenediaminetetraacetic acid disodium (EDTA-2Na), isopropanol (IPA), and $AgNO_3$ to scavenge photogenerated holes (h^+), hydroxyl radicals ($^\bullet OH$), and superoxide radicals ($^\bullet O_2^-$), respectively (Fang et al., 2018). The result showed decreased efficiency of MB photocatalytic degradation in the presence of scavengers compared to without scavengers indicating that h^+, $^\bullet OH$, and $^\bullet O_2^-$ are the active species involved. The results of the experiment were illustrated in Figure 50.

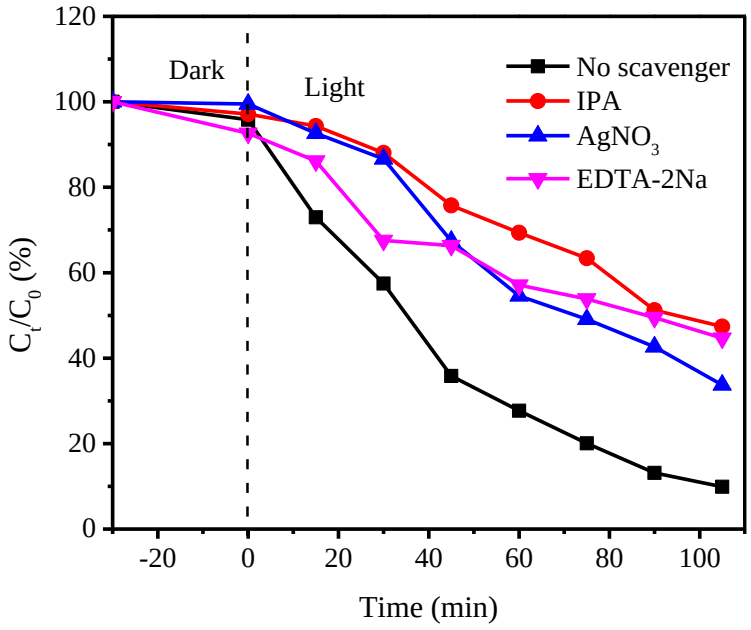

Figure 50. Effect of scavengers (IPA, $AgNO_3$, EDTA-2Na) on the photocatalytic degradation of MB using rGO-ZnO/CuO NCs.

The generation and reaction of each of these species (h^+, $^{\bullet}OH$, and $^{\bullet}O_2^-$) depend on the band-edge potentials and the redox potential of the adsorbed reactants. Illumination of rGO-ZnO/CuO with visible light generates e^-/h^+ (electrons residing in the CB and holes in the VB) leading to the generation of ROS. (i) The photogenerated e^- in the CB reacts with the adsorbed O_2 producing $^{\bullet}O_2^-$ provided that the CB potentials are more negative than the potential of $O_2/^{\bullet}O_2^-$ (-0.16V vs NHE) (Eqn. 1) (Hayyan et al., 2016). The $^{\bullet}O_2^-$ further reacts and forms other reactive oxygen species (Eqn.9,10, and 11). (ii) The $^{\bullet}OH$ could be generated as shown in the Equations (Eqn.4, 5, 11 and 14). The $^{\bullet}OH$ possesses strong oxidizing power to degrade MB (Eqn. 16). (iii) The photogenerated holes in the VB or trap states react with the adsorbed species (OH^-, H_2O, or MB) and generate reactive radicals that further react with other species and degrade the pollutants (Eqn.4-6). Oxidation of the adsorbed species (H_2O, OH^-) to generate $^{\bullet}OH$ occurs when the VB edge potentials are more positive than the potential of $OH^-/^{\bullet}OH$ (1.9V vs NHE) and $H_2O/^{\bullet}OH + H^+$ (2.73 V vs NHE) (Jenny et al., 2014). The reaction and formation mechanism of $^{\bullet}O_2^-$ and $^{\bullet}OH$ with other species were given previously in Section 2.2.1 (Eqn. 1-17).

$$O_2 + e^- \rightarrow {}^{\bullet}O_2^- \qquad (1)$$

$$^{\bullet}O_2^- + H_2O \rightarrow HOO^{\bullet} + OH^- \quad (9)$$

$$^{\bullet}O_2^- + H^+ \rightarrow HOO^{\bullet} \quad (10)$$

$$^{\bullet}O_2^- + H_2O_2 \rightarrow {}^{\bullet}OH + OH^- + O_2 \quad (11)$$

$$HOO^{\bullet} + H_2O \rightarrow {}^{\bullet}OH + H_2O_2 \quad (14)$$

$$OH^- + h^+ \rightarrow {}^{\bullet}OH \quad (4)$$

$$H_2O + h^+ \rightarrow {}^{\bullet}OH + H^+ \quad (5)$$

$$RH + h^+ \rightarrow R^{\bullet} + H^+ \quad (6)$$

$$RH + {}^{\bullet}OH \rightarrow R^{\bullet} + H_2O \quad (16)$$

$$R^{\bullet} \rightarrow \text{intermediate/final degraded product} \quad (17)$$

$$\therefore RH \xrightarrow{\text{catalyst + hv}} \text{intermediates} \rightarrow CO_2 + H_2O + \text{inorganic products}$$

Where RH stands for MB dye.

4.3.3. Antibacterial Activity Test

The *in vitro* antibacterial activities of each of the synthesized nanomaterials using CAL extract: CuO(L-10), using VSB extract: ZnO(B) and CuO-ZnO(B)-20%, and using PEG-200: ZnO(P), CuO-ZnO(P), and rGO-ZnO/CuO(P) were tested against *E. coli*, *S. aureus,* and *P. aeruginosa,* and *S. pyogenes* pathogens at concentrations of 37.5, 75, 150, and 300 μg/mL. The mean diameter (mm) of the growth inhibition zone (by taking two replicate measurements) were presented in Tables 15 and 16.

As can be observed from Tables 15 and 16, the nanoparticles exhibited different activities against the test bacterial strains. All nanomaterials, i.e., CuO(L-10), ZnO(B), CuO-ZnO(B)-20%, ZnO(P), CuO-ZnO(P), and rGO-ZnO/CuO(P), exhibited growth inhibition (> 7 mm inhibition zone diameter) against *E. coli*, *P. aeruginosa*, and *S. pyogenes* at all tested concentrations indicating their potential antibacterial activity when compared to the positive control standard drug (ceftriaxone). However, only CuO-ZnO(P) and CuO(L-10) showed

antibacterial activities against *S. aureus*, but the rest nanomaterials indicated no sign of activity (< 7 mm inhibition zone width) against the bacterium *S. aureus* at all concentrations.

The highest mean inhibitory value of 20.5±0.5 mm was exhibited by CuO(L-10), followed by CuO-ZnO(B)-20% (18.5±0.5 mm), ZnO(P) (16.75±0.25 mm), and ZnO(B) (15.5±0.5 mm) against *E. coli* at a concentration of 37.5 μg/mL. CuO-ZnO(P) and rGO-ZnO/CuO showed moderate inhibitory effects against *E. coli* (13.75±0.75 and 10±1, mm, respectively) at a concentration of 37.5 μg/mL. The zone of inhibition values was studied using different concentrations of nanomaterials as shown in Table 15 and 16. With the increase in concentrations, all materials exhibited enhanced activity against *E. coli*, *P. aeruginosa*, and *S. pyogenes.* The bacteria *P. aeruginosa* and *S. pyogenes* were found to be more susceptible to the nanomaterials at all concentrations than *E. coli*. At low concentration (37.5 μg/mL), the highest mean inhibitory was exhibited by CuO(L-10) (22±0 mm) and ZnO(P) (26.5±0.5 mm) against *P. aeruginosa* and *S. pyogenes*, respectively. Overall, the prepared materials showed growth inhibitory activity against *E. coli*, *P. aeruginosa*, and *S. pyogenes* at all concentrations in good comparison with that of the standard, ceftriaxone (29.0±0, 35.3±1.5, and 33±2.6 mm, respectively).

The result of the present finding generally indicates that among the prepared materials CuO(L-10) and CuO-ZnO(P) displayed growth inhibition against all bacterial strains tested at all concentrations. Also, all nanomaterials showed good antibacterial activity against the Gram-negative bacterial strains (*E. coli* and *P. aeruginosa*) and Gram-positive bacterium (*S. pyogenes*) at all tested concentrations. Whereas ZnO(B), CuO-ZnO(B)-20%, ZnO(P), and rGO-ZnO/CuO(P) nanomaterials have no shown growth inhibition activity against the Gram-positive bacterium (*S. aureus*) at all concentrations. The difference in the activity against these two types of bacteria could be attributed to the structural and compositional differences in the cell membrane (Slavin et al., 2017). Gram-positive bacteria have thicker peptidoglycan membranes compared to Gram-negative bacteria. Also, Gram-negative bacteria are coated with lipopolysaccharide molecules, which carry a negative charge. These negatively charged molecules have a higher affinity for the positive ions that most of the NPs release, leading to a buildup and increased uptake of ions, which then cause intracellular damage.

Table 15. Antibacterial activity inhibition zone (mean ± SD, in mm) of prepared nanomaterials against standard *E. coli*, *S. aureus*, and *P. aeruginosa* bacterial strains. (NA = Not active).

B. strains	**Sample**	**Concentrations (µg/mL)**			
		37.5	75	150	300
E. coli	CuO(L-10)	20.5±0.5	22.5±0.5	23.5±1	24±0
	ZnO(B)	15.5±0.5	17.75±0.25	19.5±0.5	20.5±0.5
	CuO-ZnO(B)-20%	18.5±0.5	19.5±0.5	21±0	22.5±0.5
	ZnO(P)	16.75±0.25	19.5±0.5	21.25±0.25	23±0
	CuO-ZnO(P)	13.75±0.75	15.5±0.5	17.25±0.25	21.5±0.5
	rGO-ZnO/CuO(P)	10±1	11±1	13.5±1.5	14.5±1.5
	Ceftriaxone	29.0±0			
S. aureus	CuO(L-10)	10±0.5	11.5±0.5	12.25±0.75	13±0.25
	ZnO(B)	NA	NA	NA	NA
	CuO-ZnO(B)-20%	NA	NA	NA	NA
	ZnO(P)	NA	NA	NA	NA
	CuO-ZnO(P)	11±0.5	11±0.25	12.25±0.75	12.75±0.75
	rGO-ZnO/CuO(P)	NA	NA	NA	NA
	Ceftriaxone	15±0.6			
P. aeruginosa	CuO(L-10)	22±0	25.5±0.5	27±0	28.5±0.5
	ZnO(B)	16.75±0.75	21±1	22.5±0.5	27±0
	CuO-ZnO(B)-20%	18±0	21.5±0.5	25.5±0.5	26.5±0.5
	ZnO(P)	11.5±0.5	21.5±0.5	23.5±0.5	25.5±0.5
	CuO-ZnO(P)	18.5±0.5	21.5±0.5	23.75±0.25	25.5±0.5
	rGO-ZnO/CuO(P)	10.5±1.5	12.75±1.25	13.75±1.75	15.5±1.5
	Ceftriaxone	35.3±1.5			

Table 16. Antibacterial activity inhibition zone (mean ± SD, in mm) of prepared nanomaterials against standard *S. pyogenes* bacterial strains.

B. strains	**Sample**	**Concentrations (µg/mL)**			
		37.5	75	150	300
S. pyogenes	CuO(L-10)	24.75±0.25	27.5±0.5	29.5±0.5	30.25±1.25
	ZnO(B)	24±0	27.5±0.5	28.5±0.5	28.5±0.5
	CuO-ZnO(B)-20%	23.75±0.25	29.5±0.5	31±1	31.5±1.5
	ZnO(P)	26.5±0.5	27.5±0.5	28±0.5	28.5±0.5
	CuO-ZnO(P)	24±1	27.5±0.5	28.5±0.5	29±1
	rGO-ZnO/CuO(P)	13.5±1.5	14±1	15.5±0.5	17±1
	Ceftriaxone	33±2.6			

The bar graph of the results for the 37.5 µg/mL concentration was shown in Figure 50. The Figure shows that all nanomaterials are active against *E. coli*, *P. aeruginosa*, and *S. pyogenes* with highest activity against *S. pyogenes*. Whereas only ZnO(B) and CuO-ZnO(P) nanomaterials have shown antibacterial activity against *S. aureus*. Among the tested nanomaterials, rGO-ZnO/CuO NCs showed the least performance against *E. coli*, *P. aeruginosa,* and *S. pyogenes* at 37.5 µg/mL concentration. The overall nanomaterials antibacterial activities evaluation indicated that CuO(L-10) and CuO-ZnO(P) are effective against the all the four bacterial strains. CuO-ZnO(B)-20% also showed effective performance against *E. coli*, *P. aeruginosa*, and *S. pyogenes* bacterial strains.

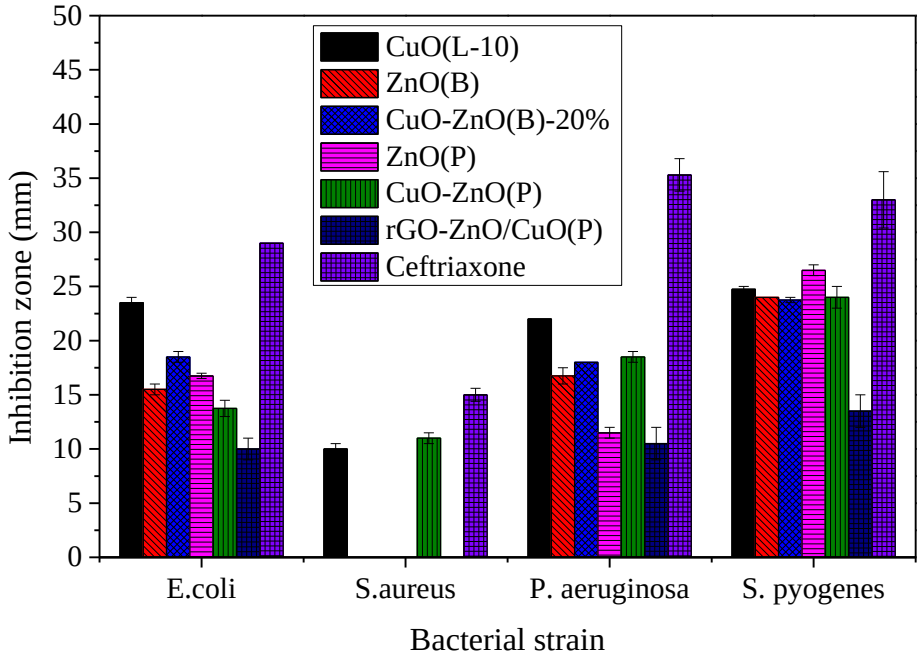

Figure 51. Inhibition zone of CuO(L-10), ZnO(B), CuO-ZnO(B)-20%, ZnO(P), CuO-ZnO(P), and rGO-ZnO/CuO(P) using 37.5 μg/mL concentration.

There are various mechanisms to explain the antibacterial activities of metal oxide nanomaterials. in the case of CuO(L-10), ZnO(B), CuO-ZnO(B)-20%, ZnO(P), CuO-ZnO(P), and rGO-ZnO/CuO NCs, the plausible mechanisms could involve direct physical interaction, the release of metal ions, generation of secondary products, and others (R. Dadi et al., 2019; Slavin et al., 2017). The direct interaction of the bacterial cells with the sharp edges of the nanomaterials causes physical damage to the bacterial cell wall by NPs adsorption and is often followed by penetration into the cell resulting in the death of the bacteria (Revathi & Karthik, 2018). In addition, due to the electrochemical potential in the solution, metal oxide NPs (CuO, ZnO) release Cu^{2+} and Zn^{2+} ions that diffuse into the bacterial cells and interact with the negatively charged cells electrostatically disrupting the membrane and cell toxicity. Both Gram-positive and -negative bacteria have a negatively charged cell wall. In addition, the interaction of the NPs with bacterial membranes may lead to the generation of ROS which can cause damage to secondary membranes, hinder the function of proteins, and destroy deoxyribonucleic acid (DNA) (R. Dadi et al., 2019). Photographic images of the zone of inhibition of some samples were given in Figure 52.

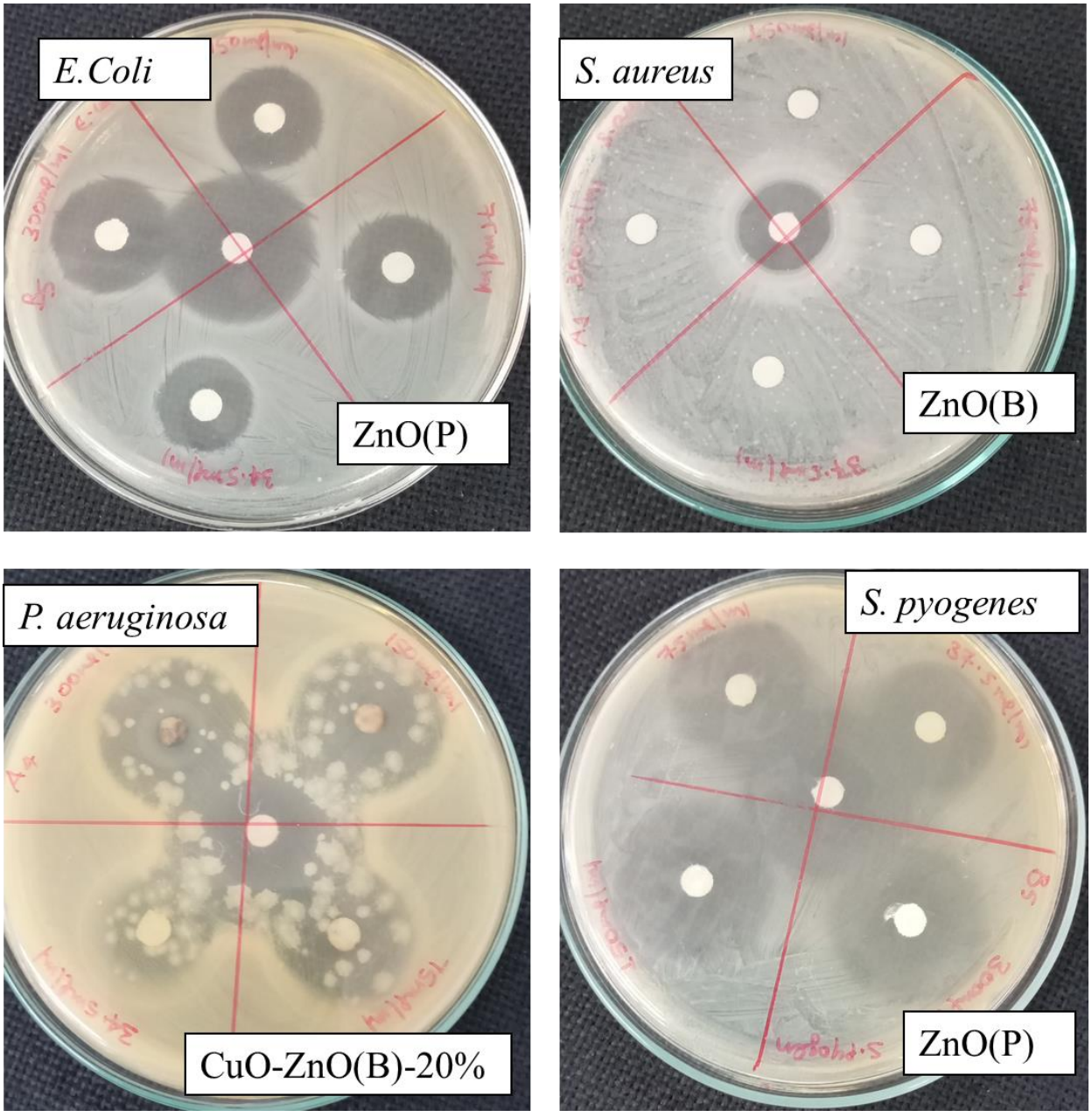

Figure 52. Photographic images of the growth inhibition zone against *E. coli, S. aureus, P. aeruginosa,* and *S. pyogenes* bacterial strains using ZnO(P), ZnO(B), CuO-ZnO(B)-20%, and ZnO(P) nanomaterials, respectively.

4.3.4. Reusability Test

In the process of reusing the catalysts, the used catalysts were separated by centrifugation, washed with DW and ethanol three times each, dried at 60 ºC overnight, and then reused in the next run (Mathalai Sundaram et al., 2019). Stability is one of the important factors to consider when it comes to the reusability of the catalyst. To this end, the recyclability of the synthesized catalysts was evaluated. In this case, the performance of CuO-ZnO(B)-20% and rGO-ZnO/CuO(P) were tested against photocatalytic degradation of MB (Figure 53A) and the catalytic reduction of 4-NP (Figure 53B). In addition, the recyclability test for the CuO(L-10) for the 4-NP catalytic reduction was evaluated as shown in Figure 53B. As shown in Figure 53A, both CuO-ZnO(B)-20% and rGO-ZnO/CuO(P) have shown fairly good stability during the four reuse runs; i.e 70 and 84 percent degradation of the initial MB concentration in the fourth run for CuO-ZnO(B)-20% and rGO-ZnO/CuO(P), respectively. However, in the fourth cycle for CuO-ZnO(B)-20%, there was a relatively sudden drop in efficiency, which could be attributed to photocorrosion, or adsorption of dye molecules onto the catalyst surface, decreasing the active surface and light absorption (X. Lei et al., 2019; Mathalai Sundaram et al., 2019; Thatikayala & Min, 2021). In this respect, CuO-ZnO NCs (CuO-ZnO(B)-20%) are a stable and recyclable photocatalyst for the degradation of MB under visible light illumination. Similarly, the catalyst recyclability against the reduction of 4-NP was also evaluated using the same recovery procedure. The efficiency for each run was shown in Figure 53B. It can be seen that CuO-ZnO(B)-20% and rGO-ZnO/CuO(P) showed a remarkable performance up to four cycles with 96.3 and 98% reduction efficiency in the 4^{th} round of the reuse run, respectively. Accordingly, the little change in the efficiency of the catalyst after four cycles suggests CuO-ZnO NCs are promising catalysts for treating organic pollutants in water. On the other hand, CuO(L-10) reduction efficiencies were found to be 100% (1^{st}), 70.9% (2^{nd}), 53.5% (3rd), and 36% (4^{th}) cycles in 12 min after the reaction was started in each step (Figure 53B). The result indicated that CuO(L-10) has poor recyclability against the 4-NP reduction. The significant decrease in performance with reused catalyst could be due to the high rate of corrosion resulting in Cu^{+2} ions and the passivation of the active sites by the adsorbed species from the previous cycle.

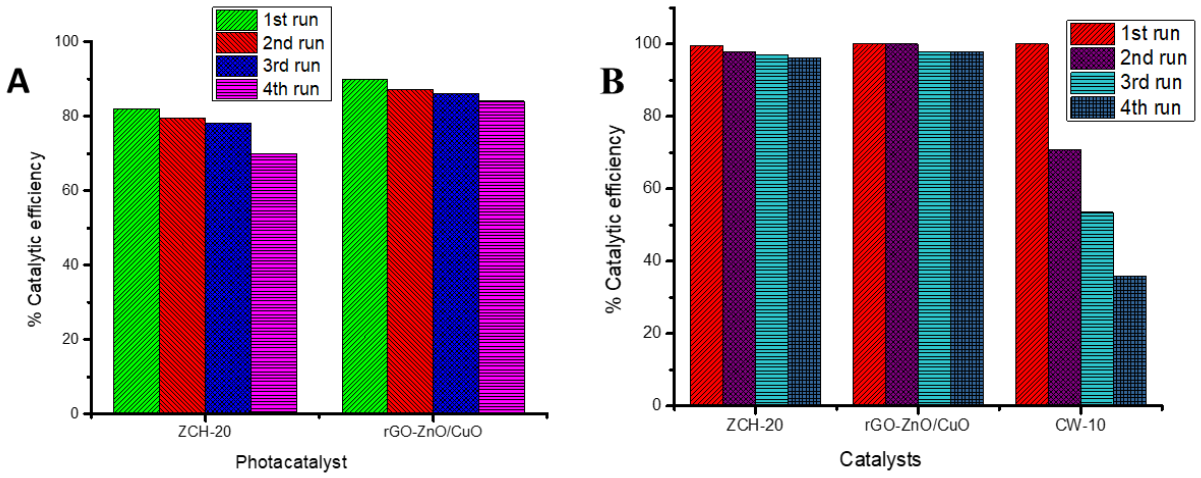

Figure 53. Comparison of the efficiencies for four successive cycles of (A) MB photodegradation, (B) 4-NP reduction to 4-aminophenol.

The stability of the CuO-ZnO NCs (CuO-ZnO(B)-20%) catalyst was investigated by analyzing its XRD patterns before and after it had been used for 4 runs as shown in Figure 54. According to the XRD pattern after reusability, the crystallinity of the sample does not show appreciable change after 4 cycles of catalytic reduction run indicating remarkable stability. Before the reaction, the diffractogram exhibits characteristic peaks of 2 phases only (ZnO card no. 00-036-1451, and CuO card no. 00-048-1548). However, after 4 cycle catalytic reduction runs, an additional peak at $2\theta=43.3^{o}$ which could be attributed to the formation of Cu^{0} phase (Cu card no. 00-004-0836) from the reduction of CuO due to the presence of $NaBH_4$ (Kassem et al., 2021).

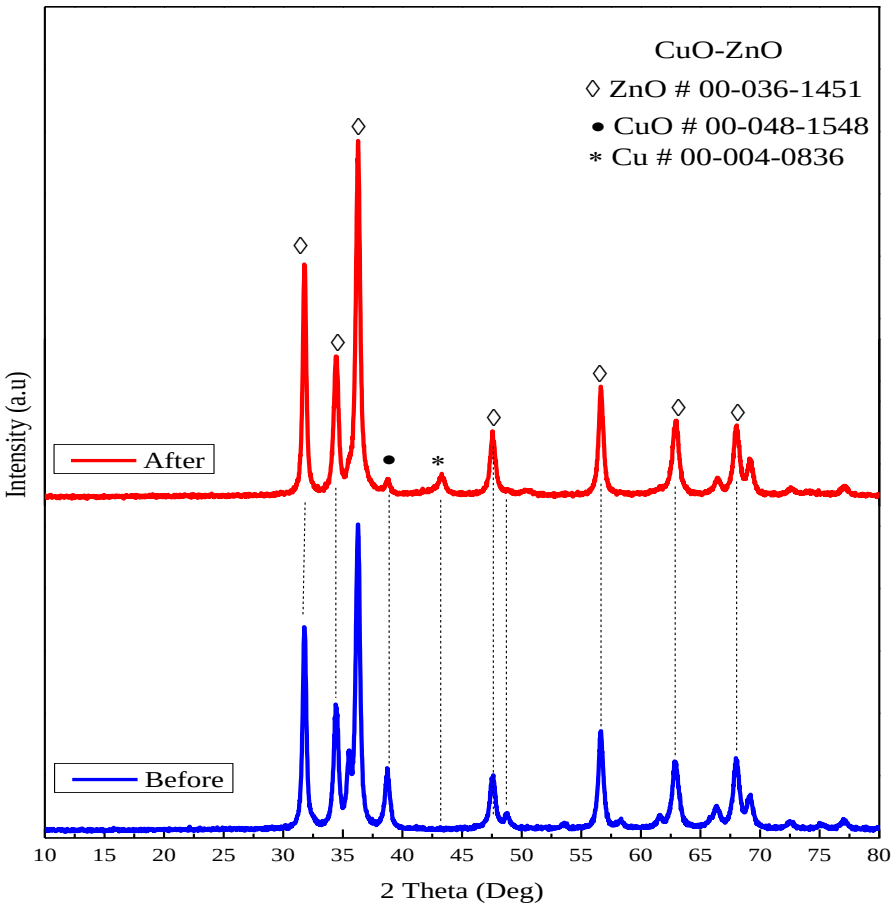

Figure 54. XRD patterns of CuO-ZnO(B)-20% before catalysis and after catalytic reduction of 4-NP for four runs.

CHAPTER FIVE

5. CONCLUSION AND RECOMMENDATIONS

In this study, CuO NPs, ZnO NPs, CuO-ZnO NCs, rGO-ZnO/CuO NCs, and rGO were successfully synthesized by MW-assisted method using (i) CAL extract: CuO(L-10), (ii) VSB extract:ZnO(B), CuO-ZnO(B), (iii) PEG-200: ZnO(P), CuO-ZnO(P), rGO-ZnO/CuO(P), rGO-ZnO/CuO(P2), and (iv) ascorbic acid: rGO. XRD, UV-Vis, FT-IR, PL, SEM, EIS, and other methods were used to explore the crystallinity, optical characteristics, morphology, composition, and other features of the synthesized nanomaterials. The results indicated that spherical-shaped CuO(L-10), plate-like CuO-ZnO(B)-20%, and rod-like rGO-ZnO/CuO(P) was formed. The prepared materials have shown a remarkable performance against the catalytic reduction of 4-NP with ratio rate constants of 75.8, 5.92, and 11.7 $min^{-1}g^{-1}$ for CuO(L-10), CuO-ZnO(B)-20%, and rGO-ZnO/CuO NCs against the 4-NP reduction, respectively. Also, MB photocatalytic degradation efficiency of 80% for CuO-ZnO(B)-20% and 90% rGO-ZnO/CuO(P) was achieved. Further, the inhibition zone exhibited by all nanomaterials is in good comparison with that of the standard, ceftriaxone against the Gram-negative bacterial strains (*E. coli* and *P. aeruginosa*) and Gram-positive bacterium (*S. pyogenes*). In addition, the nanocomposites showed better recyclability against both 4-NP reduction and MB photocatalytic degradation. Therefore, the nanomaterials obtained using PEG and extracts of CAL and VSB could be the potential candidate for the remediation of polluted water and bacterial disinfection.

The following points are recommended for future work:

- Optimization of operational parameters such as the pH of the solutions, calcination temperature and time, microwave irradiation time and power, precursors type and concentration, and copper precursors percentage (< 10% and >50%) used during synthesis.
- Test for the performance of the different CuO-ZnO NCs synthesized using CAL and VSB for the reduction of 4-NP.
- Further characterization of the selected composites by Raman spectroscopy

- Test for the effects of scavengers to determine the dominant reactive species in the degradation process and describe the mechanism of the reaction.
- Test for simultaneous degradation of mixed dyes, and conduct the degradation process considering real industrial effluents.
- Further investigation for determination of the minimum inhibitory concentration of each sample against each bacterial strain.

6. REFERENCES

Ademe, A. S. (2014). 'Source and Determinants of Water Pollution in Ethiopia: Distributed Lag Modeling Approach.' *Intellectual Property Rights: Open Access*, *2*(2).

Adil, S. F. et al. (2015). 'Biogenic synthesis of metallic nanoparticles and prospects toward green chemistry.' *Dalton Transactions*, *44*(21), 9709–9717.

Adyani, S. H., & Soleimani, E. (2019). 'Green synthesis of Ag/Fe_3O_4/RGO nanocomposites by Punica Granatum peel extract: Catalytic activity for reduction of organic pollutants.' *International Journal of Hydrogen Energy*, *44*(5), 2711–2730.

Agarwal, S. et al. (2019). 'Morphology-dependent structural and optical properties of ZnO nanostructures.' *Applied Physics A: Materials Science and Processing*, *125*(8), 553.

Ahamed, M. et al. (2014). 'Synthesis, characterization, and antimicrobial activity of copper oxide nanoparticles.' *Journal of Nanomaterials*, *2014*(January), 17.

Ahmadi, R. et al. (2021). 'Evaluation of antibacterial behavior of in situ grown CuO-GO nanocomposites.' *Materials Today Communications*, *28*(July), 102642.

Ahmed, S. et al. (2017). 'A review on biogenic synthesis of ZnO nanoparticles using plant extracts and microbes: A prospect towards green chemistry.' *Journal of Photochemistry and Photobiology B: Biology*, *166*, 272–284.

Ajmal, A. et al. (2014). 'Principles and mechanisms of photocatalytic dye degradation on TiO 2 based photocatalysts: A comparative overview.' *RSC Advances*, *4*(70), 37003–37026.

Akir, S. et al. (2016). 'Eco-friendly synthesis of ZnO nanoparticles with different morphologies and their visible light photocatalytic performance for the degradation of Rhodamine B.' *Ceramics International*, *42*(8), 10259–10265.

Akpan, U. G., & Hameed, B. H. (2009). 'Parameters affecting the photocatalytic degradation of dyes using TiO_2-based photocatalysts: A review.' *Journal of Hazardous Materials*, *170*(2–3), 520–529.

Alam, S. N. et al. (2017). 'Synthesis of Graphene Oxide (GO) by Modified Hummers Method and Its Thermal Reduction to Obtain Reduced Graphene Oxide (rGO).' *Graphene*, *06*(01), 1–18.

Ali, K. et al. (2015). 'Microwave accelerated green synthesis of stable silver nanoparticles with Eucalyptus globulus leaf extract and their antibacterial and antibiofilm activity on clinical isolates.' *PLoS ONE*, *10*(7), 1–20.

Ali, S. G. et al. (2021). 'Butea monosperma seed extract mediated biosynthesis of ZnO NPs and their antibacterial, antibiofilm and anti-quorum sensing potentialities.' *Arabian Journal of Chemistry*, *14*(4), 103044.

Ambika, S., & Sundrarajan, M. (2015). 'Antibacterial behaviour of Vitex negundo extract assisted ZnO nanoparticles against pathogenic bacteria.' *Journal of Photochemistry and Photobiology B: Biology*, *146*, 52–57.

Amir Faiz, M. S. et al. (2020). 'Low cost and green approach in the reduction of graphene oxide (GO) using palm oil leaves extract for potential in industrial applications.' *Results in Physics*, *16*(January), 102954.

Annathurai, S. et al. (2019). 'Green Synthesis and Electrical Properties of p-CuO/n-ZnO Heterojunction Diodes.' *Journal of Inorganic and Organometallic Polymers and Materials*, *29*(2), 535–540.

Ansari, M. O. et al. (2015). 'Electrically conductive polyaniline sensitized defective-TiO2 for improved visible light photocatalytic and photoelectrochemical performance: A synergistic effect.' *New Journal of Chemistry*, *39*(11), 8381–8388.

Anwer, H. et al. (2019). 'Photocatalysts for degradation of dyes in industrial effluents: Opportunities and challenges.' *Nano Research*, *12*(5), 955–972.

Arellano-Cortaza, M. et al. (2021). 'pH dependent morphology and texture evolution of ZnO nanoparticles fabricated by microwave-assisted chemical synthesis and their photocatalytic dye degradation activities.' *Ceramics International*, *47*(19), 27469–27478.

Arias, F. A. et al. (2020). 'The adsorption of methylene blue on eco-friendly reduced graphene oxide.' *Nanomaterials*, *10*(4), 4–5.

Arsha Kusumam, T. V. et al. (2016). 'Morphology controlled synthesis and photocatalytic activity of zinc oxide nanostructures.' *Ceramics International*, *42*(3), 3769–3775.

Asadzadeh-Khaneghah, S., & Habibi-Yangjeh, A. (2020). 'g-C_3N_4/carbon dot-based nanocomposites serve as efficacious photocatalysts for environmental purification and energy generation: A review.' *Journal of Cleaner Production*, *276*, 124319.

Asgar, H. et al. (2020). 'Estimation of electrochemical charge storage capability of ZnO/CuO/reduced graphene oxide nanocomposites.' *International Journal of Energy Research*, *44*(3), 1580–1593.

Aspoukeh, P. K. et al. (2022). 'Synthesis, properties and uses of ZnO nanorods: a mini review.' *International Nano Letters*, *12*(2), 153–168.

Atarod, M. et al. (2016). 'Green synthesis of Pd/RGO/Fe_3O_4 nanocomposite using Withania coagulans leaf extract and its application as magnetically separable and reusable catalyst for the reduction of 4-nitrophenol.' *Journal of Colloid and Interface Science*, *465*, 249–258.

Atarod, M. et al. (2015). 'Green synthesis of a Cu/reduced graphene oxide/Fe_3O_4 nanocomposite using Euphorbia wallichii leaf extract and its application as a recyclable and heterogeneous catalyst for the reduction of 4-nitrophenol and rhodamine B.' *RSC Advances*, *5*(111), 91532–91543.

Avcı, B. et al. (2019). 'Controlling of surface morphology of ZnO nanopowders via precursor material and Al doping.' *Materials Science in Semiconductor Processing*, *99*, 149–158.

Aziz, M. et al. (2014). 'Preparation and characterization of graphene membrane electrode assembly.' *Jurnal Teknologi (Sciences and Engineering)*, *69*(9), 11–14.

Azizi, S. et al. (2016). 'Effect of annealing temperature on antimicrobial and structural properties of bio-synthesized zinc oxide nanoparticles using flower extract of Anchusa italica.'

Journal of Photochemistry and Photobiology B: Biology, *161*, 441–449.

Babitha, N. et al. (2018). 'Enhanced Antibacterial Activity and Photo-Catalytic Properties of ZnO Nanoparticles: Pedalium Murex Plant Extract-Assisted Synthesis.' *Journal of Nanoscience and Nanotechnology*, *19*(5), 2888–2894.

Babu, A. T., & Antony, R. (2019). 'Green synthesis of silver doped nano metal oxides of zinc & copper for antibacterial properties, adsorption, catalytic hydrogenation & photodegradation of aromatics.' *Journal of Environmental Chemical Engineering*, *7*(1), 102840.

Babu, L. K. et al. (2019). 'Synthesis, characterization of nanocrystalline ZnO via two different chemical methods and its antibacterial activity.' *Surfaces and Interfaces*, *16*, 93–100.

Babu, S. G. et al. (2019). 'Synergistic effect of sono-photocatalytic process for the degradation of organic pollutants using CuO-TiO_2/rGO.' *Ultrasonics Sonochemistry*, *50*, 218–223.

Balouiri, M. et al. (2016). 'Methods for in vitro evaluating antimicrobial activity: A review.' *Journal of Pharmaceutical Analysis*, *6*(2), 71–79.

Bano, S. et al. (2020). 'Metal Oxide Nanostructured Materials for Water Treatment: Prospectives and Challenges.' In *Modern Age Waste Water Problems* (pp. 213–231). Springer International Publishing.

Basnet, P. et al. (2018). 'A review on bio-synthesized zinc oxide nanoparticles using plant extracts as reductants and stabilizing agents.' *Journal of Photochemistry and Photobiology B: Biology*, *183*, 201–221.

Bathla, A. et al. (2019). 'Morphology Dependent Photocatalytic Activity of CuO/CuO–TiO_2 Nanocatalyst for Degradation of Methyl Orange Under Sunlight.' *Journal of Nanoscience and Nanotechnology*, *20*(5), 3123–3130.

Bayrami, A. et al. (2019). 'Enriched zinc oxide nanoparticles by Nasturtium officinale leaf extract: Joint ultrasound-microwave-facilitated synthesis, characterization, and implementation for diabetes control and bacterial inhibition.' *Ultrasonics Sonochemistry*,

58(March), 104613.

Bharathi, P. et al. (2019). 'Enhanced charge transfer and separation of hierarchical CuO/ZnO composites: The synergistic effect of photocatalysis for the mineralization of organic pollutant in water.' *Applied Surface Science*, *484*, 884–891.

Bhattacharjee, A., & Ahmaruzzaman, M. (2015). 'Green synthesis of 2D CuO nanoleaves (NLs) and its application for the reduction of p-nitrophenol.' *Materials Letters*, *161*, 79–82.

Bhattacharjee, A., & Ahmaruzzaman, M. (2018). 'Microwave assisted facile and green route for synthesis of CuO nanoleaves and their efficacy as a catalyst for reduction and degradation of hazardous organic compounds.' *Journal of Photochemistry and Photobiology A: Chemistry*, *353*, 215–228.

Bhattacharjee, A. et al. (2020). 'Enzyme-mimetic activity of sugar cane juice stabilized CuO nanospheres and CuO/GO nanocomposite: Green synthesis and applications.' *Colloids and Interface Science Communications*, *35*(January), 100239.

Bordbar, M. et al. (2018). 'Melissa Officinalis L. leaf extract assisted green synthesis of CuO/ZnO nanocomposite for the reduction of 4-nitrophenol and Rhodamine B.' *Separation and Purification Technology*, *191*, 295–300.

Boruah, P. K. et al. (2018). 'Magnetic Metal/Metal Oxide Nanoparticles and Nanocomposite Materials for Water Purification.' In *Nanoscale Materials in Water Purification* (pp. 473–503). Elsevier.

Buazar, F. et al. (2019). 'Biofabrication of highly pure copper oxide nanoparticles using wheat seed extract and their catalytic activity: A mechanistic approach.' *Green Processing and Synthesis*, *8*(1), 691–702.

Cahyana, A. H. et al. (2021). 'Green synthesis of $CuFe_2O_4$ nanoparticles mediated by Morus alba L. leaf extract: Crystal structure, grain morphology, particle size, magnetic and catalytic properties in Mannich reaction.' *Ceramics International*, *47*(15), 21373–21380.

Camargo, P. H. C. et al. (2009). 'Nanocomposites: Synthesis, structure, properties and new

application opportunities.' *Materials Research*, *12*(1), 1–39.

Can, M. (2020). 'Green gold nanoparticles from plant-derived materials: An overview of the reaction synthesis types, conditions, and applications.' *Reviews in Chemical Engineering*, *36*(7), 859–877.

Carmen, Z., & Daniel, S. (2012). 'Textile Organic Dyes – Characteristics, Polluting Effects and Separation/Elimination Procedures from Industrial Effluents–A Critical Overview.' In *Organic Pollutants Ten Years After the Stockholm Convention-Environmental and Analytical Update* (pp. 55–86). InTech.

Chandrasekaran, V. et al. (2018). 'Optical and recyclable photocatalytic properties of silica supported ZnO/Au heterostructures under sun light.' *Journal of Materials Science: Materials in Electronics*, *29*(1), 667–673.

Chávez-Urbiola, I. R. et al. (2019). 'Development and characterization of photodiode n-ZnO/p-Si by Radio Frecuency Sputtering, a sensor with low voltage operation and its response to visible and UV light.' *Thin Solid Films*, *669*, 364–370.

Che, W. et al. (2015). 'Morphology-controllable synthesis of CuO nanostructures and their catalytic activity for the reduction of 4-nitrophenol.' *Journal of Physics and Chemistry of Solids*, *77*, 1–7.

Chemingui, H. et al. (2019). 'Facile green synthesis of zinc oxide nanoparticles (ZnO NPs): antibacterial and photocatalytic activities.' *Materials Research Express*, *6*(10), 1050b4.

Chen, C. et al. (2020). 'Self-assembly synthesis of CuO/ZnO hollow microspheres and their photocatalytic performance under natural sunlight.' *Vacuum*, *174*, 109198.

Chen, W. et al. (2018). 'Two-Dimensional Janus Transition Metal Oxides and Chalcogenides: Multifunctional Properties for Photocatalysts, Electronics, and Energy Conversion.' *ACS Applied Materials and Interfaces*, *10*(41), 35289–35295.

Chng, L. L. et al. (2013). 'Nanostructured catalysts for organic transformations.' *Accounts of Chemical Research*, *46*(8), 1825–1837.

Chowdhury, R. et al. (2020). 'Green synthesis of CuO nanoparticles using: Lantana camara flower extract and their potential catalytic activity towards the aza-Michael reaction.' *RSC Advances*, *10*(24), 14374–14385.

Crini, G., & Lichtfouse, E. (2019). 'Advantages and disadvantages of techniques used for wastewater treatment.' *Environmental Chemistry Letters*, *17*(1), 145–155.

Dadi, D. et al. (2017). 'Environmental and health impacts of effluents from textile industries in Ethiopia: the case of Gelan and Dukem, Oromia Regional State.' *Environmental Monitoring and Assessment*, *189*(1), 11.

Dadi, R. et al. (2019). 'Antibacterial activity of ZnO and CuO nanoparticles against gram positive and gram negative strains.' *Materials Science and Engineering C*, *104*, 109968.

Danish, M. S. S. et al. (2021). 'Photocatalytic applications of metal oxides for sustainable environmental remediation.' *Metals*, *11*(1), 1–25.

Das, S., & Srivastava, V. C. (2018). 'An overview of the synthesis of CuO-ZnO nanocomposite for environmental and other applications.' *Nanotechnology Reviews*, *7*(3), 267–282.

Davar, F. et al. (2015). 'Green synthesis of ZnO nanoparticles and its application in the degradation of some dyes.' *Journal of the American Ceramic Society*, *98*(6), 1739–1746.

De Silva, K. K. et al. (2018). 'Progress of reduction of graphene oxide by ascorbic acid.' *Applied Surface Science*, *447*(March), 338–346.

Deganello, F. (2017). 'Nanomaterials for environmental and energy applications prepared by solution combustion based-methodologies: Role of the fuel.' *Materials Today: Proceedings*, *4*(4), 5507–5516.

Delsouz Khaki, M. R. et al. (2018). 'Evaluating the efficiency of nano-sized Cu doped TiO_2/ZnO photocatalyst under visible light irradiation.' *Journal of Molecular Liquids*, *258*, 354–365.

Devendran, P., & Swaminathan, M. (2019). 'Photo Functional Materials for Environmental Remediation.' In *Photocatalytic Functional Materials for Environmental Remediation* (pp.

267–289).

Ding, M. et al. (2018). 'Fabrication of Hierarchical ZnO@NiO Core–Shell Heterostructures for Improved Photocatalytic Performance.' *Nanoscale Research Letters*, *13*(1), 260.

Djurišić, A. B. et al. (2014). 'Strategies for improving the efficiency of semiconductor metal oxide photocatalysis.' *Materials Horizons*, *1*(4), 400–410.

Długosz, O., & Banach, M. (2020). 'Continuous synthesis of metal and metal oxide nanoparticles in microwave reactor.' *Colloids and Surfaces A: Physicochemical and Engineering Aspects*, *606*(August), 125453.

Dobrucka, R. et al. (2021). 'Anti-Leukemia Activity of Au/CuO/ZnO Nanoparticles Synthesized used Verbena officinalis Extract.' *Journal of Inorganic and Organometallic Polymers and Materials*, *31*(1), 191–202.

Dou, P. et al. (2015). 'One-step microwave-assisted synthesis of Ag/ZnO/graphene nanocomposites with enhanced photocatalytic activity.' *Journal of Photochemistry and Photobiology A: Chemistry*, *302*, 17–22.

Duan, H. et al. (2015). 'Green chemistry for nanoparticle synthesis.' *Chemical Society Reviews*, *44*(16), 5778–5792.

Emiru, T. F., & Ayele, D. W. (2017). 'Controlled synthesis, characterization and reduction of graphene oxide: A convenient method for large scale production.' *Egyptian Journal of Basic and Applied Sciences*, *4*(1), 74–79.

Erythropel, H. C. et al. (2018). 'The Green ChemisTREE: 20 years after taking root with the 12 principles.' *Green Chemistry*, *20*(9), 1929–1961.

Fakhari, S. et al. (2019). 'Green synthesis of zinc oxide nanoparticles: a comparison.' *Green Chemistry Letters and Reviews*, *12*(1), 19–24.

Fan, C. et al. (2020). 'Enhanced H_2S gas sensing properties by the optimization of p-CuO/n-ZnO composite nanofibers.' *Journal of Materials Science*, *55*(18), 7702–7714.

Fang, H. et al. (2018). 'Biomimetic synthesis of urchin-like CuO/ZnO nanocomposites with excellent photocatalytic activity.' *New Journal of Chemistry*, *42*(15), 12779–12786.

Fei, W. et al. (2019). 'Fabrication of visible-light-active ZnO/ZnFe-LDH heterojunction on Ni foam for pollutants removal with enhanced photoelectrocatalytic performance.' *Solar Energy*, *188*(March), 593–602.

Firoozi, S., & Hosseini-Sarvari, M. (2021). 'Visible-Light-Induced C-P-Bond Formation Using Reduced Graphene Oxide Decorated with Copper Oxide/Zinc Oxide (rGO/CuO/ZnO) as Ternary Recyclable Nanophotocatalyst.' *ChemistrySelect*, *6*(8), 1764–1771.

Gadipelly, C., & Mannepalli, L. K. (2019). 'Nano-metal oxides for organic transformations.' *Current Opinion in Green and Sustainable Chemistry*, *15*, 20–26.

Galani, S. M. et al. (2018). 'Development of Easily Separable ZnO-Supported Au Nanocatalyst for the Oxidative Esterification of Alcohols and Reduction of Nitroarenes.' *ChemistrySelect*, *3*(32), 9414–9421.

Galani, S. M., & Panda, A. B. (2019). 'Enhanced Thermocatalytic Activity of Porous Yellow ZnO Nanoflakes: Defect- and Morphology-Induced Perspectives.' *Chemistry - An Asian Journal*, *14*(5), 612–620.

Gebrekidan, A. et al. (2009). 'Environmental impacts of Sheba tannery (Ethiopia) effluents on the surrounding water bodies.' *Bulletin of the Chemical Society of Ethiopia*, *23*(2), 269–274.

Geyid, A. et al. (2005). 'Screening of some medicinal plants of Ethiopia for their anti-microbial properties and chemical profiles.' *Journal of Ethnopharmacology*, *97*(3), 421–427.

Gitet, H. et al. (2013). 'Speciation of chromium in soils near Sheba Leather Industry, Wukro Ethiopia.' *Talanta*, *116*, 626–629.

Gold, K. et al. (2018). 'Antimicrobial Activity of Metal and Metal-Oxide Based Nanoparticles.' *Advanced Therapeutics*, *1*(3), 1700033.

Govindasamy, G. A. et al. (2021). 'Compositions and antimicrobial properties of binary ZnO–CuO nanocomposites encapsulated calcium and carbon from Calotropis gigantea targeted for skin pathogens.' *Scientific Reports*, *11*(1), 99.

Guo, F. et al. (2021). 'Construction of Cu_3P-$ZnSnO_3$-g-C_3N_4 p-n-n heterojunction with multiple built-in electric fields for effectively boosting visible-light photocatalytic degradation of broad-spectrum antibiotics.' *Separation and Purification Technology*, *265*, 118477.

Guo, T. (2015). 'A comprehensive review on synthesis methods for transition-metal oxide nanostructures.' *CrystEngComm*, *17*(19), 3551–3585.

Harish, S. et al. (2017). 'Controlled structural and compositional characteristic of visible light active ZnO/CuO photocatalyst for the degradation of organic pollutant.' *Applied Surface Science*, *418*, 103–112.

Hashimi, A. S. et al. (2020). 'Fast microwave-assisted synthesis of copper nanowires as reusable high-performance transparent conductive electrode.' *Current Applied Physics*, *20*(1), 205–211.

Hayyan, M. et al. (2016). 'Superoxide Ion: Generation and Chemical Implications.' *Chemical Reviews*, *116*(5), 3029–3085.

Herring, N. P. et al. (2012). 'Enhanced photocatalytic activity of ZnO-graphene nanocomposites prepared by microwave synthesis.' *Journal of Nanoparticle Research*, *14*(12), 1277.

Herrmann, J. M. (2010). 'Photocatalysis fundamentals revisited to avoid several misconceptions.' *Applied Catalysis B: Environmental*, *99*(3–4), 461–468.

Hezam, A. et al. (2017). 'Heterogeneous growth mechanism of ZnO nanostructures and the effects of their morphology on optical and photocatalytic properties.' *CrystEngComm*, *19*(24), 3299–3312.

Hoseinpour, V., & Ghaemi, N. (2018). 'Novel ZnO-MnO_2-Cu_2O triple nanocomposite: Facial synthesis, characterization, antibacterial activity and visible light photocatalytic performance for dyes degradation-A comparative study.' *Materials Research Express*, *5*(8),

085012.

Huang, F. et al. (2010). 'Analysis of the degradation mechanism of methylene blue by atmospheric pressure dielectric barrier discharge plasma.' *Chemical Engineering Journal*, *162*(1), 250–256.

Huang, J. et al. (2010). 'Preparation of porous flower-shaped SnO_2 nanostructures and their gas-sensing property.' *Sensors and Actuators, B: Chemical*, *147*(2), 467–474.

Huang, Y. et al. (2019). 'Catalytic ozonation of organic contaminants in petrochemical wastewater with iron-nickel foam as catalyst.' *Separation and Purification Technology*, *211*, 269–278.

Husen, A., & Iqbal, M. (2019). 'Nanomaterials and Plant Potential: An Overview.' In A. *Nanomaterials and Plant Potential* (pp. 3–29). Springer International Publishing.

Hussain, I. et al. (2016). 'Green synthesis of nanoparticles and its potential application.' *Biotechnology Letters*, *38*(4), 545–560.

Ilyas, M. et al. (2019). 'Environmental and health impacts of industrial wastewater effluents in Pakistan: A review.' *Reviews on Environmental Health*, *34*(2), 171–186.

Imangaliyeva, A. N. et al. (2019). 'In situ synthesis and catalytic properties of Cu_2O nanoparticles based on clay materials and polyethylene glycol.' *Journal of Nanoparticle Research*, *21*(5), 97.

Ingle, A. P. et al. (2014). 'Bioactivity, mechanism of action, and cytotoxicity of copper-based nanoparticles: A review.' *Applied Microbiology and Biotechnology*, *98*(3), 1001–1009.

Isık, T. et al. (2019). 'Green Synthesis of Zinc Oxide Nanostructures.' In *Zinc Oxide Based Nano Materials and Devices*. IntechOpen.

Islam, M. T. et al. (2019). 'Sucrose-Mediated Fast Synthesis of Zinc Oxide Nanoparticles for the Photocatalytic Degradation of Organic Pollutants in Water.' *ACS Omega*, *4*(4), 6560–6572.

Jana, A., & Gregory, D. H. (2020). 'Microwave-Assisted Synthesis of ZnO–rGO Core–Shell Nanorod Hybrids with Photo- and Electro-Catalytic Activity.' *Chemistry-A European Journal*, *26*(29), 6703–6714.

Jenny, S. et al. (2014). 'Understanding TiO_2 photocatalysis: mechanisms and materials.' *Chemical Reviews*, *114*(19), 9919–9986.

John, S. et al. (2019). 'High photoelectrochemical activity of CuO nanoflakes grown on Cu foil.' *Electrochimica Acta*, *319*, 390–399.

Johra, F. T. et al. (2014). 'Facile and safe graphene preparation on solution based platform.' *Journal of Industrial and Engineering Chemistry*, *20*(5), 2883–2887.

Joseph, S., & Mathew, B. (2015). 'Microwave assisted facile green synthesis of silver and gold nanocatalysts using the leaf extract of Aerva lanata.' *Spectrochimica Acta - Part A: Molecular and Biomolecular Spectroscopy*, *136*(PC), 1371–1379.

Ju, H. M. et al. (2010). 'X-ray diffraction patterns of thermally-reduced graphenes.' *Journal of the Korean Physical Society*, *57*(61), 1649–1652.

Ju, X. et al. (2020). 'Controllable synthesis of porous CuO-Cu_2O/rGO microspheres composite as high-performance electrode material for supercapacitors.' *Composite Interfaces*, *27*(9), 845–858.

Jyoti et al. (2018). 'Highly selective and efficient room temperature NO_2 gas sensors based on Zn-doped CuO nanostructure-rGO hybrid.' *Journal of Materials Science: Materials in Electronics*, *29*(12), 10640–10655.

Jyoti, & Varma, G. D. (2019). 'Synthesis of CuO-ZnO/rGO ternary composites for superior NO_2 gas sensor at room temperature.' *Materials Research Express*, *6*(3), 035011.

Kajbafvala, A. et al. (2012). 'Effects of morphology on photocatalytic performance of Zinc oxide nanostructures synthesized by rapid microwave irradiation methods.' *Superlattices and Microstructures*, *51*(4), 512–522.

Kalantari Bolaghi, Z. et al. (2019). 'Photocatalytic activity of ZnO/RGO composite synthesized by one-pot solution combustion method.' *Materials Research Bulletin*, *115*(January), 191–195.

Kandula, S., & Jeevanandam, P. (2016). 'Synthesis of Cu2O@Ag Polyhedral Core-Shell Nanoparticles by a Thermal Decomposition Approach for Catalytic Applications.' *European Journal of Inorganic Chemistry*, *2016*(10), 1548–1557.

Kanu et al. (2011). 'Industrial Effluents and their Impact on Water Quality of receiving rivers in Nigeria.' *Journal of Applieal Technology in Environmental Sanitation*, *1*(1), 75–86.

Kar, S. et al. (2018). 'A Comprehensive Review over Green Synthesis of Graphene.' *International Journal of Research and Scientific Innovation*, *V*(Vii), 1–12.

Karthik, K. et al. (2018). 'Multifunctional properties of microwave assisted CdO–NiO–ZnO mixed metal oxide nanocomposite: enhanced photocatalytic and antibacterial activities.' *Journal of Materials Science: Materials in Electronics*, *29*(7), 5459–5471.

Kassem, A. A. et al. (2021). 'Catalytic reduction of 4-nitrophenol using copper terephthalate frameworks and CuO@C composite.' *Journal of Environmental Chemical Engineering*, *9*(1), 104401.

Kato, K. et al. (2019). 'A novel single-mode microwave assisted synthesis of metal oxide as visible-light photocatalyst.' *Materials Letters*, *235*, 125–128.

Khan, M. et al. (2015). 'Green approach for the effective reduction of graphene oxide using Salvadora persica L. root (Miswak) extract.' *Nanoscale Research Letters*, *10*(1), 1–9.

Khan, M. M. et al. (2015). 'Metal oxides as photocatalysts.' *Journal of Saudi Chemical Society*, *19*(5), 462–464.

Khan, M. et al. (2018). 'Plant extracts as green reductants for the synthesis of silver nanoparticles: lessons from chemical synthesis.' *Dalton Transactions*, *47*(35), 11988–12010.

Kirankumar, V. S., & Sumathi, S. (2020). 'A review on photodegradation of organic pollutants using spinel oxide.' *Materials Today Chemistry*, *18*, 100355.

Kumar, A. (2017). 'A Review on the Factors Affecting the Photocatalytic Degradation of Hazardous Materials.' *Material Science & Engineering International Journal*, *1*(3), 1–10.

Kumar, A. et al. (2017). 'A combustion synthesis route for magnetically separable graphene oxide-$CuFe_2O_4$-ZnO nanocomposites with enhanced solar light-mediated photocatalytic activity.' *New Journal of Chemistry*, *41*(19), 10568–10583.

Kumar, B. V. et al. (2011). 'ZnO nanoparticle as catalyst for efficient green one-pot synthesis of coumarins through Knoevenagel condensation.' *Journal of Chemical Sciences*, *123*(5), 615–621.

Kumaresan, N. et al. (2020). 'Visible light driven photocatalytic activity of ZnO/CuO nanocomposites coupled with rGO heterostructures synthesized by solid-state method for RhB dye degradation.' *Arabian Journal of Chemistry*, *13*(2), 3910–3928.

Kumari, V. et al. (2019). 'S-, N- and C-doped ZnO as semiconductor photocatalysts: A review.' *Frontiers of Materials Science*, *13*(1), 1–22.

Kwon, H. J. et al. (2018). 'Large-Scale Synthesis and Medical Applications of Uniform-Sized Metal Oxide Nanoparticles.' *Advanced Materials*, *30*(42), 1704290.

Lavín, A. et al. (2019). 'High proportion ZnO/CuO nanocomposites: Synthesis, structural and optical properties, and their photocatalytic behavior.' *Surfaces and Interfaces*, *17*, 100367.

Lee, W. J. et al. (2019). 'Microwave-irradiated reduced graphene oxide nanosheets for highly reversible and ultrafast sodium storage.' *Journal of Alloys and Compounds*, *778*, 382–390.

Lei, C. et al. (2017). 'Synthesis of hierarchical porous zinc oxide (ZnO) microspheres with highly efficient adsorption of Congo red.' *Journal of Colloid and Interface Science*, *490*, 242–251.

Lei, C. et al. (2017). 'Fabrication of hierarchical porous ZnO-Al_2O_3 microspheres with enhanced

adsorption performance.' *Applied Surface Science*, *426*, 360–368.

Lei, X. et al. (2019). 'ZIF-8 derived hollow CuO/ZnO material for study of enhanced photocatalytic performance.' *Colloids and Surfaces A: Physicochemical and Engineering Aspects*, *568*, 1–10.

Li, J. et al. (2020). 'Formation of dumbbell and sphere-like CuO as high-performance anode materials for lithium ion batteries.' *Materials Letters*, *261*, 127058.

Li, L. et al. (2014). 'Microwave-assisted synthesis of nanocomposite Ag/ZnO-TiO_2 and photocatalytic degradation Rhodamine B with different modes.' *Colloids and Surfaces A: Physicochemical and Engineering Aspects*, *457*(1), 134–141.

Li, X. et al. (2018). 'Graphene-based heterojunction photocatalysts.' *Applied Surface Science*, *430*, 53–107.

Li, X. et al. (2013). 'Green synthesis and photo-catalytic performances for ZnO-reduced graphene oxide nanocomposites.' *Journal of Colloid and Interface Science*, *411*, 69–75.

Liao, R. et al. (2011). 'Polyphenol-reduced graphene oxide: Mechanism and derivatization.' *Journal of Physical Chemistry C*, *115*(42), 20740–20746.

Lin, Y. T. et al. (2014). 'Key operating parameters affecting photocatalytic activity of visible-light-induced C-doped TiO_2 catalyst for ethylene oxidation.' *Chemical Engineering Journal*, *248*, 175–183.

Liu, C. et al. (2019). 'CuO/ZnO heterojunction nanoarrays for enhanced photoelectrochemical water oxidation.' *Applied Surface Science*, *469*, 276–282.

Liu, F. et al. (2019). 'Construction of rGO wrapping Cu_2O/ZnO heterostructure photocatalyst for PNP and PAM degradation.' *Environmental Science and Pollution Research*, *26*(24), 25286–25300.

Liu, H. et al. (2018). 'Incorporation of reduced graphene oxide into faceted flower-like f001g TiO_2 for enhanced photocatalytic activity.' *Royal Society Open Science*, *5*(8), 180613.

Liu, T. J. et al. (2013). 'Morphology-dependent photo-catalysis of bare zinc oxide nanocrystals.' *RSC Advances*, *3*(31), 12662–12670.

Liu, X. et al. (2013). 'Investigation of photocatalytic activities over ZnO-TiO_2-reduced graphene oxide composites synthesized via microwave-assisted reaction.' *Journal of Colloid and Interface Science*, *394*(1), 441–444.

Liu, X. et al. (2011). 'Microwave-assisted synthesis of TiO_2-reduced graphene oxide composites for the photocatalytic reduction of Cr(VI).' *RSC Advances*, *1*(7), 1245–1249.

Liu, X. et al. (2012). 'UV-assisted photocatalytic synthesis of ZnO-reduced graphene oxide composites with enhanced photocatalytic activity in reduction of Cr(VI).' *Chemical Engineering Journal*, *183*, 238–243.

Logaranjan, K. et al. (2016). 'Shape- and Size-Controlled Synthesis of Silver Nanoparticles Using Aloe vera Plant Extract and Their Antimicrobial Activity.' *Nanoscale Research Letters*, *11*(1), 520.

Low, J. et al. (2017). 'Heterojunction Photocatalysts.' *Advanced Materials*, *29*(20), 1601694.

Lozhkomoev, A. S. et al. (2019). 'Synthesis of CuO–ZnO composite nanoparticles by electrical explosion of wires and their antibacterial activities.' *Journal of Materials Science: Materials in Electronics*, *30*(14), 13209–13216.

Luo, D. et al. (2019). 'An improved method to synthesize nanoscale graphene oxide using much less acid.' *Materials Today Physics*, *9*(2019), 100097.

Mageshwari, K. et al. (2015). 'Improved photocatalytic activity of ZnO coupled CuO nanocomposites synthesized by reflux condensation method.' *Journal of Alloys and Compounds*, *625*, 362–370.

Mahendran, G. B. et al. (2020). 'Green preparation of reduced graphene oxide by Bougainvillea glabra flower extract and sensing application.' *Journal of Materials Science: Materials in Electronics*, *31*(17), 14345–14356.

Maity, C. K. et al. (2018). 'Single pot fabrication of N-doped reduced GO (N-rGO) /ZnO-CuO nanocomposite as an efficient electrode material for supercapacitor application.' *Vacuum*, *157*, 145–154.

Majumdar, D. et al. (2017). 'Ultrasound assisted formation of reduced graphene oxide-copper (II) oxide nanocomposite for energy storage applications.' *Colloids and Surfaces A: Physicochemical and Engineering Aspects*, *512*, 158–170.

Malwal, D., & Gopinath, P. (2017). 'Efficient adsorption and antibacterial properties of electrospun CuO-ZnO composite nanofibers for water remediation.' *Journal of Hazardous Materials*, *321*, 611–621.

Man, H. et al. (2020). 'Simultaneous deSOx and deNOx of marine vessels flue gas on ZnO-CuO/rGO: Photocatalytic oxidation kinetics.' *Journal of Industrial and Engineering Chemistry*, *92*, 77–87.

Mandeep et al. (2019). 'Pulp and paper industry–based pollutants, their health hazards and environmental risks.' *Current Opinion in Environmental Science and Health*, *12*, 48–56.

Mandlimath, T. R., & Gopal, B. (2011). 'Catalytic activity of first row transition metal oxides in the conversion of p-nitrophenol to p-aminophenol.' *Journal of Molecular Catalysis A: Chemical*, *350*(1–2), 9–15.

Mao, Y. et al. (2019). 'Solvothermal synthesis and photocatalytic properties of ZnO micro/nanostructures.' *Ceramics International*, *45*(2), 1724–1729.

Mardikar, S. P. et al. (2020). 'Sunlight driven highly efficient degradation of methylene blue by CuO-ZnO nanoflowers.' *Journal of Environmental Chemical Engineering*, *8*(2), 102788.

Marković, D. et al. (2020). 'The influence of coating with aminopropyl triethoxysilane and CuO/Cu_2O nanoparticles on antimicrobial activity of cotton fabrics under dark conditions.' *Journal of Applied Polymer Science*, *137*(40), 1–12.

Marslin, G. et al. (2018). 'Secondary metabolites in the green synthesis of metallic nanoparticles.' *Materials*, *11*(6), 940.

Mathalai Sundaram, C. et al. (2019). 'Studies on the catalytic activity of $CuO/TiO_2/ZnO$ ternary nanocomposites prepared via one step hydrothermal green approach.' *Materials Research Express*, *6*(12), 125043.

Mclaren, A. et al. (2009). 'Shape and size effects of ZnO nanocrystals on photocatalytic activity.' *Journal of the American Chemical Society*, *131*(35), 12540–12541.

Mergia, E. et al. (2016). 'Antitrypanosomal activity of Verbascum sinaiticum Benth. (Scrophulariaceae) against Trypanosoma congolense isolates.' *BMC Complementary and Alternative Medicine*, *16*(1), 362.

Meti, S. et al. (2018). 'Chemical free synthesis of graphene oxide in the preparation of reduced graphene oxide-zinc oxide nanocomposite with improved photocatalytic properties.' *Applied Surface Science*, *451*, 67–75.

Mohammadi-Aloucheh, R. et al. (2018a). 'Green synthesis of ZnO and ZnO/CuO nanocomposites in Mentha longifolia leaf extract: characterization and their application as anti-bacterial agents.' *Journal of Materials Science: Materials in Electronics*, *29*(16), 13596–13605.

Mohammadi-Aloucheh, R. et al. (2018b). 'Enhanced anti-bacterial activities of ZnO nanoparticles and ZnO/CuO nanocomposites synthesized using Vaccinium arctostaphylos L. fruit extract.' *Artificial Cells, Nanomedicine and Biotechnology*, *46*(sup1), 1200–1209.

Momeni, M. M. (2015). 'Fabrication of copper decorated tungsten oxide-titanium oxide nanotubes by photochemical deposition technique and their photocatalytic application under visible light.' *Applied Surface Science*, *357*, 160–166.

Momeni, M. M. et al. (2018). 'Fabrication, characterization and photoelectrochemical properties of cuprous oxide-reduced graphene oxide photocatalysts for hydrogen generation.' *Journal of Materials Science: Materials in Electronics*, *29*(5), 4136–4146.

Mukherji, S. et al. (2019). 'Synthesis and characterization of size- And shape-controlled silver nanoparticles.' *Physical Sciences Reviews*, *4*(1), 1–73.

Nagendra, G. K. et al. (2019). 'Study of structural features and antibacterial property of ZnO/CuO nanocomposites derived from solution combustion synthesis.' *IOP Conference Series: Materials Science and Engineering*, *577*(1).

Nakata, K., & Fujishima, A. (2012). 'TiO_2 photocatalysis: Design and applications.' *Journal of Photochemistry and Photobiology C: Photochemistry Reviews*, *13*(3), 169–189.

Nasrollahzadeh, M. et al. (2019). 'Plant-Mediated Green Synthesis of Nanostructures: Mechanisms, Characterization, and Applications.' In *Interface Science and Technology* (1st ed., Vol. 28, pp. 199–322). Elsevier Ltd.

Nasrollahzadeh, M. et al. (2015). 'Tamarix gallica leaf extract mediated novel route for green synthesis of CuO nanoparticles and their application for N-arylation of nitrogen-containing heterocycles under ligand-free conditions.' *RSC Advances*, *5*(51), 40628–40635.

Nasrollahzadeh, M. et al. (2015). 'Green synthesis of Pd/CuO nanoparticles by Theobroma cacao L. seeds extract and their catalytic performance for the reduction of 4-nitrophenol and phosphine-free Heck coupling reaction under aerobic conditions.' *Journal of Colloid and Interface Science*, *448*, 106–113.

Nasrollahzadeh, M. et al. (2019). 'An Introduction to Nanotechnology.' In *Interface Science and Technology* (1st ed., Vol. 28, pp. 1–27). Elsevier Ltd.

Nasrollahzadeh, M. et al. (2019). 'Green Nanotechnology.' In *Interface Science and Technology* (1st ed., Vol. 28, pp. 145–198). Elsevier Ltd.

Nasrollahzadeh, M. et al. (2020). 'Preparation of Au nanoparticles by Q switched laser ablation and their application in 4-nitrophenol reduction.' *Clean Technologies and Environmental Policy*, *22*(8), 1715–1724.

Nosaka, Y., & Nosaka, A. Y. (2017). 'Generation and Detection of Reactive Oxygen Species in Photocatalysis.' *Chemical Reviews*, *117*(17), 11302–11336.

Nunes, D. et al. (2019). 'Metal oxide nanostructures for sensor applications.' *Semiconductor Science and Technology*, *34*(4), 043001.

Nur, A. et al. (2018). 'Synthesis of ZnO/CuO Composite by The Electrochemical Method in The Acetat Acid Solution.' *EKUILIBRIUM Journal of Chemical Engineering*, *2*(2), 59.

Ogunyemi, S. O. et al. (2019). 'Green synthesis of zinc oxide nanoparticles using different plant extracts and their antibacterial activity against Xanthomonas oryzae pv. oryzae.' *Artificial Cells, Nanomedicine and Biotechnology*, *47*(1), 341–352.

Ojha, D. P. et al. (2017). 'Photo-Fenton degradation of organic pollutants using a zinc oxide decorated iron oxide/reduced graphene oxide nanocomposite.' *Ceramics International*, *43*(1), 1290–1297.

Oliveira, M. C. et al. (2020). 'Connecting theory with experiment to understand the photocatalytic activity of CuO–ZnO heterostructure.' *Ceramics International*, *46*(7), 9446–9454.

Omar, F. S. et al. (2014). 'Microwave synthesis of zinc oxide/reduced graphene oxide hybrid for adsorption-photocatalysis application.' *International Journal of Photoenergy*, *2014*, 1–8.

Ong, C. B. et al. (2018). 'A review of ZnO nanoparticles as solar photocatalysts: Synthesis, mechanisms and applications.' *Renewable and Sustainable Energy Reviews*, *81*, 536–551.

Oruç, Ç., & Altındal, A. (2017). 'Structural and dielectric properties of CuO nanoparticles.' *Ceramics International*, *43*(14), 10708–10714.

Pal, G. et al. (2019). 'Green synthesis of nanoparticles: A greener approach for a cleaner future.' In *Green Synthesis, Characterization and Applications of Nanoparticles* (pp. 1–26). Elsevier.

Pardakhty, A. et al. (2018). 'A Systematic Study of ZnO/CuO Core/Shell Nanostructures Pegylated by Microwave Assistant Reverse Micelles (RM) Method.' *Journal of Cluster Science*, *29*(6), 1061–1068.

Parham, S. et al. (2019). 'A proposed mechanism of action of textile/Al_2O_3–TiO_2 bimetal oxide nanocomposite as an antimicrobial agent.' *Journal of the Textile Institute*, *110*(5), 791–798.

Paristiowati, M. et al. (2019). 'Green Chemistry-Based Experiments As the Implementation of Sustainable Development Values.' *JTK (Jurnal Tadris Kimiya)*, *4*(1), 11–20.

Park, Y. J. et al. (2015). 'Solution-processed multidimensional ZnO/CuO heterojunction as ultraviolet sensing.' *Optical Materials Express*, *5*(8), 1752.

Paydar, S. (2021). 'Developing cuprospinel $CuFe_2O_4$–ZnO semiconductor heterostructure as a proton conducting electrolyte for advanced fuel cells.' *International Journal of Hydrogen Energy*, *46*(15), 9927–9937.

Pirhashemi, M. (2018). 'Review on the criteria anticipated for the fabrication of highly efficient ZnO-based visible-light-driven photocatalysts.' *Journal of Industrial and Engineering Chemistry*, *62*, 1–25.

Podrojková, N. et al. (2021). 'Pyrolysis Degradation of Cellulose over Highly Effective ZnO and ZnO−CuO Nanocatalysts.' *ChemistrySelect*, *6*(17), 4256–4264.

Prabhu, Y. T. et al. (2019). 'The facile hydrothermal synthesis of CuO@ZnO heterojunction nanostructures for enhanced photocatalytic hydrogen evolution.' *New Journal of Chemistry*, *43*(17), 6794–6805.

Prakash, A. et al. (2013). 'Enhanced photocatalytic performance of ZnO-reduced graphene oxide hybrid synthesized via ultrasonic probe-assisted study.' *AIP Conference Proceedings*, *1512*, 312–313.

Prashanth, G. K. et al. (2019). 'Comparison of Antimicrobial, Antioxidant and Anticancer Activities of ZnO Nanoparticles Prepared by Lemon Juice and Citric Acid Fueled Solution Combustion Synthesis.' *BioNanoScience*, *9*(4), 799–812.

Priyadharsan, A. et al. (2018). 'Synthesis and investigation on synergetic effect of rGO-ZnO decorated MoS_2 microflowers with enhanced photocatalytic and antibacterial activity.' *Colloids and Surfaces A: Physicochemical and Engineering Aspects*, *559*, 43–53.

Qi, H. et al. (2019). 'Photodegradation of Methyl Orange Over CdS–TiO_2/L-zeolite Composite Photocatalyst.' *Journal of Inorganic and Organometallic Polymers and Materials*, *29*(2),

564–571.

Qu, Y. et al. (2020). 'Controllable synthesis of ZnO nanoflowers with structure-dependent photocatalytic activity.' *Catalysis Today*, *355*(January), 397–407.

Rabchinskii, M. K. et al. (2018). 'Facile reduction of graphene oxide suspensions and films using glass wafers.' *Scientific Reports*, *8*(1), 14154.

Raghupathi, K. R., et al. (2011). 'Size-dependent bacterial growth inhibition and mechanism of antibacterial activity of zinc oxide nanoparticles.' *Langmuir*, *27*(7), 4020–4028.

Rahman, M. U. et al. (2019). 'Efficient dye-sensitized solar cells composed of nanostructural zno doped with Ti.' *Catalysts*, *9*(3), 273.

Rai, M. K. et al. (2012). 'Silver nanoparticles: The powerful nanoweapon against multidrug-resistant bacteria.' *Journal of Applied Microbiology*, *112*(5), 841–852.

Raizada, P. et al. (2021). 'Surface defect engineering of metal oxides photocatalyst for energy application and water treatment.' *Journal of Materiomics*, *7*(2), 388–418.

Raj Pant, H. et al. (2013). 'A green and facile one-pot synthesis of Ag-ZnO/RGO nanocomposite with effective photocatalytic activity for removal of organic pollutants.' *Ceramics International*, *39*(5), 5083–5091.

Rajeshkumar, S. et al. (2019). 'Recent advances and biomedical applications of zinc oxide nanoparticles.' In *Green Synthesis, Characterization and Applications of Nanoparticles* (pp. 445–457). Elsevier.

Rajeswari, P. et al. (2018). 'Impact of microwave-assisted synthesis on the morphology and rhodamine B oxidation properties of ZnO nanocomposites.' *Applied Nanoscience*, *8*(4), 645–654.

Rajith Kumar, C. R. et al. (2020). 'One-pot green synthesis of ZnO-CuO nanocomposite and their enhanced photocatalytic and antibacterial activity.' *Advances in Natural Sciences: Nanoscience and Nanotechnology*, *11*(1), 015009.

Ramanathan, S. et al. (2019). 'Synthesis of reduced graphene oxide/ZnO nanocomposites using grape fruit extract and Eichhornia crassipes leaf extract and a comparative study of their photocatalytic property in degrading Rhodamine B dye.' *Journal of Environmental Health Science and Engineering*, *17*(1), 195–207.

Ramos, P. G. et al. (2022). 'A review on improving the efficiency of photocatalytic water decontamination using ZnO nanorods.' *Journal of Sol-Gel Science and Technology*, *102*(1), 105–124.

Ramya, E. et al. (2019). 'CuO@SiO_2 Nanoparticles assisted photocatalytic degradation of 4-nitrophenol and their antimicrobial activity studies.' *Environmental Nanotechnology, Monitoring and Management*, *12*(January), 100240.

Ray, C., & Pal, T. (2017). 'Recent advances of metal-metal oxide nanocomposites and their tailored nanostructures in numerous catalytic applications.' *Journal of Materials Chemistry A*, *5*(20), 9465–9487.

Reddy, E. P. et al. (2003). 'TiO_2-loaded zeolites and mesoporous materials in the sonophotocatalytic decomposition of aqueous organic pollutants: The role of the support.' *Applied Catalysis B: Environmental*, *42*(1), 1–11.

Renuka, L. et al. (2017). 'Synthesis of Sunlight Driven ZnO/CuO Nanocomposite: Characterization, Optical, Electrochemical and Photocatalytic Studies.' *Materials Today: Proceedings*, *4*(11), 11782–11790.

Revathi, V., & Karthik, K. (2018). 'Microwave assisted CdO–ZnO–MgO nanocomposite and its photocatalytic and antibacterial studies.' *Journal of Materials Science: Materials in Electronics*, *29*(21), 18519–18530.

Romeiro, F. C. et al. (2017). 'rGO-ZnO nanocomposites for high electrocatalytic effect on water oxidation obtained by microwave-hydrothermal method.' *Applied Surface Science*, *423*, 743–751.

Safaei-Ghomi, J., & Ghasemzadeh, M. A. (2017). 'Zinc oxide nanoparticle promoted highly efficient one pot three-component synthesis of 2,3-disubstituted benzofurans.' *Arabian*

Journal of Chemistry, *10*, S1774–S1780.

Sagadevan, S., & Murugasen, P. (2015). 'Electrical properties of copper oxide nanoparticles.' *Journal of Nano Research*, *30*, 1–8.

Sahooli, M., & Sabbaghi, S. (2013). 'Investigation of thermal properties of CuO nanoparticles on the ethylene glycol-water mixture.' *Materials Letters*, *93*, 254–257.

Sahu, K. et al. (2020). 'Two-dimensional CuO-ZnO nanohybrids with enhanced photocatalytic performance for removal of pollutants.' *Journal of Physics and Chemistry of Solids*, *137*, 109223.

Sahu, K., & Kar, A. K. (2019). 'Morphological, optical, photocatalytic and electrochemical properties of hydrothermally grown ZnO nanoflowers with variation in hydrothermal temperature.' *Materials Science in Semiconductor Processing*, *104*(March), 104648.

Sahu, K. et al. (2020). 'Enhanced catalytic activity of CuO/Cu_2O hybrid nanowires for reduction of 4-nitrophenol in water.' *Journal of Physics and Chemistry of Solids*, *136*(August 2019), 109143.

Sahu, K. et al. (2019). 'Catalytic reduction of 4-nitrophenol and photocatalytic degradation of organic pollutants in water by copper oxide nanosheets.' *Optical Materials*, *93*, 58–69.

Sahu, K. et al. (2020). 'Morphology Controlled CuO Nanostructures for Efficient Catalytic Reduction of 4-Nitrophenol.' *Catalysis Letters*, *150*(2), 471–481.

Salas Orozco, M. F. et al. (2019). 'Molecular mechanisms of bacterial resistance to metal and metal oxide nanoparticles.' *International Journal of Molecular Sciences*, *20*(11), 2808.

Saleh, S. M. (2019). 'ZnO nanospheres based simple hydrothermal route for photocatalytic degradation of azo dye.' *Spectrochimica Acta-Part A: Molecular and Biomolecular Spectroscopy*, *211*, 141–147.

Saleh, T. A. et al. (2017). 'Principles and advantages of microwave- assisted methods for the synthesis of nanomaterials for water purification.' In *Advanced Nanomaterials for Water*

Engineering, Treatment, and Hydraulics (pp. 40–57).

Santhosh, C. et al. (2016). 'Role of nanomaterials in water treatment applications: A review.' *Chemical Engineering Journal*, *306*, 1116–1137.

Saravanakkumar, D. (2018). 'Synthesis and characterization of ZnO-CuO nanocomposites powder by modified perfume spray pyrolysis method and its antimicrobial investigation.' *Journal of Semiconductors*, *39*(3), 033001.

Saravanan, A. et al. (2021). 'Effective water/wastewater treatment methodologies for toxic pollutants removal: Processes and applications towards sustainable development.' *Chemosphere*, *280*, 130595.

Saravanan, R. et al. (2013). 'Enhanced photocatalytic activity of ZnO/CuO nanocomposite for the degradation of textile dye on visible light illumination.' *Materials Science and Engineering C*, *33*(1), 91–98.

Sathishkumar, P. et al. (2011). 'Synthesis of CuO-ZnO nanophotocatalyst for visible light assisted degradation of a textile dye in aqueous solution.' *Chemical Engineering Journal*, *171*(1), 136–140.

Satish Kumar, N. et al. (2019). 'Zinc oxide nanoparticles as efficient catalyst for the synthesis of novel di-spiroindolizidine bisoxindoles in aqueous medium.' *Environmental Chemistry Letters*, *17*(1), 455–464.

Senthil Kumar, P. et al. (2017). 'CuO/ZnO nanorods: An affordable efficient p-n heterojunction and morphology dependent photocatalytic activity against organic contaminants.' *Journal of Alloys and Compounds*, *701*, 562–573.

Shaalan, N. M. et al. (2016). 'CuO nanoparticles synthesized by microwave-assisted method for methane sensing.' *Optical and Quantum Electronics*, *48*(12), 531.

Shaikh, S. et al. (2019). 'Mechanistic insights into the antimicrobial actions of metallic nanoparticles and their implications for multidrug resistance.' *International Journal of Molecular Sciences*, *20*(10), 1–15.

Shaker-Agjekandy, S., & Habibi-Yangjeh, A. (2016). 'Microwave-assisted one-pot method for preparation of ZnO/AgI nanocomposites with highly enhanced photocatalytic activity under visible-light irradiation.' *Desalination and Water Treatment*, *57*(34), 16015–16023.

Shamsuddin, M., & Raja Nordin, N. (2019). 'Biosynthesis of copper(II) oxide nanoparticles using Murayya koeniggi aqueous leaf extract and its catalytic activity in 4-nitrophenol reduction.' *Malaysian Journal of Fundamental and Applied Sciences*, *15*(2), 218–224.

Sharifi, M. et al. (2021). 'Microwave-assisted reduction reactions.' In *Green Sustainable Process for Chemical and Environmental Engineering and Science* (pp. 315–330). Elsevier.

Sharma, A. et al. (2017). 'Cobalt doped CuO nanoparticles as a highly efficient heterogeneous catalyst for reduction of 4-nitrophenol to 4-aminophenol.' *Applied Catalysis A: General*, *543*(March), 257–265.

Sharma, K. et al. (2017). 'Thermodynamic and Kinetic Studies of Methylene Blue Degradation Using Reactive Adsorption and Its Comparison with Adsorption.' *Journal of Chemical & Engineering Data*, *62*(11), 3651–3662.

Sharma, R. K., & Ghose, R. (2014). 'Synthesis of nanocrystalline CuO-ZnO mixed metal oxide powder by a homogeneous precipitation method.' *Ceramics International*, *40*(7 PART B), 10919–10926.

Sherly, E. D. et al. (2015). 'Visible-light-induced photocatalytic performances of ZnO-CuO nanocomposites for degradation of 2,4-dichlorophenol.' *Cuihua Xuebao/Chinese Journal of Catalysis*, *36*(8), 1263–1272.

Sherly, E. D. et al. (2016). 'A comparative study of the effects of CuO, NiO, ZrO2 and CeO_2 coupling on the photocatalytic activity and characteristics of ZnO.' *Korean Journal of Chemical Engineering*, *33*(4), 1431–1440.

Shinde, D. R. et al. (2017). 'Photocatalytic degradation of dyes in water by analytical reagent grades ZnO, TiO_2 and SnO_2: A comparative study.' *Drinking Water Engineering and Science*, *10*(2), 109–117.

Shultz, L. R. et al. (2020). 'A combined mechanochemical and calcination route to mixed cobalt oxides for the selective catalytic reduction of nitrophenols.' *Molecules*, *25*(1), 89.

Siddiqi, K. S. et al. (2018). 'Properties of Zinc Oxide Nanoparticles and Their Activity Against Microbes.' *Nanoscale Research Letters*, *13*(1), 141.

Singer, S. F. (1970). 'Global effects of environmental pollution.' *Eos, Transactions American Geophysical Union*, *51*(5), 476–478.

Singh, D. K. et al. (2013). 'A study of ZnO nanoparticles and ZnO-EG nanofluid.' *Journal of Experimental Nanoscience*, *8*(5), 731–741.

Singh, K. R. et al. (2021). 'Potentialities of bioinspired metal and metal oxide nanoparticles in biomedical sciences.' *RSC Advances*, *11*(40), 24722–24746.

Singh, P. et al. (2016). 'Biological Synthesis of Nanoparticles from Plants and Microorganisms.' *Trends in Biotechnology*, *34*(7), 588–599.

Siripireddy, B., & Mandal, B. K. (2017). 'Facile green synthesis of zinc oxide nanoparticles by Eucalyptus globulus and their photocatalytic and antioxidant activity.' *Advanced Powder Technology*, *28*(3), 785–797.

Sivaram, N. M. et al. (2018). 'Toxic waste from textile industries.' In *Energy from Toxic Organic Waste for Heat and Power Generation* (pp. 43–54). Elsevier.

Slavin, Y. N. et al. (2017). 'Metal nanoparticles: Understanding the mechanisms behind antibacterial activity.' *Journal of Nanobiotechnology*, *15*(1), 65.

Son, D. I. et al. (2009). 'Structural, optical, and electronic properties of colloidal CuO nanoparticles formed by using a colloid-thermal synthesis process.' *Applied Surface Science*, *255*(21), 8794–8797.

Srikanth, B. et al. (2017). 'Recent advancements in supporting materials for immobilised photocatalytic applications in waste water treatment.' *Journal of Environmental Management*, *200*, 60–78.

Stan, M. et al. (2015). 'Enhanced photocatalytic degradation properties of zinc oxide nanoparticles synthesized by using plant extracts.' *Materials Science in Semiconductor Processing*, *39*, 23–29.

Subbiah, D. K. et al. (2018). 'Nanostructured ZnO on cotton fabrics – A novel flexible gas sensor & UV filter.' *Journal of Cleaner Production*, *194*, 372–382.

Sun, H. et al. (2019). 'A noble bimetal oxysulfide Cu:VOS catalyst for highly efficient catalytic reduction of 4-nitrophenol and organic dyes.' *RSC Advances*, *9*(55), 31828–31839.

Sutradhar, P., & Saha, M. (2016). 'Green synthesis of zinc oxide nanoparticles using tomato (Lycopersicon esculentum) extract and its photovoltaic application.' *Journal of Experimental Nanoscience*, *11*(5), 314–327.

Tănase, M. A. et al. (2021). 'Antibacterial and photocatalytic properties of ZnO nanoparticles obtained from chemical versus Saponaria officinalis extract-mediated synthesis.' *Molecules*, *26*(7).

Tantubay, K. et al. (2020). 'Ternary reduced graphene oxide–CuO/ZnO nanocomposite as a recyclable catalyst with enhanced reducing capability.' *Journal of Environmental Chemical Engineering*, *8*(4), 103818.

Taufique, M. F. et al. (2018). 'ZnO–CuO Nanocomposites with Improved Photocatalytic Activity for Environmental and Energy Applications.' *Journal of Electronic Materials*, *47*(11), 6731–6745.

Thakur, S., & Karak, N. (2012). 'Green reduction of graphene oxide by aqueous phytoextracts.' *Carbon*, *50*(14), 5331–5339.

Thakur, S., & Karak, N. (2015). 'Alternative methods and nature-based reagents for the reduction of graphene oxide: A review.' *Carbon*, *94*(June), 224–242.

Thakur, S., & Mandal, S. K. (2020). 'Morphology engineering of ZnO nanorod arrays to hierarchical nanoflowers for enhanced photocatalytic activity and antibacterial action against: Escherichia coli.' *New Journal of Chemistry*, *44*(27), 11796–11807.

Thamima, M., & Karuppuchamy, S. (2015). 'Microwave assisted synthesis of Zinc oxide nanoparticles.' *International Journal of ChemTech Research*, *8*(11), 250–256.

Thatai, S. et al. (2018). 'Water quality standards, its pollution and treatment methods.' In *A New Generation Material Graphene: Applications in Water Technology* (pp. 21–42). Springer International Publishing.

Thatikayala, D., & Min, B. (2021). 'Ginkgo leaves extract-assisted synthesis of ZnO/CuO nanocrystals for efficient UV-induced photodegradation of organic dyes and antibacterial activity.' *Journal of Materials Science: Materials in Electronics*, *32*(13), 17154–17169.

Theophil Anand, G. et al. (2019). 'Microwave assisted green synthesis of CuO nanoparticles for environmental applications.' *Materials Today: Proceedings*, *36*(2019), 427–434.

Thommes, M. et al. (2015). 'Physisorption of gases, with special reference to the evaluation of surface area and pore size distribution (IUPAC Technical Report).' *Pure and Applied Chemistry*, *87*(9–10), 1051–1069.

Ullah, H. et al. (2021). 'Effect of vegetable waste extract on microstructure, morphology, and photocatalytic efficiency of ZnO–CuO nanocomposites.' *Inorganic and Nano-Metal Chemistry*, *51*(7), 963–975.

Vahdat Vasei, H. et al. (2019). 'Mesoporous honeycomb-like ZnO as ultraviolet photocatalyst synthesized via solution combustion method.' *Materials Research Bulletin*, *117*(April), 72–77.

Varier, K. M. et al. (2020). 'Light-Activated Nanoparticles for Antibacterial Studies.' In *Green Methods for Wastewater Treatment* (pp. 185–216).

Veisi, H. et al. (2021). 'Biosynthesis of CuO nanoparticles using aqueous extract of herbal tea (Stachys Lavandulifolia) flowers and evaluation of its catalytic activity.' *Scientific Reports*, *11*(1), 1–13.

Velayi, E., & Norouzbeigi, R. (2019). 'Single-step prepared hybrid ZnO/CuO nanopowders for water repellent and corrosion resistant coatings.' *Ceramics International*, *45*(14), 16864–

16872.

Velempini, T. et al. (2021). 'Recent developments in the use of metal oxides for photocatalytic degradation of pharmaceutical pollutants in water—a review.' *Materials Today Chemistry*, *19*, 100380.

Venu, S. et al. (2019). 'Phytochemical Profile and Therapeutic Properties of Leafy Vegetables.' In *Plant and Human Health, Volume 2* (Vol. 2, pp. 627–660). Springer International Publishing.

Verma, R. K. (2021). 'Eradication of Fatal Textile Industrial Dyes by Wastewater Treatment.' *Biointerface Research in Applied Chemistry*, *12*(1), 567–587.

Vivekanandhan, S. (2019). 'Combustion Process Using Plant-Based Fuels for the Synthesis of Metal- Oxide Nanostructures.' *ChemistrySelect*, *4*(27), 8026–8042.

Vo, N. L. U. et al. (2020). 'Antibacterial shoe insole-coated CuO-ZnO nanocomposite synthesized by the sol-gel technique.' *Journal of Nanomaterials*, *2020*, 1–13.

Wang, C. et al. (2014). 'Reduced graphene oxide decorated with CuO-ZnO hetero-junctions: Towards high selective gas-sensing property to acetone.' *Journal of Materials Chemistry A*, *2*(43), 18635–18643.

Wang, J. et al. (2017). 'Green reduction of graphene oxide using alanine.' *Materials Science and Engineering C*, *72*, 1–6.

Wang, J. et al. (2012). 'Oxygen vacancy induced band-gap narrowing and enhanced visible light photocatalytic activity of ZnO.' *ACS Applied Materials and Interfaces*, *4*(8), 4024–4030.

Wang, S. et al. (2018). 'ZnO hierarchical microsphere for enhanced photocatalytic activity.' *Journal of Alloys and Compounds*, *741*, 622–632.

Wang, Y. et al. (2020). 'In Situ Construction of CNT/CuS Hybrids and Their Application in Photodegradation for Removing Organic Dyes.' *Nanomaterials*, *10*(1), 178.

Wang, Y. et al. (2016). 'A simple hydrothermal synthesis of flower-like ZnO microspheres and

their improved photocatalytic activity.' *Materials Letters*, *180*, 55–58.

Wei, Q. et al. (2018). 'Construction of rGO wrapping octahedral Ag-Cu_2O heterostructure for enhanced visible light photocatalytic activity.' *Applied Catalysis B: Environmental*, *227*(December 2017), 132–144.

Westall, F., & Brack, A. (2018). 'The Importance of Water for Life.' *Space Science Reviews*, *214*(2), 50.

Wick, L. Y., & Chatzinotas, A. (2019). 'Capacity of Ecosystems to Degrade Anthropogenic Chemicals.' In *Atlas of Ecosystem Services* (pp. 179–182). Springer International Publishing.

Widiarti, N. et al. (2017). 'Synthesis CuO-ZnO nanocomposite and its application as an antibacterial agent.' *IOP Conference Series: Materials Science and Engineering*, *172*(1), 012036.

Witoon, T. et al. (2013). 'Chitosan-assisted combustion synthesis of CuO-ZnO nanocomposites: Effect of pH and chitosan concentration.' *Ceramics International*, *39*(3), 3371–3375.

Wong, K.-A. et al. (2019). 'Shape-Controlled Fabrication of ZnO Architectures for Palm Oil Mill Effluent Degradation.' *Journal of Nanoscience and Nanotechnology*, *19*(8), 5271–5278.

Wu, G. et al. (2017). 'Fabrication of Highly Stable Metal Oxide Hollow Nanospheres and Their Catalytic Activity toward 4-Nitrophenol Reduction.' *ACS Applied Materials and Interfaces*, *9*(21), 18207–18214.

Xu, H. et al. (2020). 'Batch Preparation of CuO/ZnO-Loaded Nanofiber Membranes for Photocatalytic Degradation of Organic Dyes.' *Langmuir*, *36*(47), 14189–14202.

Xu, L. et al. (2017). 'Improved photocatalytic activity of nanocrystalline ZnO by coupling with CuO.' *Journal of Physics and Chemistry of Solids*, *106*, 29–36.

Yallappa, S. et al. (2013). 'Microwave assisted rapid synthesis and biological evaluation of

stable copper nanoparticles using T. arjuna bark extract.' *Spectrochimica Acta - Part A: Molecular and Biomolecular Spectroscopy*, *110*, 108–115.

Yan, Y. et al. (2013). 'Microwave-assisted in situ synthesis of reduced graphene oxide-$BiVO_4$ composite photocatalysts and their enhanced photocatalytic performance for the degradation of ciprofloxacin.' *Journal of Hazardous Materials*, *250–251*, 106–114.

Yang, L. et al. (2010). 'High efficient photocatalytic degradation of p-nitrophenol on a unique Cu_2O/TiO_2 p-n heterojunction network catalyst.' *Environmental Science and Technology*, *44*(19), 7641–7646.

Yaqoob, A. A. et al. (2020). 'Advances and challenges in developing efficient graphene oxide-based zno photocatalysts for dye photo-oxidation.' *Nanomaterials*, *10*(5), 932.

Yaqoob, A. A. et al. (2020). 'Role of nanomaterials in the treatment of wastewater: A review.' *Water (Switzerland)*, *12*(2), 495.

Yendrapati Taraka, T. P. et al. (2019). 'Controlled addition of Cu/Zn in hierarchical CuO/ZnO p-n heterojunction photocatalyst for high photoreduction of CO_2 to MeOH.' *Journal of CO_2 Utilization*, *31*, 207–214.

Yin, L. et al. (2019). 'Microwave-assisted preparation of hierarchical CuO@rGO nanostructures and their enhanced low-temperature H_2S-sensing performance.' *Applied Surface Science*, *476*(2018), 107–114.

Younas, F. et al. (2021). 'Current and emerging adsorbent technologies for wastewater treatment: Trends, limitations, and environmental implications.' *Water*, *13*(2), 1–25.

Yu, H. et al. (2019). 'Effect of surfactants on the morphology and photocatocatalytic properties of ZnO nanostructures.' *Optik*, *185*(March), 990–996.

Yu, J. et al. (2015). 'Photogenerated electron reservoir in hetero-p-n CuO-ZnO nanocomposite device for visible-light-driven photocatalytic reduction of aqueous Cr(vi).' *Journal of Materials Chemistry A*, *3*(3), 1199–1207.

Yuan, W. et al. (2014). 'Synthesis, characterization and photocatalytic activity of cubic-likeCuCr$_2$O4 for dye degradation under visible light irradiation.' *Applied Surface Science*, *319*(1), 350–357.

Yulizar, Y. et al. (2018). 'ZnO/CuO nanocomposite prepared in one-pot green synthesis using seed bark extract of Theobroma cacao.' *Nano-Structures and Nano-Objects*, *16*, 300–305.

Yuvakkumar, R. et al. (2014). 'Novel green synthetic strategy to prepare ZnO nanocrystals using rambutan (Nephelium lappaceum L.) peel extract and its antibacterial applications.' *Materials Science and Engineering C*, *41*, 17–27.

Zaaba, N. I. et al. (2017). 'Synthesis of Graphene Oxide using Modified Hummers Method: Solvent Influence.' *Procedia Engineering*, *184*, 469–477.

Zarei, M. et al. (2020). 'Synthesis of star-shaped CuO nanoparticles supported on magnetic functionalized graphene: Catalytic and antibacterial activity.' *Journal of the Chinese Chemical Society*, *67*(11), 1992–2003.

Zelekew, O. A. et al. (2021). 'Water hyacinth plant extract mediated green synthesis of Cr_2O_3/ZnO composite photocatalyst for the degradation of organic dye.' *Heliyon*, *7*(7), e07652.

Zelekew, O. A., & Kuo, D. H. (2017). 'Facile synthesis of SiO_2@Cu_xO@TiO_2 heterostructures for catalytic reductions of 4-nitrophenol and 2-nitroaniline organic pollutants.' *Applied Surface Science*, *393*, 110–118.

Zhang, C. et al. (2019). 'Progress and challenges in photocatalytic disinfection of waterborne Viruses: A review to fill current knowledge gaps.' *Chemical Engineering Journal*, *355*(July 2018), 399–415.

Zhang, G., & Sun, S. (2017). 'Advantages and Challenges of One-Dimensional Nanostructures for Fuel Cell Applications.' In *One-dimensional Nanostructures for PEM Fuel Cell Applications*. Elsevier Ltd.

Zhang, J. et al. (2019). 'Tunable Fabrication of CuO Nanoplates on ZnO Nanorods:

Heterostructure Formation by Photodeposition for Enhanced Photocatalytic Activity.' *European Journal of Inorganic Chemistry*, *2019*(21), 2654–2660.

Zhang, J. et al. (2008). 'Importance of the relationship between surface phases and photocatalytic activity of TiO_2.' *Angewandte Chemie - International Edition*, *47*(9), 1766–1769.

Zhang, K. et al. (2019). 'Recent Advances in the Nanocatalyst-Assisted $NaBH_4$ Reduction of Nitroaromatics in Water.' *ACS Omega*, *4*(1), 483–495.

Zhang, M. et al. (2018). 'Facile synthesis of a ZnO-BiOI p-n nano-heterojunction with excellent visible-light photocatalytic activity.' *Beilstein Journal of Nanotechnology*, *9*(1), 789–800.

Zhang, N., & Chu, D. (2019). 'Fabrication of flower-like hierarchical ZnO nanostructures with enhanced photocatalytic activity.' *Surfaces and Interfaces*, *14*(399), 251–255.

Zhang, X. et al. (2019). 'Waste Eggshell-Derived Dual-Functional CuO/ZnO/Eggshell Nanocomposites: (Photo)catalytic Reduction and Bacterial Inactivation.' *ACS Sustainable Chemistry and Engineering*, *7*(18), 15762–15771.

Zhang, X. et al. (2014). 'Effect of aspect ratio and surface defects on the photocatalytic activity of ZnO nanorods.' *Scientific Reports*, *4*(1), 4596.

Zhang, Y. H. et al. (2018). 'Facile synthesis of core–shell Cu_2O@ ZnO structure with enhanced photocatalytic H_2 production.' *Journal of Physics and Chemistry of Solids*, *116*, 126–130.

Zhang, Z., & Wang, P. (2012). 'Highly stable copper oxide composite as an effective photocathode for water splitting via a facile electrochemical synthesis strategy.' *Journal of Materials Chemistry*, *22*(6), 2456–2464.

Zhao, Y. et al. (2019). 'Mechanistic Study of Catalytic Hydride Reduction of -NO2 to -NH2 Using Isotopic Solvent and Reducer: The Real Hydrogen Source.' *Journal of Physical Chemistry C*, *123*(25), 15582–15588.

Zhen, Z., & Zhu, H. (2017). 'Structure and properties of graphene.' In *Graphene: Fabrication, Characterizations, Properties and Applications* (pp. 1–12). Elsevier.

Zhou, W. Y. et al. (2013). 'ZnO nanorods: Morphology control, optical properties, and nanodevice applications.' *Science China: Physics, Mechanics and Astronomy*, *56*(12), 2243–2265.

Zhu, L. et al. (2018). 'Synthesis of the 0D/3D CuO/ZnO Heterojunction with Enhanced Photocatalytic Activity.' *Journal of Physical Chemistry C, 122*(17), 9531–9539.

Zhu, X. et al. (2017). 'Green synthesis of graphene nanosheets and their in vitro cytotoxicity against human prostate cancer (DU 145) cell lines.' *Nanomaterials and Nanotechnology*, *7*, 184798041770279.

7. PUBLICATIONS FROM THIS WORK

Published articles from this work are:

Bekru, A. G., Zelekew, O. A., Andoshe, D. M., Sabir, F. K., & Eswaramoorthy, R. (2021). Microwave-assisted synthesis of CuO nanoparticles using cordia africana Lam. leaf extract for 4-nitrophenol reduction. *Journal of Nanotechnology*, 2021, 1–12.

Bekru, A. G., Tufa, L. T., Zelekew, O. A., Goddati, M., Lee, J., & Sabir, F. K. (2022). Green Synthesis of a CuO–ZnO Nanocomposite for Efficient Photodegradation of Methylene Blue and Reduction of 4-Nitrophenol. *ACS Omega*, 7(35), 30908–30919.

Bekru, A. G., Tufa, L. T., Zelekew, O. A., Gwak, J., Lee, J., & Sabir, F. K. (2023). Microwave-Assisted Synthesis of rGO-ZnO/CuO Nanocomposites for Photocatalytic Degradation of Organic Pollutants. *Crystals*, 13(1), 133.